

MICROWAVE RESPONSE IN
SUPERCONDUCTING NANOWIRES

BY

ROBERT CHESLEY DINSMORE

B.S., University of Massachusetts-Amherst, 1999
M.S., Northeastern University, 2003

DISSERTATION

Submitted in partial fulfillment of the requirements
for the degree of Doctor of Philosophy in Physics
in the Graduate College of the
University of Illinois at Urbana-Champaign, 2009

Urbana, Illinois

Doctoral Committee:

Professor Dale Van Harlingen, Chair
Associate Professor Alexey Bezryadin, Director of Research
Professor Paul Goldbart
Professor Paul Selvin

MICROWAVE RESPONSE IN SUPERCONDUCTING NANOWIRES

Robert Chesley Dinsmore, Ph.D.
Department of Physics
University of Illinois at Urbana-Champaign, 2009
Alexey Bezryadin, Adviser

We fabricate superconducting wires using molecular templating technique to study their transport properties when exposed to microwave radiation (MW), at cryogenic temperatures. Our wires have a diameter on the order of the zero temperature coherence length, which makes them quasi-one-dimensional at all temperatures below the superconducting critical temperature, T_C . When our wires are exposed to MW of sufficient power we observe the formation of a finite voltage, dynamic superconducting that we do not see without MW. We identify this dynamic superconducting state as a microwave induced phase slip center (PSC) and study its properties in depth in this dissertation. The jump-wise transition, observed at high bias currents, from the superconducting state into the PSC and the transition from the superconducting state to the normal state are both observed to be stochastic in nature. We attribute this switching to the occurrence of a single quantum phase slip (QPS) which in the presence of a high bias current creates enough heat to warm the wire to a temperature above T_C , or, in the presence of MW, triggers the PSC dynamic state. We present a model for the increase of the rate of QPS with the increase in MW power and show that it is consistent with our observations. The AC Josephson effect is observed in the PSC state (but not in the normal state, to which the wire transits at high bias when no MW is applied) and modeled using a multi-valued current phase relationship. With our model we are able to reproduce the observed fractional Shapiro steps.

Acknowledgements

This work would not have been possible without the help and guidance of many knowledgeable and generous people. I am very grateful for the help and tutelage I received from my adviser, Alexey Bezryadin whose vast knowledge of reduced dimension superconductivity and ability to generate ideas was a major asset.

I would like to thank the founding members of the Bezryadin group, Tony Bolinger, Ulas Coskun, David Hopkins and Andrey Rogachev for their help training me in everything from sample fabrication to curve fitting. They helped make the Bezryadin group the close knit, helpful and collaborative environment that it is today. I would like to thank the other past and present group members Thomas Aref, Matthew Brenner, Cesar Chialvo, Bob Colby, Jaseung Ku, and Mitrabahnu Sahu. I am especially appreciative of the help and guidance I received from Myung-Ho Bae, a postdoc in our group.

I received a great deal of help from people outside of my group as well. Professor Russ Giannetta's help with general experimental know-how was invaluable. The staff engineers in the MRL Microfabrication facility, Tony Banks and Kevin Colravy were always around to help with any questions or concerns. The engineers in the Center for Microanalysis of Materials, Vania Petrova, Mike Marshal and Rick Haasch were very helpful with instrumentation training and performing requested analyses.

I would also like to acknowledge all the wonderful people I have met over the years in Urbana. I had a lot of fun doing things I never would have imagined myself doing. And of course I would like to thank Courtney, whose love and support made all the bumps along the way seem painless.

This work was supported by the U.S. Department of Energy under Grant No. DE-FG02-07ER46453. This work was carried out in part in the Frederick Seitz Materials Research Laboratory Central Facilities, University of Illinois, which are partially supported by the U.S. Department of Energy under Grant Nos. DE-FG02-07ER46453 and DE-FG02-07ER46471.

Contents

1	Introduction.....	1
1.1	The Ginzburg-Landau Theory.....	2
1.2	Josephson Junctions.....	5
1.3	Phase Slips in Quasi-One-Dimensional Wires.....	10
1.4	References.....	23
2	Fabrication and Measurement of Nanowire Devices.....	26
2.1	Fabrication of Superconducting Nanowires Devices Using Molecular Templating.....	26
2.2	Cryostats.....	38
2.3	Transport Measurements.....	45
2.4	References.....	47
3	Superconducting and Insulating Wires.....	48
3.1	DC Transport Measurements on MoGe Nanowires.....	48
3.2	The Superconductor - Insulator Transition in Quasi-One-Dimensional Wires.....	58
3.3	Numerical Study of the Resistance vs. Temperature Behavior in One-Dimensional Wires.....	67
3.4	References.....	76
4	Microwave Response.....	78
4.1	Experimental Observations: The Critical Currents	78
4.2	Discussion and Analysis.....	83
4.3	Phase Slips and Switching in Superconducting Nanowires.....	92
4.4	Additional Observations.....	109

4.5	Summary of Microwave Effects.....	113
4.6	References.....	114
5	AC Josephson Response in Superconducting Nanowires.....	115
5.1	Observation of Shapiro Steps in Superconducting Nanowires.....	115
5.2	Modeling Our Results.....	126
5.3	A Brief Discussion of Noise.....	135
5.4	References.....	137
	Author's Biography.....	138

Chapter 1

Introduction

Superconductivity is the phenomenon where a material can carry a current without any loss, i.e., it has zero electrical resistance. This happens due to a pairing of electrons at temperatures below the critical temperature, T_C . In the classic superconductors this pairing is elegantly described by the Bardeen, Cooper and Schrieffer, (BCS) theory [1]. Under the right conditions the interactions between electrons and the lattice ions produce an effective attraction between two electrons causing them to form a bound pair. These Cooper pairs are the building blocks for the macroscopic quantum state of a superconductor. If a material forms a macroscopic number of Cooper pairs and those pairs are phase-coherent then the material is a superconductor. These pairs can be broken by several mechanisms, in addition to heating them above T_C , such as passing a current greater than the critical depairing current, I_C or applying a magnetic field greater than the thermodynamic critical field H_C . The way that these depairing effects change in reduced dimensional systems is very important to understand for their use in advanced technology such as qubits[2], various types of photon detectors [3], current standards [5].

Superconductors show a great deal of promise in applications ranging from power distribution [4] to elements in quantum computers [5,6] and have been the subject of intense research since they were first discovered by Kamerlingh Onnes in 1911. Superconductors also have very interesting behavior when exposed to magnetic fields, high frequency radiation, and arranged in various geometrical configurations. In 1962 it was proposed by Josephson [7] that a supercurrent can flow through a tunnel junction between two superconductors. These so called Josephson junctions show macroscopic quantum behavior [8] and can be used as voltage standards [9] and to measure very small magnetic fields when used in superconducting quantum interference devices (SQUID)

[10]. Another promising geometry for applications is that of a 1-Dimensional, or a quasi 1-D wire and with recent advances in fabrication techniques [11], such wires can be made to have diameters of only a few nanometers.

The main advancement in this dissertation is the study of these superconducting nanowires when exposed to microwave radiation. The behavior of superconducting nanowires resembles that of larger superconducting wires and to Josephson Junctions but it is significantly different from both. I will begin by describing the physics of superconductivity in 1-Dimension and the physics of Josephson junctions that relates to the experiments done on nanowires in this chapter. In the next chapter I will give a detailed description of the experimental setup used. The focus of chapter three will be on general transport characteristics of superconducting nanowires and how superconductivity breaks down in these structures. Chapters 4 and 5 outline the primary achievements made by my research on microwave response in nanowires.

1.1 The Ginzburg-Landau Theory

The BCS theory is a fully microscopic theory of superconductivity and as such it is difficult to apply to systems outside of a few special cases. Fortunately there is an alternative phenomenological theory developed by Ginzburg and Landau (GL) [12]. The GL theory is a macroscopic, phenomenological, mean field theory which provides accurate description of superconductors in the vicinity of their critical temperature. The GL theory was shown to limiting case of the BCS theory by Gor'kov [13] and it is capable of making very accurate predictions for systems with spatially-dependent order parameter. In the strictest sense the GL theory is only applicable at temperatures just below, but not too close to T_C . There are some instances where it can be extended to even lower temperatures.

The success of the GL theory lies in its treatment of superconductivity in terms of the overall free energy of the system. To do this they first used a pseudowavefunction as a complex order parameter, $\psi(\mathbf{r}) = |\psi(\mathbf{r})|e^{i\phi(\mathbf{r})}$. The density of superconducting electrons

(i.e. the superfluid density) is given by $n_s = |\psi|^2$ and the free energy is then expressed as an expansion of the magnitude of order parameter and the magnitude of its gradient. Assuming that the order parameter varies slowly in space they arrive at the following equation for the GL free energy per unit volume:

$$f = f_{n0} + \alpha |\psi|^2 + \frac{\beta}{2} |\psi|^4 + \frac{1}{4m} \left| \left(\frac{\hbar}{i} \nabla - \frac{2e}{c} \mathbf{A} \right) \psi \right|^2 + \frac{h^2}{8\pi} \quad (1.1)$$

Here f_{n0} is the free energy density of the normal state in the absence of any applied magnetic fields, h , is the applied magnetic field per unit volume and since it is included here it is clear that there must be an upper limit on the applied magnetic field strength for which a stable superconducting state can exist. This is because one can make h large enough to cancel any of the negative terms in equation 1.1. The terms m and e are the mass and the charge of the electron respectively, \mathbf{A} is the vector potential, and α and β are expansion parameters which, in general, depend on temperature and can be determined from the following relationships:

$$\alpha(T) = -\frac{2e^2}{mc^2} H_C^2(T) \lambda_{eff}^2(T) \quad (1.2a)$$

$$\beta(T) = -\frac{16\pi e^4}{m^2 c^4} H_C^2(T) \lambda_{eff}^4(T) \quad (1.2b)$$

$$\lambda_{eff}^2 = \frac{mc^2}{4\pi |\psi|^2 e^2} \quad (1.2c)$$

Here $H_C(T)$ is the temperature dependent critical field and λ_{eff} is the effective London penetration depth, both of which can be measured experimentally or computed using the BCS theory[14]. Using the results for the approximate temperature dependence of the critical field and the penetration depth derived from the microscopic theory one can show that $\alpha(T) = \alpha(0)(1 - T/T_C)$ and $\beta(T) \approx const$. The free energy of a superconducting system will be at a minimum under equilibrium conditions. Thus equation 1. 1, when

integrated over all space, must be minimized. Performing a variational minimization procedure on the integrand leads to the GL differential equations:

$$\hbar \nabla \varphi = \frac{m}{e|\psi|^2} \mathbf{J}_s + \frac{2e}{c} \mathbf{A} = 2m\mathbf{v}_s + \frac{2e}{c} \mathbf{A} = \mathbf{p} \quad (1.3a)$$

$$\alpha\psi + \beta|\psi|^2\psi + \frac{1}{4m} \left(\frac{\hbar}{i} \nabla - \frac{2e}{c} \mathbf{A} \right)^2 \psi = 0 \quad (1.3b)$$

Here \mathbf{A} is the vector potential, \mathbf{p} , is the momentum of the condensate, \mathbf{v}_s is the velocity of Cooper pairs and \mathbf{J}_s is the supercurrent density. When these equations are solved, for the boundary conditions of the system being studied, one can then analyze much of the system's behavior. Once the functional form of the order parameter is solved for, it enables one to determine what types of solutions are possible for a superconducting state and how those states respond to thermal fluctuations, something that plays a key role in 1-Dimensional systems.

Before concluding this brief introduction to the GL theory I will discuss the case of a 1-Dimensional system in the absence of any fields. In this case \mathbf{A} is zero and only equation 1.3b need to be considered. Taking the normalized pseudowavefunction, $y = \psi/\psi_\infty$ with $\psi_\infty^2 = -\alpha/\beta > 0$ equation 1.3b reduces to:

$$\xi^2(T) \frac{d^2 y}{dx^2} + y - y^3 = 0 \quad (1.4a)$$

$$\xi(T) = \frac{\hbar^2}{4m|\alpha(T)|} = \xi(0)(1-T/T_C)^{-1/2} \quad (1.4b)$$

With $\xi(T)$ the GL coherence length. This length has the natural interpretation as the characteristic length of variation of the order parameter, $\psi(\mathbf{r})$. Now that I have defined $\xi(T)$, ξ for brevity, I can define the meaning of 1-Dimension. A 1-Dimensional superconductor is defined as one with 2 of its dimensions $\ll \xi$ and one dimension $\gg \xi$. For the wires that I am studying we have 2 dimensions $\sim \xi$ so they are referred to as

quasi 1-Dimensional. In 1-D wires ζ is the minimum length of wire over which the order parameter can be suppressed by thermal fluctuations. This will be discussed in greater detail later in this chapter. The upper limit for quasi 1 dimensional wires are those that have their cross sectional dimensions less than 4.4ζ [15]. A superconductor with at least 2 dimensions larger than 4.4ζ can support a vortex. Or wires are too small to support a vortex so their physics is fundamentally different to the physics of 2 dimensional films or bulk superconductors.

1.2 Josephson Junctions

The simplest version of a Josephson junction consists of two superconducting electrodes that are connected to each other by a tunnel junction, a short ($\sim \xi$) region of normal metal or a reduced dimension region of the same superconductor, i.e. by any short weak link. These configurations show the DC and AC Josephson effects which were predicted by Josephson in 1962 [7] when he analyzed tunneling between two bulk superconductors separated by a tunnel barrier using the formalism of the microscopic theory [13, 16]. The phase evolution equation, known simply as AC Josephson relation, which stems from the fact that the rate of change of the condensate wavefunction phase is proportional to the electrochemical potential [17,18], is:

$$\frac{d\phi}{dt} = \frac{2eV}{h} \quad (1.5)$$

Here ϕ is the phase difference across the weak link and V is the voltage across the same region. This equation is very general. Thus a time varying phase difference must be present if there is a measurable voltage across any region of superconductor. Josephson also found that for a superconductor-insulator-superconductor (SIS) Josephson junction (JJ) the supercurrent across the junction is given by:

$$I_s = I_c \sin \phi \quad (1.6)$$

This equation gives the current-phase relationship, CPR, for a standard JJ. This equation is valid even for a zero voltage state. Taken in combination with equation 1.5 the CPR tells us how the supercurrent oscillates in the presence of a time varying phase, or voltage. For the case of JJ we see that if a voltage were maintained across the junction, the supercurrent would oscillate at a frequency, f , given by $f=2eV/h$.

A simple but quite realistic description of a superconducting device with a weak link comes in the form of the Resistively and Capacitively Shunted Josephson Junction, (RCSJ), developed by McCumber and Stewart [19,20]. The corresponding circuit diagram is shown in Fig 1.1. Using Kirchoff's law and summing the currents through each channel one gets the following equation for the current conservation:

$$I = I_c \sin \phi + V / R + C dV / dt \quad (1.7)$$

Where I_c represents the critical depairing current and R and C are the values for the shunting resistor and capacitor. Using the ac Josephson relation (eq. 1.5) this can be rewritten as a second order differential equation for the phase:

$$\frac{d^2 \phi}{dt^2} + Q^{-1} \frac{d\phi}{dt} + \sin \phi = I / I_c \quad (1.8)$$

with $Q = (2eI_c / \hbar C) RC \equiv \omega_p RC$. Note this model can be generalized to a non standard JJ or even a 1-D wire by including the appropriate CPR in place of the purely sinusoidal one. It is also possible to consider this equation in the limit $C \rightarrow 0$. In this case the model is the Resistively Shunted Josephson junction (RSJ) model and equation 1.7 reduces to a first order differential equation for ϕ .

Equation 1.8 has a mechanical analog that aids in its interpretation. The equation describes a particle of mass $(\hbar/2e)^2 C$ as it moves along the phase axis of the potential.

$$U(\phi) = -E_J \cos \phi - (\hbar I / 2e) \phi \quad (1.9)$$

and subjected to a drag force given by $(h/2e)^2(1/R)$. The drag force is inversely proportional to resistance because the normal current which are responsible for dissipation are given by V/R . The smaller the resistance is, the larger the normal current is and hence the larger the dissipation. The term E_J , known as the Josephson energy, is given by $E_J = \hbar I_C / 2e$ and I is the current through the junction (summed over all channels). Figure 1.1 shows this potential plotted for some nonzero value of the bias current, I . The function is a periodic sinusoidal function with a tilt determined by the current. The phase “particle” gets trapped in a local minimum for low currents. Thermal fluctuations can cause it to oscillate and possibly jump over the barrier. This time - varying phase leads to a time variation of the supercurrent, and thus leads to a change in the normal current, and thus produces a voltage across the junction. Quantum fluctuations can also lead to the phase particle crossing the energy barrier. This process is known as macroscopic quantum tunneling MQT and was first analyzed theoretically by Caldeira and Leggett [21]. Schmidt and others showed that MQT cannot happen for drag forces greater than \hbar/x^2 where x is the distance between maxima. Thus, so-called Schmid transition occurs in JJ at $R = \hbar/4e^2 = 6.5 \text{ k}\Omega$ [22, 23, 24, 25, 26, 27]. When macroscopic tunneling is proliferating, the phase difference of the order parameter across a junction or a nanowire is subject to strong quantum fluctuations and has no definite value, i.e. it is uncertain. This fact is related to Heisenberg uncertainty principle and represents the state in which the charge on the junctions has a low uncertainty while the phase difference has a high uncertainty, since the charge and the phase are conjugate variables. In the case when the charge is well defined (i.e. has a low uncertainty) and it is not zero there is a nonzero voltage and the JJ does not go superconducting. The application of this phenomenon to nanowires will be discussed in Chapter 3.

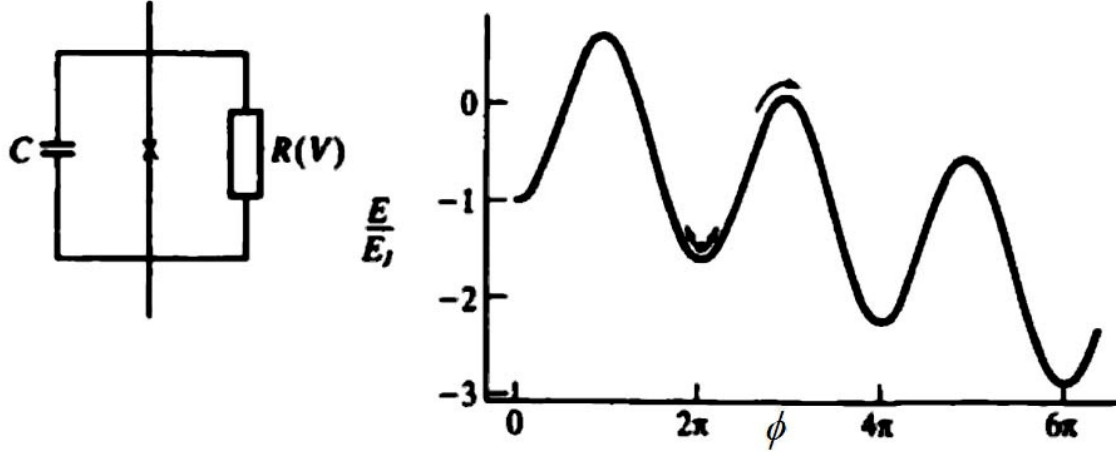


Fig 1.1 Left: Circuit Diagram for the RCSJ Model. Right: The Tilted Washboard potential of the RCSJ Model. This image in its original form is from [14].

When the voltage applied to the JJ has an AC component the AC Josephson effect leads to a lock-in phenomenon leading to the appearance of voltage plateaus in the Voltage-Current, $V(I)$ characteristics, which were first observed by Shapiro in 1963 [9]. These so called Shapiro Steps (SS) are easy to understand in the context of the RCSJ model and a pure voltage bias. The current biased case is not exactly solvable, but the behavior is qualitatively similar [28]. As such I will present a derivation for the appearance of SS in the case of a voltage bias. First let us consider a junction that has a CPR that is a linear combination of sinusoidal terms:

$$I_s = I_c \sum_m c_m \sin(m\phi) \quad (1.10)$$

This current phase relation is a general one and allows for the discussion of fractional SS in terms of higher harmonic terms in the CPR. The bias voltage has an AC and DC component and is given by $V_{bias} = V_{DC} + V_{AC} \sin \omega_1 t$. This voltage must satisfy the ac Josephson relation (eq 1.5) which when integrated gives:

$$\phi = \phi_0 + \omega_{DC} t + \frac{2\pi V_{AC}}{\Phi_0 \omega_1} \sin(\omega_1 t) \quad (1.11)$$

where $\omega_{DC} = 2eV / \hbar$ and $\Phi_0 = h / 2e$ is the magnetic flux quantum. Inserting this relation into equation 1.10 and making use of the following:

$$\sin(a + b \sin x) = \sum_{n=-\infty}^{\infty} (-1)^n J_n(b) \sin(a - nx) \quad (1.12a)$$

$$\text{with } a = \phi_0 + \omega_{DC}t, \quad x = \omega_1 t, \quad \text{and } b = \frac{2\pi V_{AC}}{\Phi_0 \omega_1} \quad (1.12b)$$

One arrives at the following expression for the supercurrent as a function of time:

$$I_s = I_c \sum_m \sum_{n=-\infty}^{\infty} c_m (-1)^n J_n\left(m \frac{2\pi V_{AC}}{\Phi_0 \omega_1}\right) \sin[(m\omega_{DC} - n\omega_1)t - m\phi_0] \quad (1.12)$$

where J_n are Bessel functions. This result gives a nonzero time-averaged supercurrent only if $m\omega_{DC} = n\omega_1$, i.e. for

$$V_{DC} = n / m \cdot hf / 2e \quad (1.13)$$

and for n any non negative integer and m any integer for which $c_m \neq 0$. For a purely sinusoidal (only the $m=1$ term) CPR this reduces to $V_{DC} = nhf / 2e$. This result can be seen as horizontal steps (zero resistance) in the $V(I)$ characteristic of the junction that appear at voltages given by equation 1.13. The widths of these steps are determined by the maximum and minimum values the supercurrent can attain, i.e. by inserting 1.13 into 1.12. The result is as follows:

$$I_s^{m,n} = 2I_c c_m J_n\left(m \frac{2\pi V_{AC}}{\Phi_0 \omega_1}\right) \sin(m\phi_0) \quad (1.14)$$

This reduces to the well known result by putting $m=1$, $c_m=1$ and noting that the maximum value of $\sin(\phi_0)$ is 1.

This concludes my brief discussion of the physics of Josephson Junctions that is necessary in order to understand the physics of 1-Dimensional superconducting systems. My modeling and comparison with experimental results show that the RCSJ model, if amended for the appropriate CPR, provides a good description of the supercurrent oscillations in a superconducting nanowire and allows one to compute its transport properties. We will use this model to gain quantitative understanding of the response of nanowires to the external microwave radiation.

1.3 Phase Slips in Quasi 1-Dimensional Wires

1.3.1 The Free Energy Barrier

The study of one-dimensional superconductivity began in earnest in 1967 with a paper by Little [29]. In this work Little studied the behavior of the GL equation for a one-dimensional wire forming a loop. The case is similar to that of a 1D wire as only the boundary conditions need to be changed. Little showed that fluctuations of both the amplitude and the phase of the superconducting order parameter do not destroy a supercurrent in a one-dimensional wire unless a fluctuation occurs which drives the amplitude of the order parameter to zero in some segment of the wire. Thus Little came to a conclusion that a true phase transition to the superconducting state is only possible if the sample is infinite and three-dimensional.

To understand the concept of a phase slip one needs to analyze the GL equation for the 1D case. In the absence of any external fields equation 1.3a gives the following result for the supercurrent, I_S :

$$I_S = J_S A = \frac{e\hbar}{m} \psi(x)^2 \frac{d}{dx} \phi(x) A \quad (1.15)$$

with A , the cross-sectional area and the order parameter $\psi(x) = \psi_0(x)e^{i\phi(x)}$. Conservation of current requires $|\psi|^2 \frac{d\phi}{dx} = \text{constant}$. Langer and Ambegaokar used this constraint to argue that one could have $\psi \rightarrow 0$ just so long as the phase varied rapidly in space [30]. As the order parameter reaches zero at some point on the 1D wire the phase changes by 2π in a process known as a phase slip. Langer and Ambegaokar analyzed the behavior of a wire for currents below the critical depairing current [30]. This process is shown pictorially in Fig 1.2 below [29]. When plotted in Argand diagram along the x-axis of the wire the order parameter is a tightly wound helical coil where the number of winds represent the total phase difference between its ends in units of 2π . This difference does not have to be an integral multiple of 2π , but the abrupt change in phase, i.e. the phase slip must be either 2π or -2π because the order parameter in the macroscopic leads is defined modulo 2π . The phase slip event happens over a very short time scale $\sim 10^{-12}$ s and produces a voltage spike due to a reduction of the supercurrent. When phase slips occur regularly due to fluctuations they can produce a time average voltage. These phase slips are responsible for the appearance of resistance in a wire below T_C , a topic that is the subject of the next discussion.

In order for a phase slip to occur, the order parameter must be suppressed and be near zero over a region on the order of the GL coherence length, ξ and then return to its equilibrium value. For this to happen the system must cross an energy barrier approximately equal to the condensation energy for a segment of wire with cross section, A , given by $\Delta F \approx H_C^2 / 8\pi A \xi$ with H_C the temperature dependent thermodynamic critical magnetic field.

To find the exact value of the phase slip barrier one needs to know the order parameter “shape” near the phase slip point. In the limit of zero bias current (which is also good for low bias currents) and in the case when the magnetic field is zero the solution for the order parameter corresponding to a phase slip can be written as $y_{\text{PS}} = \tanh[(x - x_0) / \sqrt{2}\xi(T)]$. It is easy to see that this solution satisfies the normalized equation 1.4a, which describes the normalized order parameter $y = \psi / \psi_\infty$. Here x_0 is the position of the phase slip, at which the order parameter goes to zero. The order

parameter increase to its equilibrium value $y_{EQ} = 1$ at a length scale comparable to the coherence length $\xi(T)$. This solution allows one to find the Arrhenius barrier for a phase slip $\Delta F(T)$, which can be computed as a difference between the GL free energy corresponding to the solution $y_{PS}(x)$ and the homogeneous equilibrium solution $y_{EQ} = 1$. Thus one can write $\Delta F(T) = F_{GL}\{y_{PS}(x)\} - F_{GL}\{y_{EQ}\}$, where the F_{GL} is the functional describing the GL free energy [31], given in eq.1.1. Thus, it is possible to find the barrier for a phase slip (and therefore estimate the rate of phase slips) simply by comparing to exact static solutions of the GL equation (one homogeneous and one going to zero at a point), without referring to any equations describing the dynamics of the condensate. The free energy thus computed is:

$$\Delta F = \frac{8\sqrt{2}}{3} \frac{H_c^2}{8\pi} A\xi \quad (1.16)$$

The expression 1.16 is exactly correct only in the limit of zero applied bias current.

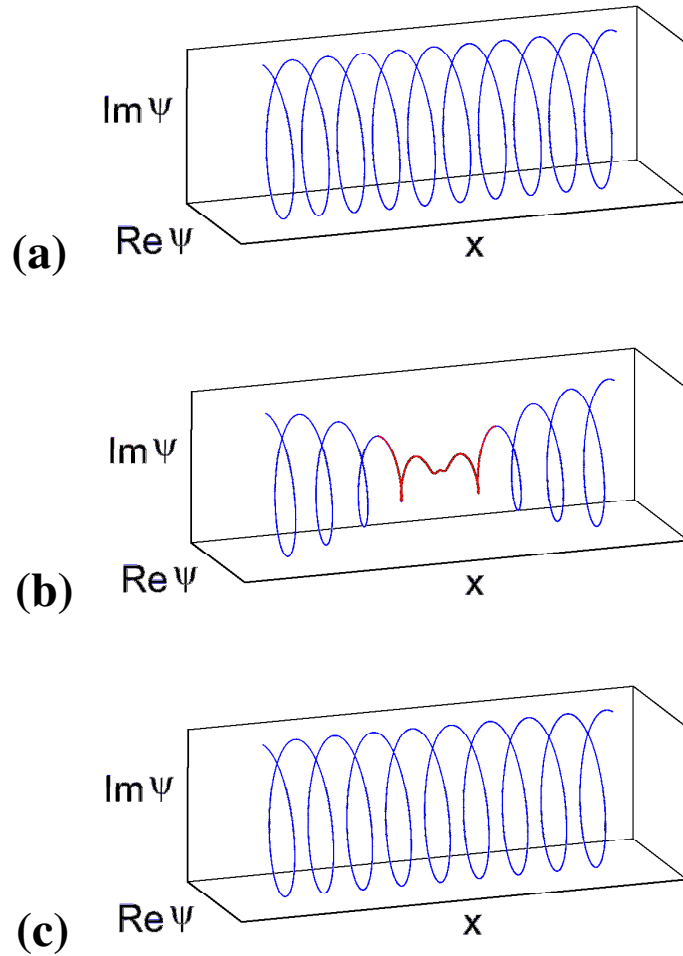


Figure 1.2 Schematic of a phase slip event in a 1-Dimensional superconductor. (a) Before the phase slip there are ten helical turns along the wire. Thus the phase difference between the wire end ends is $10 \times 2\pi$. (b) The order parameter goes to zero at some point along the wire, allowing the phase to slip by -2π . (c) After the phase slip a helical turn has been subtracted (the phase difference becomes of $9 \times 2\pi$). Image created by A. T. Bollinger[32]

Using the temperature dependence of the thermodynamic critical field and of the coherence length this can be rewritten as:

$$\Delta F(T) = \Delta F(0) \left(1 - \frac{T}{T_c}\right)^{3/2}$$

with

$$\Delta F(0) = \frac{8\sqrt{2}}{3} \frac{H_c^2(0)}{8\pi} A \xi(0) \quad (1.17)$$

A more useful form of $\Delta F(0)$ can be derived using the procedure outlined below that makes use of many of the well known results from BCS theory and elementary condensed matter physics. First we note that the zero temperature coherence length is given by:

$$\xi^2(0) = \frac{\hbar^2}{4m|\alpha(0)|} = \frac{\hbar^2 c^2}{8e^2 H_c^2(0) \lambda_{\text{eff}}^2(0)} \quad (1.18)$$

With c , the speed of light in a vacuum and the zero denotes $T=0$, unless stated otherwise. We can now eliminate $H_c(0)$ and write 1.17 b as

$$\Delta F(0) = \frac{\sqrt{2}}{3} \frac{A}{8\pi} \frac{\hbar^2 c^2}{e^2 \xi(0) \lambda_{\text{eff}}^2(0)} \quad (1.19)$$

Here λ_{eff} is the effective London penetration depth, defined below in equation 1.20 in relation to the London penetration depth, λ_L . Next we make use of some relations which are valid in the dirty limit which is certainly the case for the MoGe wires studied in this dissertation [14]

$$\Phi_0 = \left(\frac{2}{3}\right)^{1/2} \pi \xi_0 \lambda_L(0) H_c(0)$$

$$\lambda_{\text{eff}}^2(0) = \lambda_L^2(0) \frac{\xi_0}{\ell} \quad (1.20)$$

Where Φ_0 is the flux quantum ($\Phi_0 = h/2e$), ξ_0 is the Pippard coherence length and ℓ is the electronic mean free path. We can now eliminate the effective penetration depth from 1.29:

$$\Delta F(0) = \frac{\sqrt{2}}{3} \frac{A}{8\pi} \frac{\hbar^2 c^2}{e^2 \xi(0) \lambda_L^2(0)} \frac{\ell}{\xi_0} \quad (1.20)$$

The Pippard coherence length is related to the zero temperature BCS gap, $\Delta(0)$, and the Fermi velocity, v_F by the following relationship:

$$\xi_0 = \frac{\hbar v_F}{\pi \Delta(0)} \quad (1.21)$$

Also the penetration depth is related to the density of superconducting electrons, n_s as follows.

$$\lambda_L^2(0) = \frac{mc^2}{4\pi n_s(0) e^2} = \frac{mc^2}{4\pi n e^2} \quad (1.22)$$

Above I have made use of the fact that at $T=0$ all electrons condense to form pairs and the density of superconducting electrons is equal to the total density of electrons.

Equations 1.21 and 1.22 allow us to eliminate ξ_0 and $\lambda_L(0)$ from eq. 1.20.

$$\Delta F(0) = \frac{\sqrt{2}}{3} \frac{\pi \hbar}{2e^2} \frac{A}{\xi(0)} \frac{ne^2 \ell}{m v_F} \Delta(0) \quad (1.23)$$

From the BCS theory we know that $\Delta(0) = 1.76 k_B T$ and from the Drude model of metals we know that the resistance of a wire can be written as

$$R = \frac{\rho L}{A} = \frac{m v_F}{n e^2 \ell} \frac{L}{A} \quad (1.24)$$

Using these results and noting that $h / (2e)^2 \equiv R_Q$ is the von Klitzing constant for Cooper pairs, we can rewrite 1.23 into a form that is of great use for our experiments [41].

$$\Delta F(0) = \frac{1.76\sqrt{2}}{3} \frac{R_Q}{R_N} \frac{L}{\xi(0)} k_B T_C \quad (1.25)$$

The parameters in this expression are now physical parameters of the wire. With R_N , the normal state resistance of the wire, L , the length of the wire, T_C , the critical temperature of the wire and $\xi(0)$ the zero temperature GL coherence length of the wire. This free energy barrier is analogous to the energy barrier in the tilted washboard potential of the RCSJ model.

1.3.2 The Appearance of Resistance in a 1-Dimensional Superconducting Wire

Now that we have a form for the free energy barrier that must be crossed in order for a phase slip to occur we can discuss one application of it, namely how resistance arises in a wire. The free energy landscape for a wire will look qualitatively similar to the washboard potential except that the phase travels the saddle point of an energy surface and does so only in units of 2π . If there is a bias current applied then the washboard becomes tilted and the barrier for a phase slip is greater in one direction than it is in the other. This energy barrier difference was given by Anderson and Dayem and equals $hI / 2e$ [33]. The rate for a phase slip can be determined by an Arrhenius activation law as follows:

$$\frac{d\phi}{dt} \equiv \Gamma = \Omega \left[\exp\left(\frac{\Delta F - hI/4e}{kT}\right) - \exp\left(\frac{\Delta F + hI/4e}{kT}\right) \right] \quad (1.26)$$

$$V = \frac{\hbar\Omega}{e} e^{-\frac{\Delta F}{kT}} \sinh\left(\frac{hI}{4ekT}\right)$$

Where the bracketed terms account for the phase slip to lower energy state and to the higher energy state and the second equation makes use of the ac Josephson relation. This equation gives the voltage on a wire produced by thermodynamically random phase slip events and is the main result of the theory of thermally activated phase slips (TAPS). The attempt frequency, Ω , is a prefactor that gives how often a phase slip is attempted and will be discussed in more detail shortly. Using Ohms law and the small argument approximation for the *sinh* function we can write down the resistance of a superconducting wire as:

$$R_{LAMH} = R_Q \frac{\hbar\Omega}{k_B T} e^{-\Delta F/k_B T} \quad (1.27)$$

Here the resistance is denoted R_{LAMH} after Langer, Ambegaokar, McCumber and Halperin [30, 34, 35]. The prefactor as originally derived [30] was off by 2 orders of magnitude—a fact that did not have much effect on its prediction of experimental results due to the strong exponential dependence originating from the Arrhenius factor. The value of the prefactor derived by McCumber and Halperin using the time dependent GL theory is

$$\Omega = \frac{L}{\xi} \sqrt{\frac{\Delta F}{k_B T}} \frac{1}{\tau_{GL}} \quad \text{with} \quad \tau_{GL} = \frac{\pi\hbar}{8k_B(T_C - T)} \quad (1.28)$$

Here τ_{GL} is the GL relaxation time. This value of the prefactor improves the LAMH theory agreement with theory, but its use is still controversial. Recently it was argued that the LAMH prefactor is only valid for $T \geq 0.95T_C$ [26]. Because of criticisms such as this we use an alternative approach when fitting data. Now we use the following phenomenological formula for resistance [36].

$$R_{TAPS} = R_N e^{-\Delta F/k_B T} \quad (1.29)$$

This formula still retains the Arrhenius factor; however the attempt frequency depends on the normal resistance of the wire.

The controversy over the prefactor aside, TAPS theory (LAMH or 1.29) produces excellent agreement with experimental data. It was first verified by Lukens, Warburton and Webb in 1970 [37] on Sn whiskers, and later by Newbower, Beasley and Tinkham [44]. Figure 1.3 shows their results along with fits to the LAMH model. Newbower's results were fit better closer to T_C by accounting for the parallel normal channel resistance, using $R(T) = R_{LAMH} R_N / (R_{LAMH} + R_N)$. This model also produced excellent fits for wires studied by members of my group [11, 38, 39].

At very low temperatures the barrier cannot be crossed by thermal fluctuations so in order for a phase slip to occur, it must happen by quantum tunneling. Quantum phase slips (QPS) have been difficult to confirm experimentally. The first claimed experimental observation of QPS was made by Giordano in 1988 when he found long tails in his resistance vs. temperature data [40]. Such tails were later observed by Lau and again attributed to QPS [41]. Unfortunately tails in the R vs. T data can also arise due to inhomogeneities in the wire, as shown by Bollinger in 2004[42]. Thus R vs. T data does not present a very convincing evidence for QPS and as a result we have looked for other signs of QPS. One such sign comes in the behavior of wires subjected to high bias currents. A recently developed model shows that at sufficiently high bias one QPS can cause a wire to go normal because the heat it generates when it dumps the energy, $hI / 2e$, into the wire is enough to cause its temperature to exceed T_C [43]. This model will be discussed in further detail in Chapter 4 where it will be used to explain the suppression of the critical switching current due to the presence of microwave radiation.

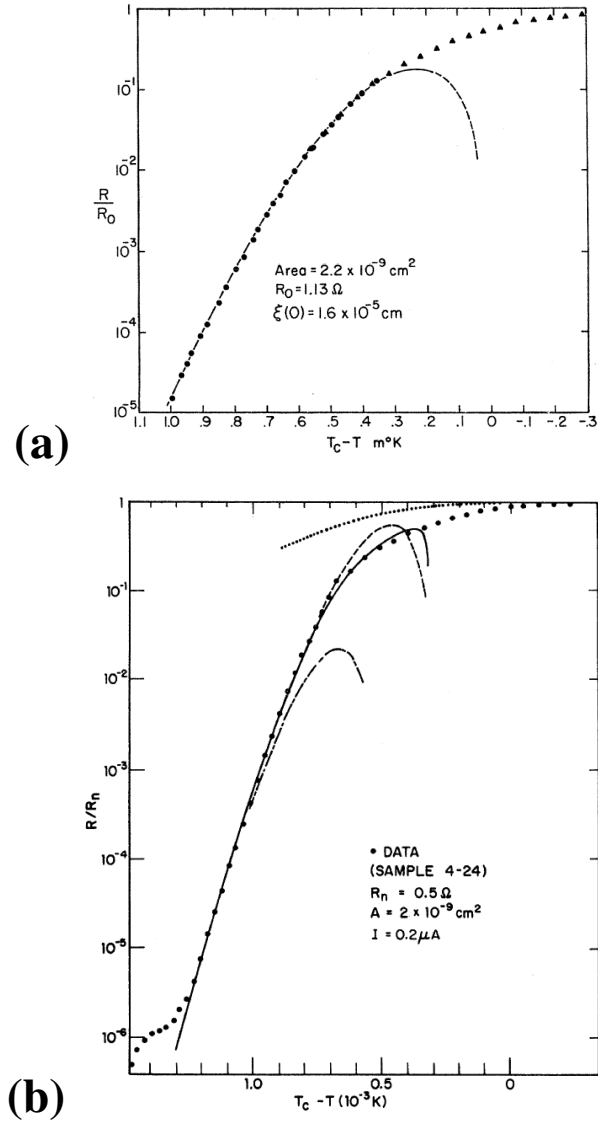


Figure 1.3 Experimental verification of the LAMH Model. (a) Data (symbols) from Lukens Warburton, and Webb [37] and their fit to LAMH theory (dashed line). (b) Data (symbols) from Newbower, Beasley, and Tinkham [44]. The various fits are to LAMH theory (dashed line), LAMH theory with parallel normal channel (solid line), LAMH theory with different attempt frequency (dot-dashed line), and Tucker-Halperin theory (dotted line). The deviation at lowest temperatures is attributed to contact effects.

1.3.3 Skockpol-Beasley-Tinkham model of Phase Slip Centers

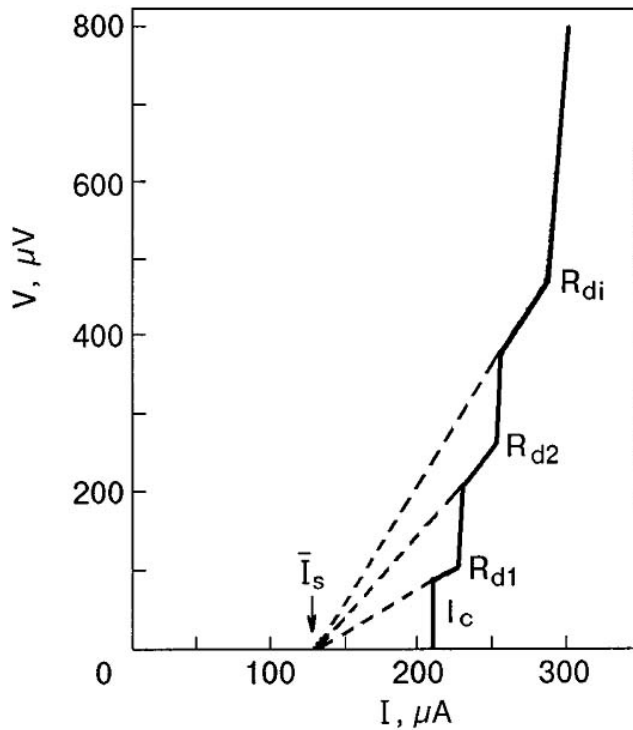


Figure 1.4 Voltage-Current Characteristic for a thin film Sn wire obtained at $T=0.98 T_C$. The critical current, I_c and the offset current \bar{I}_s are indicated. The steps here are indicative of the presence of phase slip centers (PSCs).[46]

When a superconducting wire is subject to a bias current it was found that the voltage increased in regular steps for $I > I_C$ [45]. Figure 1.4 shows this behavior for a thin Sn wire at $T=0.98 T_C$ and can be found in the review article by Dmitriev [46]. The resistive state, i.e. the step region, is clearly not the full normal state of the wire because at higher currents the resistance increases further. These resistive states have also been shown to show Shapiro Steps indicating that they are a dynamic superconducting state [47]. The resistive steps are due to a phenomenon known as a phase slip center (PSC). PSCs are regions of a wire where there are periodic phase slips that give rise to a nonzero time average voltage. Each step in figure 1.4 indicates the addition of a new PSC in the wire.

This phenomenon was first explained by the model of Skockpol, Beasley and Tinkham (SBT) [48] and is summarized schematically in Fig. 1.5 [14]. In this model it is

conceptually easier to view the wire as slightly inhomogeneous. In this case there is a region of the wire with a critical current that is slightly smaller than the critical current for the rest of the wire. Having such a weaker spot is not really necessary because thermal fluctuations can produce a similar effect by suppressing the critical current of one region of the wire more so than the others. As the bias current is increased beyond this minimum critical current there is no longer a stable zero voltage state and the order parameter is suppressed by the phase slip process outlined above. When the order parameter goes to zero during the phase slip the bias current must then be carried as normal current through the PSC region. This is done by Bogoliubov quasiparticles, which then diffuse from the center of the PCS a distance, Λ , which is the quasi-particle diffusion length. The quasiparticle diffusion length is the same as the electric field penetration depth and can be found from the following equation:

$$\Lambda = \sqrt{D\tau_Q} = \left(\frac{1}{3}v_F l\tau_Q\right)^{1/2} \quad (1.30)$$

Here D is the diffusion constant, l , the mean free path and τ_Q is the characteristic time for this process. With all the current being carried by the normal channel, supercurrent is again able to build up in the channel to repeat this cycle. Thus the PSC has a stable AC supercurrent beating at its core as well as an AC normal current. The SBT model predicts that the voltage across the PSC is given by:

$$V = 2\Lambda\rho(I - \beta I_C) / A \quad (1.31)$$

The parameter $\beta \sim 0.5$ gives the time averaged supercurrent in the PSC. This model agreed quite well with experiments and even produced results similar to a more rigorous microscopic theory [46, 49]. An in-depth theoretical review of the PSC properties is given in ref. [50].

It is important to note that previous studies of the PSC phenomenon has been limited to working near T_C . That is because the whiskers employed in the experiments were quite large in diameter and therefore were only quasi-one-dimensional near T_C due

to the fact that ξ diverges at T_C . One of the central topics of this dissertation is the study of such PSCs in wires that remain quasi-one-dimensional down to $T = 0$. Also with this section I have completed my discussion of the relevant historical results and models that I will be making use of in the following chapters.

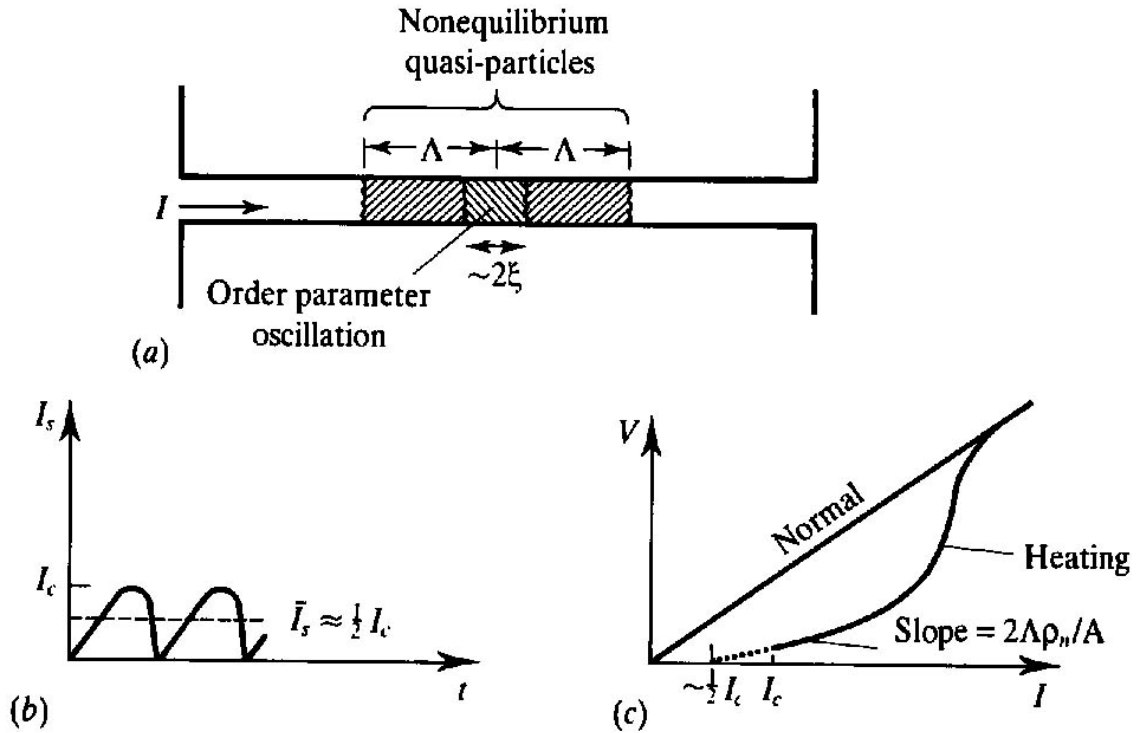


Figure 1.5 Schematic of the SBT model for a Phase Slip Center. (a) Diagram of a current biased wire with a PSC in the middle. The order parameter fluctuates in the central region creating a charge imbalance that extends over the quasi-particle relaxation length Λ . (b) Supercurrent in the PSC core as a function of time with average value $\bar{I}_s \approx \frac{1}{2} I_c$. (c) Schematic $V(I)$ curve for a wire with a single PSC. The PSC sets in at $I = I_c$ with an initial slope given by $R_{PSC} = 2\Lambda\rho_n/A$. For higher currents the wire is eventually heated to a temperature above T_C and is driven normal.[14]

1.4 References

-
- [1] J. Bardeen, L. N. Cooper, and J. R. Schrieffer, *Phys. Rev.* **108**, 1175 (1957)
- [2] M. Grajcar, S. H. W. van der Ploeg, A. Izmalkov, E. Il'ichev, H.-G. Meyer, A. Fedorov, A. Shnirman, Gerd Schön, *Nature Physics* **4**, 612, (2008).
- [3] A. Divochiy, F. Marsili, D. Bitauld, A. Gaggero, R. Leoni, F. Mattioli, A. Korneev, V. Seleznev, N. Kaurova, O. Minaeva, G. Gol'tsman, K. G. Lagoudakis, M. Benkhaoul, F. Lévy and A. Fiore, *Nature Photonics* **2**, 302 (2008).
- [4] U.S. Patent 7038141.
- [5] Mooij, J. E. & Harmans, C. J. P. *New J. Phys.* **7**, 219 (2005); Mooij, J. E. & Nazarov Y. V. *Nature Physics* **2**, 169-172 (2006).
- [6] J. Ku A. Bezryadin, , V. Manucharyan, R. C. Dinsmore III, In preparation
- [7] B. D. Josephson, *Phys. Lett.* **1**, 251 (1962).
- [8] J. M. Martinis, M. H. Devoret, & J. Clarke, 1987 *Phys. Rev. B* **35**, 4682.
- [9] S. Shapiro, *Phys. Rev. Lett.* **11**, 80 - 82 (1963)
- [10] R. Jaklevic, J. Lambe, A. Silver, and J. Mercereau, *Phys. Rev. Lett.* **12**, 159 (1964).
- [11] A. Bezryadin, A.; Lau, C.N.; Tinkham, M. *Nature* **2000**, *404*, 971-974
- [12] V. L. Ginzburg and L. D. Landau, *Zh. Eksperim. i. Teor. Fiz.* **20**, 1064 (1950).
- [13] L. P. Gor'kov, *Zh. Eksperim. i. Teor. Fiz.* **36** 1918 (1959)
- [14] M. Tinkham, *Introduction to Superconductivity*, 2nd ed. (McGraw-Hill, New York, 1996).
- [15] K. K. Likharev, *Rev. Mod. Phys.* **51**, 101-159 (1979)
- [16] N. N. Bogoliubov, *Sov. Phys. JETP*, **7**, 41 (1958).
- [17] S. T. Beliaev, *Sov. Phys. JETP*, **7**, 417-432 (1958).
- [18] L. P. Gor'kov, "Sov. Phys. JETP", **7**, 505-508 (1958).
- [19] W. C. Stewart, *Appl. Phys. Lett.* **12**, 277 (1968).
- [20] D. E. McCumber, *J. Appl. Phys.* **39**, 3113 (1968).
- [21] A. O. Caldeira and A. J. Leggett, *Phys. Rev. Lett.* **46**, 211 (1981)
- [22] A. Schmid, *Phys. Rev. Lett.* **51**, 1506–1509 (1983).

-
- [23] S. A. Bulgadaev, *JETP Lett.* **39**, 315–319 (1984).
- [24] S. Chakravarty, *Phys. Rev. Lett.* **49**, 681–684 (1982).
- [25] J. S. Penttilä, Ü. Parts, P. J. Hakonen, M. A. Paalanen, E. B. Sonin, *Phys. Rev. Lett.* **82**, 1004–1007 (1999).
- [26] D. Meidan, Y. Oreg and G. Refael, *Phys Rev. Lett.* **98**, 187001/1–4 (2007).
- [27] H. P. Büchler, V. B. Geshkenbein, G. Blatter, *Phys. Rev. Lett.* **92**, 067007/1–4 (2004).
- [28] P. Russer, *J. Appl. Phys.* **43**, 2008 (1972)
- [29] W. A. Little, *Phys. Rev.* **156**, 398 (1967).
- [30] S. Langer, and V. Ambegaokar, *Phys. Rev.* **164**, 498. (1967)
- [31] P. G. de Gennes, “*Superconductivity of Metals and Alloys*”, (Westview Press, 1999).
- [32] A. T. Bollinger *Ph.D. Thesis.* UIUC (2005)
- [33] P. W. Anderson and A.H. Dayem, *Phys. Rev. Lett.* **13**, 195 (1964).
- [34] D. E. McCumber, *Phys. Rev.* **172** (1968)
- [35] D. E. McCumber and B. I. Halperin *Phys. Rev.* **B1** 1054 (1970)
- [36] A. Rogachev, T.-C. Wei, D. Pekker, A.T. Bollinger, P. Goldbart, and A. Bezryadin, *Phys. Rev. Lett.* **97**, 137001 (2006).
- [37] J.E. Lukens, R. J. Warburton, and W. Webb, *Phys. Rev. Lett.* **25** 1180 (1970)
- [38] A. Rogachev, A. T. Bollinger, and A. Bezryadin, *Phys. Rev. Lett.* **94**, 017004 (2005)
- [39] A.T. Bollinger, A. Rogachev, A. Bezryadin, *Europhys. Lett.* **76** 3 505-511 (2006)
- [40] N. Giordano, *Phys. Rev. Lett.* **61**, 2137 (1988).
- [41] C. N. Lau, N. Markovic, M. Bockrath, A. Bezryadin, and M. Tinkham, *Phys. Rev. Lett.* **87**, 217003 (2001).
- [42] A. T. Bollinger et. al., *Phys. Rev. B* **69**, 180503(R) (2004).
- [43] N. Shah, D. Pekker, P. M. Goldbart, *Phys. Rev. Lett.* **101**, 207001 (2008)
- [44] R. S. Newbower, M. R. Beasley, and M. Tinkham, *Phys. Rev. B* **5**, 864 (1972).
- [45] J. D. Meyer and G. v. Minnigerode, *Phys. Lett.* **38A** 529 (1972)
- [46] V. M. Dmitriev. *Low. Temp. Phys.* **27** 165 (2001)
- [47] W. Skocpol, M. R. Beasley, M. Tinkham, *J. Appl. Phys.* **45** 4054 (1974)
- [48] W. Skocpol, M. R. Beasley, M. Tinkham, *J. Low. Temp. Phys.* **16** 145 (1974)

[49] V. P. Galako, *Zh.Eksp.Teor.Fiz.* **66**, 379 (1974)

[50] B. I. Ivlev and N. B. Kopnin, *Sov. Phys. Uspekhi*, **27** 206-227 (1984).

Chapter 2

Fabrication and Measurement of Nanowire Devices

2.1 Fabrication of Superconducting Nanowires Devices Using Molecular Templating

We fabricate nanowire devices based on the technique of molecular templating originally developed by Bezryadin et al. [1] and further improved by other group members [2]. With this technique we are able to make superconducting or insulating single nanowire devices as well as single superconducting wire resonators and devices with multiple wires in parallel or two wires in series. The fabrication is achieved by placing a single carbon nanotube over a trench in the substrate and then sputter-coating the nanotube with desired superconducting material. Most of the fabrication was carried out at the Microfabrication Facility and the Center for Microanalysis of Materials, CMM, both part of the Frederick Seitz Materials Research Laboratory (MRL). Figure 2.1 shows the schematics of a single wire device and section 2.1 gives a detailed description of how we fabricate wires.

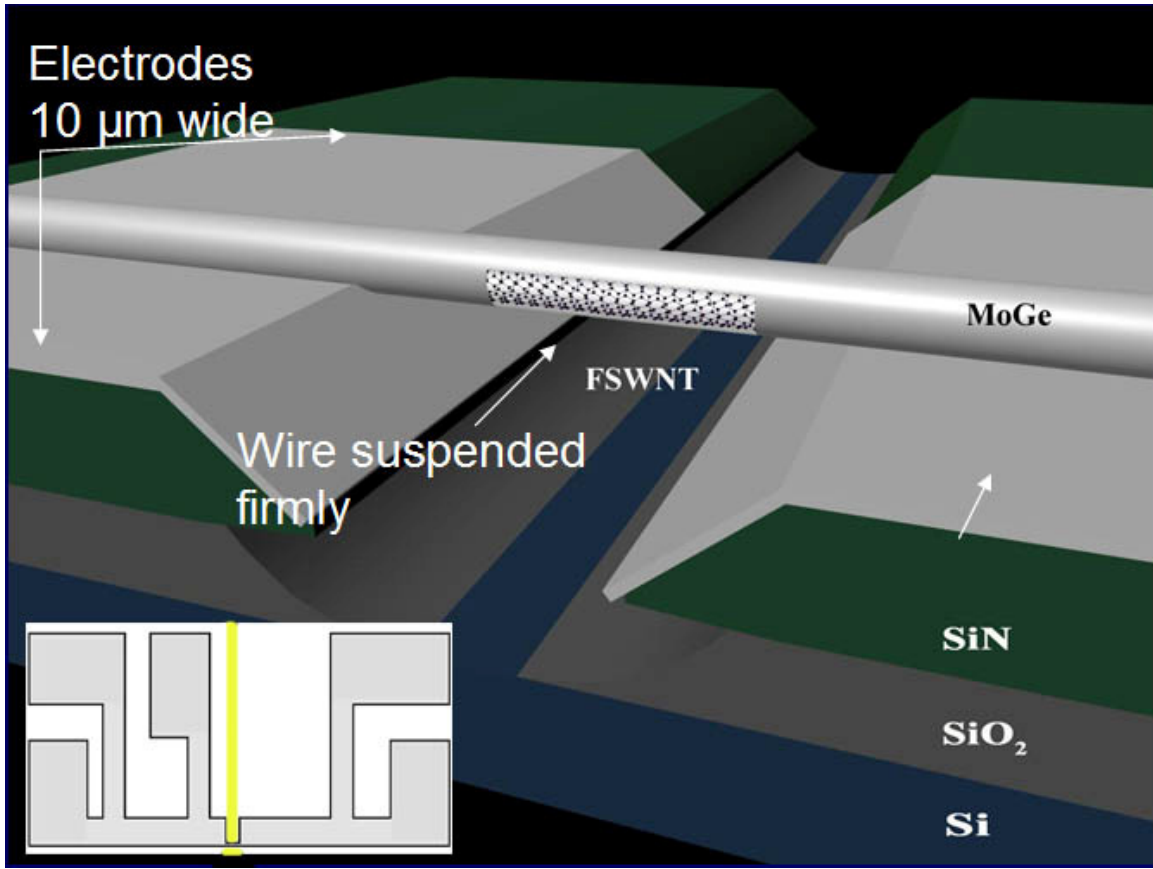


Figure 2.1 Schematic diagram of the central portion typical single nanowire device indicated by the yellow line in the inset. Starting from the base the substrate consists first of a 500 μm Si wafer, then a 500nm layer of SiO_2 and lastly a 60nm layer of SiN . A line ranging from 50nm to 500nm wide is etched into the SiN layer and the SiO_2 is wet etched in HF to create the undercut as shown. Fluorinated single wall carbon nanotubes (FSWNT) are deposited on the substrate and are then sputter coated with a layer of MoGe alloy 5-15nm thick. The wire to be measured is examined and chosen in an SEM and the electrodes are then defined by photolithography by placing the narrow portion of the photomask (see inset) over the wire. Inset: The photomask used for all DC samples. The yellow line indicates the region of the substrate that corresponds to the wire and the trench. This region of the mask comes in 4 sizes, 5 μm , 10 μm , 15 μm , and 20 μm .

2.1.1 Preparation of the Substrate

We start with a purchased 4-inch wafer coated with two layers of SiO_2 and SiN , as is illustrated in Fig.2.1. The wafer itself is 500 μm Si. Some of the wafers are made out of highly doped Si so that it can be used as a gate electrode at low temperatures. The SiO_2

layer consists in fact of two oxide layers, first a 100 nm film of dry SiO₂ and a second layer of 400 nm of wet SiO₂. The top layer is a 60 nm low-stress SiN deposited by low-pressure chemical deposition. These wafers are shipped with a protective layer of PMMA which must be removed by dipping the entire wafer in Acetone and swirling it for 30-45 seconds until it is clean. The wafer is then rinsed in isopropanol and blown dry in Nitrogen. Once cleaned the wafer is then brought to the e-beam writer facility where they will write the pattern for us (Fig. 2.2). The patterns we use were based on a design created by A. T. Bollinger and consists of a repeating pattern of 4.8cm*4.8cm or 6cm*12cm with either a single or double line in the center which will become the trench and integer markers ranging from +119 to -119 adjacent to the trench(es) which serve as aids for optical mask alignment during the photolithography stage of fabrication. In addition to the functional features, each substrate piece is outlined with crosses that are visible to the naked eye. These crosses allow one to easily align the wafer into the dicing saw so it can be cut into individual chips. Once the e-beam writing is complete the wafer is returned to us to be developed and diced up into individual substrates. The e-beam pattern is done in the PMMA layer first and must be projected into SiN using reactive ion etching, (RIE) Fig 2.1. The wafer is first broken into quarters and then a small test piece is broken off to ensure that the RIE procedure works. The etching recipe is to etch the wafer in SF₆ at 20 sccm flow, 60 mT pressure and 75 Watts RF power for 2.5-5 minutes which is designed to etch through the exposed 60nm thin SiN film. The procedure is very sensitive to the recent history of the instrument. This is why we only do ¼ wafer at a time and use a test piece. The test piece is etched in SF₆ for 2.5 minutes and then subjected to our normal substrate cleaning procedure (to follow in the next paragraph) and examined in a scanning electron microscope (SEM) to see the procedure worked. If the marker numbers appear clean and there is a trench for the full length of the test piece then the rest of the ¼ wafer is done for the same length of time. If not, another test piece is broken off and the RIE time is increased and the results are again tested as described above. When the test results are satisfactory the result is a quarter wafer of substrates that are fully patterned but need to be diced into 4.8cm*4.8cm squares for standard samples, or 6cm*12cm for resonator samples. Before this is done the wafer needs to be cleaned and coated with a thin protective layer of photoresist. It is cleaned in acetone, rinsed in isopropanol, dried under nitrogen and a layer of photoresist is spun on it in the

clean-room environment to protect it in the dicing saw. The protective layer of photoresist is necessary as it protects the clean layer of SiN beneath it from all the dust that is created in the dicing saw. If this layer is not present, even if the original PMMA is left instead, the dust sticks to the surface and is so difficult to remove that the resulting substrates are essentially useless. (They can be cleaned, to some extent in the RIE, but the trenches become wider and the time involved to get it right is not worth it). This piece of wafer is then put into the dicing saw, aligned using the large crosses and cut into individual chips. The result of this procedure is a $\frac{1}{4}$ wafer of substrates coated in a very dirty layer of photoresist that can easily be broken into individual substrates.

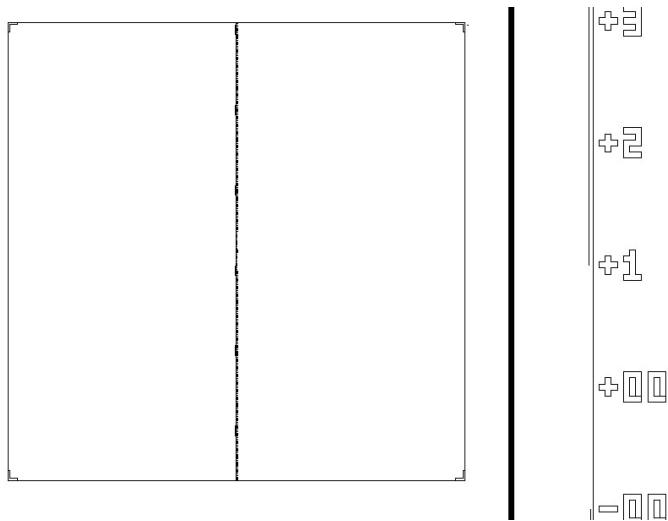


Figure 2.1 *Left: Individual substrate pattern that is 4.8 mm on each side. The central region is the trench line(s) and markers. The dicing markers are visible on the corners. Right: Close up of the trench lines and markers. The alignment markers are separated by 20 μm and are drawn with 1 μm thick lines. This substrate design has two trenches for fabricating devices with wires in series. Single*

wire devices can be made on this substrate, but are usually made on substrates with a single uninterrupted trench. One trench runs the entire length of the chip whereas the second line is a 40 μm long and separated from the first trench. There are 5 different separation distances in this design: 300nm, 500nm, 1 μm , 5 μm and 10 μm . 300nm is the smallest distance between trenches that can be achieved with this design.

The next step in substrate preparation is to clean and etch. This is done in one continuous process in the fume hood. Nine new, clean scintillation vials are placed in the fume hood in a line. From left to right they are filled as follows: 1 Acetone, 2 Acetone, 3 Deionized (DI) H_2O , 4 Nitric Acid, 5 DI H_2O , 6 DI H_2O , 7 Nitric Acid, 8 DI H_2O , 9 Isopropanol. In the middle of the 2 vials of DI H_2O , #5 and #6 we place a small plastic cup and fill it $\frac{1}{2}$ way with 49% HF. The substrates are then cleaned and etched using the following procedure. Using tweezers the first step is to swirl the substrate in vial 1,

acetone to remove the thick layer of photoresist, PR. When the PR is visibly removed the substrate is then placed in vial 2, acetone, polished side (SiN) facing up and put into a sonicating bath for 2 minutes. Next the substrate is rinsed in vial 3, DI H₂O, to remove any acetone and placed polished side up in vial 4, nitric acid, and sonicated for another 2 minutes. The substrate is then rinsed in vial 5, DI H₂O, and then etched in the plastic HF cup for 7-9 seconds swirling gently throughout the exposure. After etching the substrate is doused in vial 6, DI H₂O, swirling for 30 seconds and then put into vial 7, nitric acid, where it is swirled for 1 minute. Finally the substrate is rinsed in vial 8, DI H₂O, and subsequently swirled in vial 9 for 30 seconds as a final rinse. The substrate is then held firmly on a clean pad and blown dry with forced nitrogen gas.

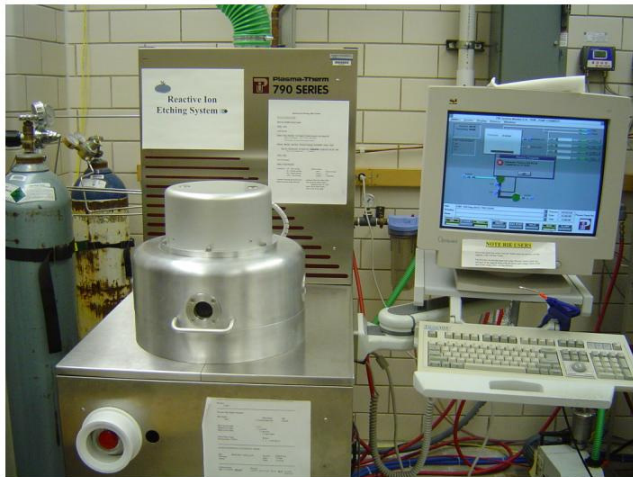


Figure 2.3: The Uniaxis 790 Series Reactive Ion Etching System located in the Materials Research Laboratory's Microfabrication facility.

2.1.2 Deposition of Fluorinated Carbon Nanotubes

Before we can deposit nanotubes we must first get them into solution and make sure that the concentration is optimal for making nanowire devices. The nanotubes that we use are fluorinated single wall carbon nanotubes, FSWNT, obtained from CNI. These tubes come in all lengths from a few 10s of nanometers up to 5 μm and range from 1nm – 10nm in diameter. To make a master solution, one that will subsequently be diluted, we stick a clean capillary tube into the container of fluorinated carbon nanotubes and then tap the black, soot-like powder that sticks to it into a clean scintillation vial. This process may be repeated if desired. When there is enough of the powder in the vial, it is then

filled about $\frac{1}{2}$ of the way full with clean, laboratory grade isopropanol. The resulting mixture is then sonicated for 5 minutes until one obtains a dark murky liquid. The concentration of FSWNTs in this solution is typically too great to be useful in our fabrication process so several dilutions are prepared, typically 1:2, 1:5 and 1:10 and all four are used to make a test batch of samples (using the full fabrication procedure to follow) so that the optimal concentration is achieved. We use trenches that are 50, 100, 200 and 500nm long and it is found that the concentration must be higher the longer the trench because many of the shorter tubes do not fall across the entire trench if it is long. Also higher concentrations are desired for multiwire devices.

Once the desired concentration is achieved that solution can be used to fabricate many samples, but some isopropanol may need to be added due to it evaporating slowly even from a sealed scintillation vial. The tubes are deposited on a clean substrate which is placed in the hood on a clean dust-free paper. The solution needs to be sonicated for approximately 5 minutes in order to evenly disperse the FSWNTs. Once this is done a small glass dropper is used to add two small drops to the clean substrate, taking care to form a rigid droplet on the surface. If the drop wets the chip and slides off, another droplet is added. The droplet is allowed to sit there for 1.5 minutes and then is blown dry with nitrogen, taking care to blow in the direction perpendicular to the trench. It is not clear if blowing parallel to the trench has any effect on the number of tubes that lay across the trench. Once the droplet is blown off the sample is put into a sample holder and is now ready for the sputtering procedure.

2.1.3 Sputter Coating Molybdenum-Germanium Alloys

The sputtering procedure for depositing $\text{Mo}_{26}\text{Ge}_{74}$ was developed by me after the original procedure was not producing superconducting films for the new targets we had purchased. The first procedure is presented here is for the $\text{Mo}_{26}\text{Ge}_{74}$ purchased from SCM[®]. The 4 inch target purchased was 99.99% Molybdenum at 26% and 99.999% Germanium at 74% and indium bonded to a copper backing plate. The target was used exclusively in the MRL Microfabrication facility's AJA ATC 2000 4 gun magnetron

sputtering system which is fitted with a liquid nitrogen filled cold trap to aid in the fabrication of clean superconducting films.

Once the substrates are cleaned and FSWNTs are deposited they are ready to be placed in the sputtering system to be coated with MoGe. Before doing this the sample chuck and the is loaded into the system without the samples attached to it and the target is presputtered for 5-10 minutes. This is done to clean the target of any oxide layer that may have formed since it's last use and to coat all nearby surfaces with MoGe to limit the amount of impurities that can outgas. This is only done once each time the target is first loaded into the system. Once this initial procedure is completed, the chuck is removed and the samples are attached to it using double sided carbon tape which is first touched a few times with a gloved finger to limit the strength of the adhesive. The chuck is then loaded back into the sputtering system and it is left to pump down to $8 * 10^{-8}$ Torr. This pressure is only achievable in this system by providing a steady flow of liquid nitrogen through the cold trap. When the low pressure is reached the samples are ready to be sputter coated. The DC power is set to 350 W, the flow rate of ultra pure Argon is kept at the default 20 sccm, and the pressure of Argon is maintained at 1 mTorr or lower if a steady plasma can be achieved. First the target shutter is opened to ensure that the plasma is going, which is signified by a steady violet glow in the chamber the substrate shutter is then kept opened for the desired amount of time. It was found that for this target at these setting we deposited approximately 3 Angstroms per second. Additionally the T_C of a typical 10nm film was found to be 6 K which makes for a very

The sputtering procedure used for the target we had before this one was similar except that we used 150W power and 4mTorr pressure. This target was ordered to be $Mo_{21}Ge_{79}$, however XPS measurements performed by R. Hatch in the CMM gave a concentration of $Mo_{26}Ge_{74}$ and this is why that concentration was purchased after 2 targets that were both ordered to be $Mo_{21}Ge_{79}$, and verified to be that by XPS, initially failed to produce consistent films. One of these targets was tested again and found to produce good films with the settings used for the newer target. From this we suspect that MoGe films are very susceptible to impurities and need to be sputtered as fast as possible and at the lowest pressure possible to avoid introducing any contaminants. The AJA system places the target 6 inches from the substrate which is far enough to limit the

sputtering rate. If possible it is recommended to use a sputtering system that positions the target as close as possible to the substrate and is maintained at pressures at least 10^{-8} Torr.

2.1.4 Scanning Electron Microscopy and Focused Ion Beam lithography



Figure 2.4 Left: the Hitachi s-4700. Right: The FEI DB235 FIB. Both instruments are part of the MRL's CMM facility.

The samples need to be examined with a scanning electron microscope, SEM, so that they can be selected based on appearance and later isolated with photolithography. The two SEMs we used were a Hitachi S-4700 and the SEM built into the FEI DB235 FIB. Both instruments are capable of obtaining an image with resolution ~ 5 nm but the FIB seems to be more consistent with image quality and stage motion plus it has the added benefit of having an ion beam available to cut away any unwanted wires. Regardless of which instrument is used the procedure is the same. Several samples are attached to the sample holder using carbon tape that is touched first with a gloved finger. The samples are laid out in a manner so that they can all be easily identified and distinguished from one another and then they are loaded into the instrument and the pump down procedure is followed.

Once the samples are ready to be imaged the trench is found first and we begin looking for good wires at least one millimeter in from the edge of the substrate. This avoids getting a wire too close to the edge to be able to keep the entire photolithography

pattern on the substrate which avoids potential leakage for doped substrates. Wires are first chosen based on whether or not they can be isolated with a photomask. Photolithography is done after this step to remove metal coating wires that we do not want to measure so we use the SEM to determine where to place the photomask. We use masks that are 5 μm , 10 μm , 15 μm and 20 μm wide to isolate a given wire. The 5 μm mask is very difficult to work with so we usually use the 10 μm one. This means that a wire must be at least 5 μm away from another wire in both directions in order to ensure that it can be isolated with the mask. In practice the distance must be larger than that and one usually looks for wires that are $\sim 5 \mu\text{m}$ away from one of the markers (see fig 2.4) and have no unwanted wires within 8nm on either side. Choosing wires as such simplifies the mask alignment procedure. For wires that are less than 200nm long we observe bright spots on the ends of the wires for about $\frac{1}{2}$ of the wires on a given sample. We believe that these bright spots are due to there being a second surface below the wire for the imaging electrons to interact with. The presence of a second surface means that the wire is suspended so firmly across the trench that it does not follow the downward slope of the edge of the SiN that results from the RIE process. These wires are favored over wires that do not show these bright spots because it is more likely that they are homogenous and free from any structural defects that might arise if the wire were to follow the contour of the SiN before crossing. There is no conclusive evidence to support this claim, but these spots are not present in longer wires. Wires longer than 200nm seldom show these bright spots and many of these wires show behavior that could be due to the presence of weak links. As with many of the procedures, wires with bright spots show good results, therefore we make sure to make samples with bright spots when possible. Wires are also chosen based on their measured length and width because this, combined with the sputtered film thickness, is a good indicator of their normal resistance. For the wires used to generate the Superconductor – Insulator Transition Phase Diagram this part of the procedure was very important. Once a suitable wire is found we write down the position of the wire and determine how to align the mask for the photolithography procedure. We also take a high resolution image of the wire and then store each sample in its own sample holder and place it in a desiccator where it is kept when not being worked on.

It is important to note that FSWNTs are not as rigid as regular nanotubes. The addition of Fluorine atoms cause the tubes to be insulating because they are bonded to the nanotube through the electrons that, in regular tubes, are the conduction electrons. These electrons also add structural stability to traditional tubes and when they are associated with the fluorine atoms, this stability is reduced causing the tube to be more susceptible to bending. This nonrigidity makes it difficult to make long straight wires if the trench width is much longer than 200nm. A possible fix for this is to use regular CNTs or to make the longer wires thicker by sputtering thicker MoGe layers.

As noted above many times we use the FIB to image wires for the first time. When this is the case it is possible to use the ion beam to remove undesired wires or any remaining SiN bridges (occurs often where e-beam lithography is stiched) from the trench so that it can be isolated with the photomask. To do this one needs to make sure to follow the alignment procedure for the FIB so that the electron beam and ion beam image the same region of the sample. The wire is never to be imaged with the ion beam as that could damage it. The ion beam is tilted 52 degrees from the electron beam so the stage needs to be rotated by that amount whenever it is to be used. The ion beam is set to 10 pA and focused as best as can be achieved on a region of the sample that is of no interest. The wires that are to be cut away are then located with the electron beam and the line tool is used to define the pattern to be cut. The stage is then tilted and the cut is performed with the ion beam.

2.1.5 Photolithography

The last stage in sample fabrication is to isolate the wire(s) to be studied by photolithography. We perform this procedure in the nanofab cleanroom which is part of the MRL's Microfab facility. There are 2 types of positive photoresists that were used in fabricating samples in our group, AZ 5214 and Shipley 1805. The procedures are essentially the same so I will describe the one used for the AZ photoresist and indicate the alternative procedure for Shipley in parentheses where needed.

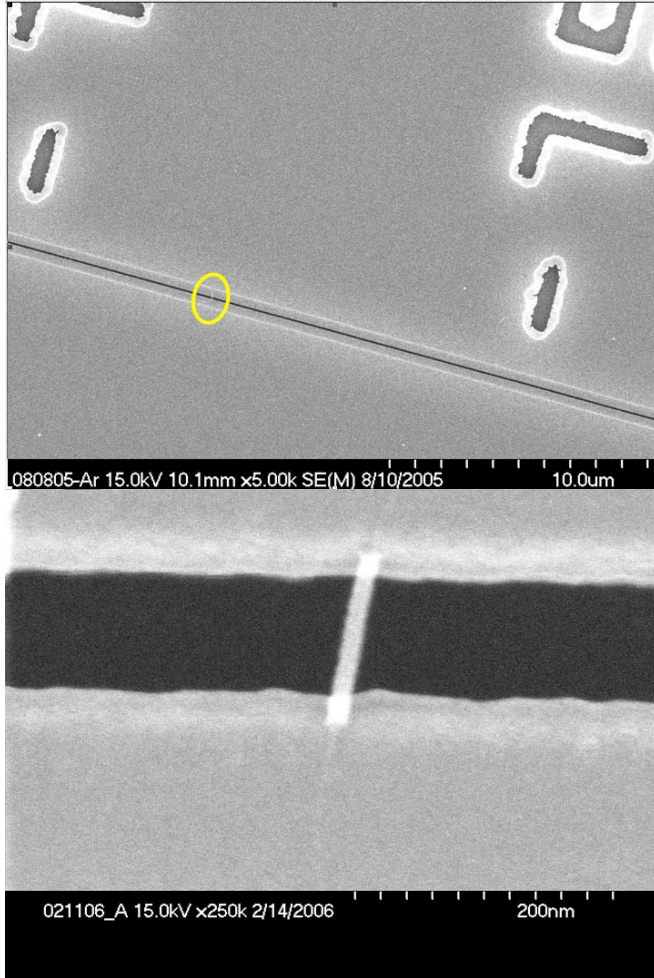


Figure 2.4 SEM images of some samples taken with the Hitachi s-4700. Top: image showing a single nanowire (circled) between two markers. The markers are spaced 20 μm apart and the distance and direction the wire is from the nearest marker is recorded so that the photomask will lie on top of only one wire. Bottom: High resolution image showing a nanowire. The brighter spots near the banks of the trench indicate that the wire is suspended straightly and firmly across the gap.

A hot plate is covered with aluminum foil to ensure an even temperature on its top and set to 110 °C, (120 °C). The samples are carefully placed metal side up on a glass slide and baked on the hot plate for 5 minutes to remove any moisture. We are careful to make sure that we know which sample is which at every stage. After this the slide is moved over to an enclosed blower of Nitrogen where it is allowed to cool for 5 minutes. For samples being patterned with AZ resist the samples are blown with HDMS for 2 minutes to ensure that the resist sticks to the sample. This is not necessary for Shipley. Each sample is then placed on the spinner one at a time and a drop of photoresist is placed on top. The sample is then spun for 25 seconds at 7000 RPM (8000 RPM) to produce a uniform coating of resist. The samples are then placed on a glass slide and baked on the hot plate for 40 seconds at 110 °C (2 min at 120 °C for Shipley).

We use one of 2 Karl Suss MJB3 Mask Aligners to perform the photolithography. They each use a wavelength of 365 nm to expose the resist. The mask used is shown in Fig. 2.1 and consists of a narrow constriction of four sizes—5, 10, 15, and 20 μm that must be aligned across the trench region of the sample. This is done according to the information recorded during the SEM session. Once aligned the resist is exposed for 5.5 seconds (7.5 seconds). After exposure the resist is developed by swirling the sample in a vial of 7:1 mixture of DI water and AZ developer (4: 1 for Shipley) for a few seconds longer than it takes to see the pattern, typically 25 seconds. The sample is immediately removed and rinsed in a stream of DI water. The pattern is then examined to determine if the development is complete. If the edge lines are very straight and there is no stray islands of resist then the job is done, if not the sample is developed for another 5-10 seconds and tested again.

Once the photolithography is done the removal of unwanted metal is done in our lab's fume hood. MoGe is etched in a 3% solution of hydrogen peroxide made from a 9:1 dilution of 30% hydrogen peroxide. The etch rate is faster than 1nm per second so we etch at 1 second per nm sputtered. The sample is etched by swirling it in the diluted hydrogen peroxide solution for the duration required and then immediately rinsing it by swirling it in a scintillation vial of DI water for 30 seconds. At this stage the sample is examined by eye and under a microscope to see if all the metal is removed. If there is any doubt it can be etched for a few seconds more and rinsed and examined again. Samples that are not going to be measured immediately can be put back in their holder and stored in the desiccator. This helps prevent unwanted oxidation. Any sample that is to be measured needs to have the photoresist removed by swirling it in a vial of acetone for 30-45 seconds. The sample is then rinsed in isopropanol and then dried under forced nitrogen. The sample is examined under the microscope one final time to verify that the narrow bridge is continuous across the trench.

2.1.6 Mounting the Sample on a Chip carrier

The cryostats that are used each have a receptacle for a 8-pin chip carrier that we use to mount our samples, though only 6 are wired. We have used several slightly different chip carriers but the mounting procedure is the same for each. The sample

holder is a 14 pin plastic pin carrier that must first be cut roughly in half so there are no more than 8 pins remaining. The holder is then placed in a specially designed sample mounting box. This box grounds all the measurement pins through 100 k Ω resistors to help protect against static discharge across the wire. It is very easy to “burn” a wire with a static discharge so much care is taken to avoid this. In particular, the person mounting the sample needs to be grounded to remove static electricity through an appropriate setup. Thin gold wires (50 μm diameter) are used to attach the sample leads to the pins. These wires are cut to a length of about 1.5 cm and are soldered to the pins. To do this the pins are first tinned with solder and then the heat of the soldering iron is lowered and they are again tinned with indium. We use indium that was previously used as a gasket to seal the cryostat. The resulting alloy melts at a lower temperature than solder does and allows us to solder the thin gold wire without burning it. The wires are held with tweezers and inserted into the pins while they are heated so the alloy melted. When the heat is removed the alloy resolidifies and forms a good electrical contact between the pin and the wire.

After the wires are attached the sample is prepared to be mounted. The sample is placed face up on a clean surface and a grounding bracelet is put on. Indium dots are pressed onto the 4- main leads of the sample using a special tool (the back end of a small drill bit with the drill end covered in electrical tape). A small piece of carbon tape is then put on the flat part of the chip carrier and the sample is attached to it aligned with the leads closest to the pins that are to be used. Next each gold wire is pressed into the indium dot and a second dot is pressed on top ensuring a good electrical contact that is mechanically stable. Once this is completed the sample is ready to be inserted into the slot on the cryostat.

2.2 Cryostats

2.2.2 ^4He Test System

The majority of our measurements were carried out in a Helium-3 cryostat manufactured by Janis, however some were carried out in a test system built by Ulas

Coskun[3]. This system features 6 filtered measurement lines in a 1.25 inch stainless steel tube with a BNC connector box at room temperature. The measurement lines go through pi filters at room temperature and silver paste filters at low temperature to eliminate high frequency noise. They then connect to a 8 pin connector where the sample chip carrier is inserted. The system is also fitted with a heater and a Cernox thermometer. The dipstick can be inserted into the Helium transport dewars which can be pumped on to bring the temperature down below 1.4 K. This system is used primarily for testing samples and for experiments that do not require a magnetic field or 300 mK temperature.

2.2.2 ^3He Cryostat: Cooling

The ^3He cryostat was purchased from Janis Research Company, located in Wilmington, MA. Figure 2.5 is an image from their website showing the base model cryostat that was purchased. Previous members of the group added a custom sample holder and all internal measurement and control electronics. These components of the system will be discussed in detail later, but first I will discuss how the system cools our sample. The system uses the evaporation of Helium-3 isotope to cool our samples down to ~ 280 mK. The cryostat is inserted into a ^4He which is also fitted with a magnet capable of producing 9T fields, also to be discussed in detail below.

The system is cooled by condensing the ^3He into liquid and using its evaporation to cool the vessel thermally connected to the copper block that houses the sample receptacle. To do this we first need to insert the cryostat into a bath of liquid ^4He and there are 2 procedures for doing this depending on whether or not there is Helium in the dewar. In both cases the sample is loaded into the cryostat in the desired configuration, the faraday cage is put into place (see below) and the system is vacuum sealed. There are 2 vacuum cans and they are both designed to be sealed with an indium gasket. Unless the system was being worked on recently, the upper vacuum can will be sealed and only the 2 in diameter bottom can will need to be sealed with an indium gasket. The gasket is made each time by inserting indium wire in the groove designed for this purpose. Once the system is sealed it is pumped on down to 10^{-5} Torr to remove any moisture or air that could freeze up and cause unwanted thermal linkage or damage the electronics at low temperature. A small amount of gaseous ^4He is then added to the cryostat to provide

thermal linkage between the outer vacuum can and the inner portion of the cryostat. This allows the entire system to reach 4K quickly and is evacuated once that occurs.

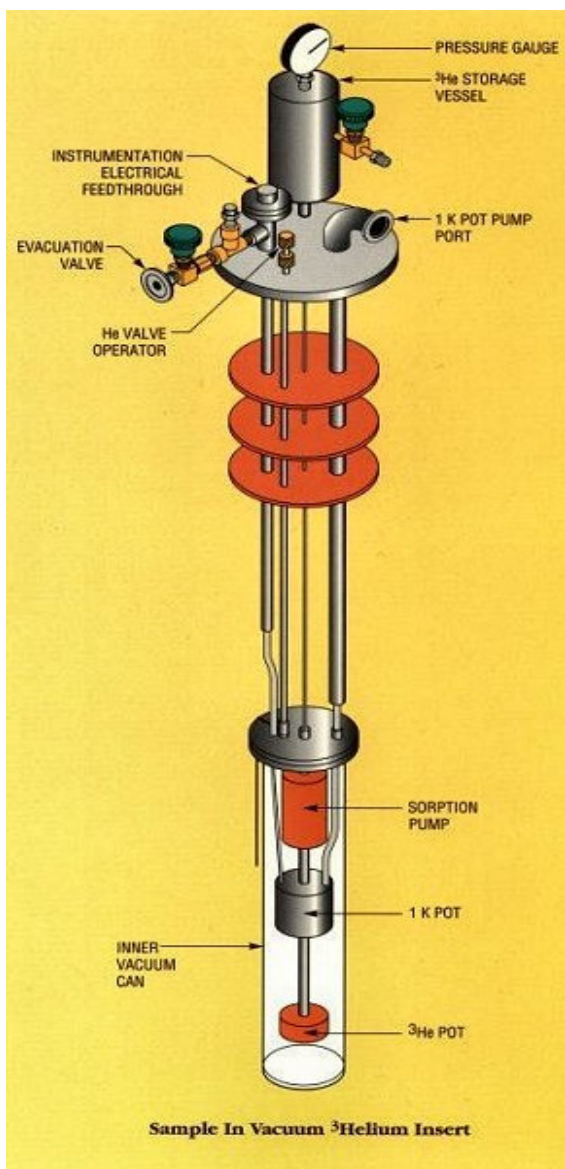


Figure 2.5 Schematic of our ^3He system as shipped directly from Janus Research Systems, company website. Our cryostat was fitted with 2 additional electrical feedthroughs at the top and we extended the vacuum can to accommodate a larger sample holder that was attached to the ^3He pot. The system contains a sealed vessel of ^3He that is connected by a stainless steel tube to the copper ^3He pot. This line passes through the sorption pump and 1K pot which are used in the condensing process. Once the ^3He is condensed in the ^3He pot, we can achieve ~ 285 mK temperature for up to 12 hours. The temperature increases to 350 mK if the 1K pot is not being pumped on. There are two small tubes on the outside of the vacuum can that let liquid/gaseous ^4He into the 1K pot/ sorption pump as well as an external connector for the sorption pump that are not depicted in this drawing.

With the sample(s) loaded and the cryostat sealed and filled with a small amount of gaseous ^4He it is ready to be lowered into the dewar. The dewar used is also equipped with a superconducting solenoid from Cryomagnetics[®] capable of generating magnetic fields up to 9T. If the dewar is empty it must first be blown dry by forcing nitrogen through the dewar's fill line and letting the exhaust vent into the room through the Helium recovery line connector until a room temperature stream of gas is achieved. This

will ensure that all water vapor has been removed. Next the cryostat is lowered into the dewar carefully and screwed into the top of the dewar to create a seal. As a precaution the sorption pump and 1K pot lines are opened up and nitrogen is blown through them to remove any water vapor. Next liquid nitrogen is flown into the fill line until the temperature of the 1K pot or sorption pump thermometers (see below) read $\sim 80\text{K}$. At this point the nitrogen flow is reversed and the dewar is emptied. When there is no more liquid nitrogen flow the fill line is sealed and the dewar is pumped on through the Helium return line connector until the pressure gauge on the dewar bottoms out. At this point there should be no appreciable amounts of liquid nitrogen in the dewar and we are ready to fill it up with helium gas. Helium gas is blown into the dewar through both the sorption pump and 1K pot lines on the cryostat. This ensures that both lines are unobstructed and free from any nitrogen. When the dewar is pressurized to atmosphere we are then able to fill the dewar with liquid helium to the desired level. Once the cryostat reaches 4.2 K it is then pumped on until it reaches 10^{-6} Torr to remove the exchange gas and ensure that there is no unintended thermal contact between the various temperature stages inside the cryostat.

If the dewar is already cold and filled with liquid helium the procedure is slightly different. Here we first insert the cryostat so that the sorption pump and 1k pot lines are about 12 inches inside the dewar. Helium is then blown through these lines to ensure that they are clear and they are closed to keep air out. The cryostat is then lowered very slowly into the dewar to conserve helium and to allow the vapors to cool it and is pumped on once fully cooled.

When the cryostat is at 4.2 K and is evacuated we are ready to start the condensation process. This can only be accomplished when the dewar filled with at least 12% volume of liquid ^4He , but lasts longer when the level is at least 60%. At the 12% level we can fill the 1K pot with liquid helium and pump on it to cool it down to $\sim 1.3\text{ K}$. At temperatures below $\sim 27\text{ K}$ ^3He adsorbs to the carbon in the sorption pump. By heating the sorption pump to $30\text{-}50\text{ K}$ we can cause the ^3He to outgas from the carbon. If this is done with a high thermal gradient, ie when the 1K pot is being pumped on, the gas flows to the 1K pot, is cooled below its condensation temperature (2.7 K ?) and liquefies in the ^3He pot. We keep this gradient present for ~ 30 minutes and then allow the sorption pump to cool back to $\sim 4\text{ K}$. After the condensation process is completed the

liquid ^3He that evaporates cools the ^3He pot and the sample block connected to it down to $\sim 285\text{mK}$. With the sorption pump cold, it will adsorb all the ^3He , present, effectively pumping on the ^3He pot. Depending on the conditions of the experiments, condensation can last well over 12 hours. Additionally, keeping the 1 K pot cold ensures the lowest possible temperature so care is usually taken to make sure that is so.

2.2.3 ^3He Cryostat: Wiring

The wiring of all thermometers, heaters and the 16 DC measurement lines as well as the fabrication of the sample holder was done by Andrey Rogachev (now at Utah). Figure 2.6 shows this in detail. All measurement lines are manganin wires and are grouped as 8 sets of twisted pairs. These wires run from the top of the cryostat to the sample holders at the bottom, passing through three silver paste filtering stages and a copper powder filtering stage to limit unwanted high frequency noise on the DC lines. The sample holder has 3 slots for chip carriers to be inserted. There is one at the bottom, which places the sample perpendicular the applied magnetic field if it is to be used and 2 slots on the side that place the sample parallel to the magnetic field. The bottom slot and the lowermost side slot have 6 DC lines available. The topmost side slot only has 4 slots and is typically used to connect our commercially calibrated RuO thermometer (Lakeshore). At the top of the cryostat a BNC box is connected to all the DC lines. This box contains an additional set of pi filters to further limit high frequency noise. In addition to the 16 measurement lines there is another series of wires used for the heaters and secondary thermometers. The sorption pump and ^3He pot are each equipped with heaters and there are thermometers on the sorption pump, 1K pot and ^3He pot to monitor the temperatures of the system. These lines are fed in through a separate feedthrough from the DC lines.

The microwave signal is fed in through an 0.85 inch SS coaxial cable. The cables used in the cryostat are UT-085-SS-SS purchased from Micro-Coax[®][4]. They are composed of a stainless steel jacket, a PTFE dielectric and a stainless steel center conductor. All ends of cables were connected to SMA connectors. The connectors used had snap on center conductor pins with solder-on male outer conductor connectors. Two of these cables were inserted through an empty feedthrough on the top of the cryostat.

One was used for these experiments, the second was added for experiments to be performed by Jaseung Ku, who also helped in constructing this. The coaxial lines were designed to be very modular so that components could easily be added as the need arose. The only components used for the experiments discussed here were attenuators. Attenuators were installed along the lines to limit the amount of thermal radiation coming in on the line. The coaxial line runs, unbroken from room temperature all the way down to the antenna at the bottom of the sample's Faraday cage. The attenuators were covered with a thin layer of vacuum grease and tightly wrapped in copper cable which was connected to the desired temperature stage. We used a -10 dB attenuator at 4.2K by connecting the copper wire to the top of the cryostat's vacuum can and we used a -3 dB attenuator which we connected to the 1K pot. When the system was cooled we found that the average base temperature changed from ~275 mK without any cable to ~ 280 mK with the cable connected to the sample can. We interpret this to mean that the attenuators are sufficient for our purposes.

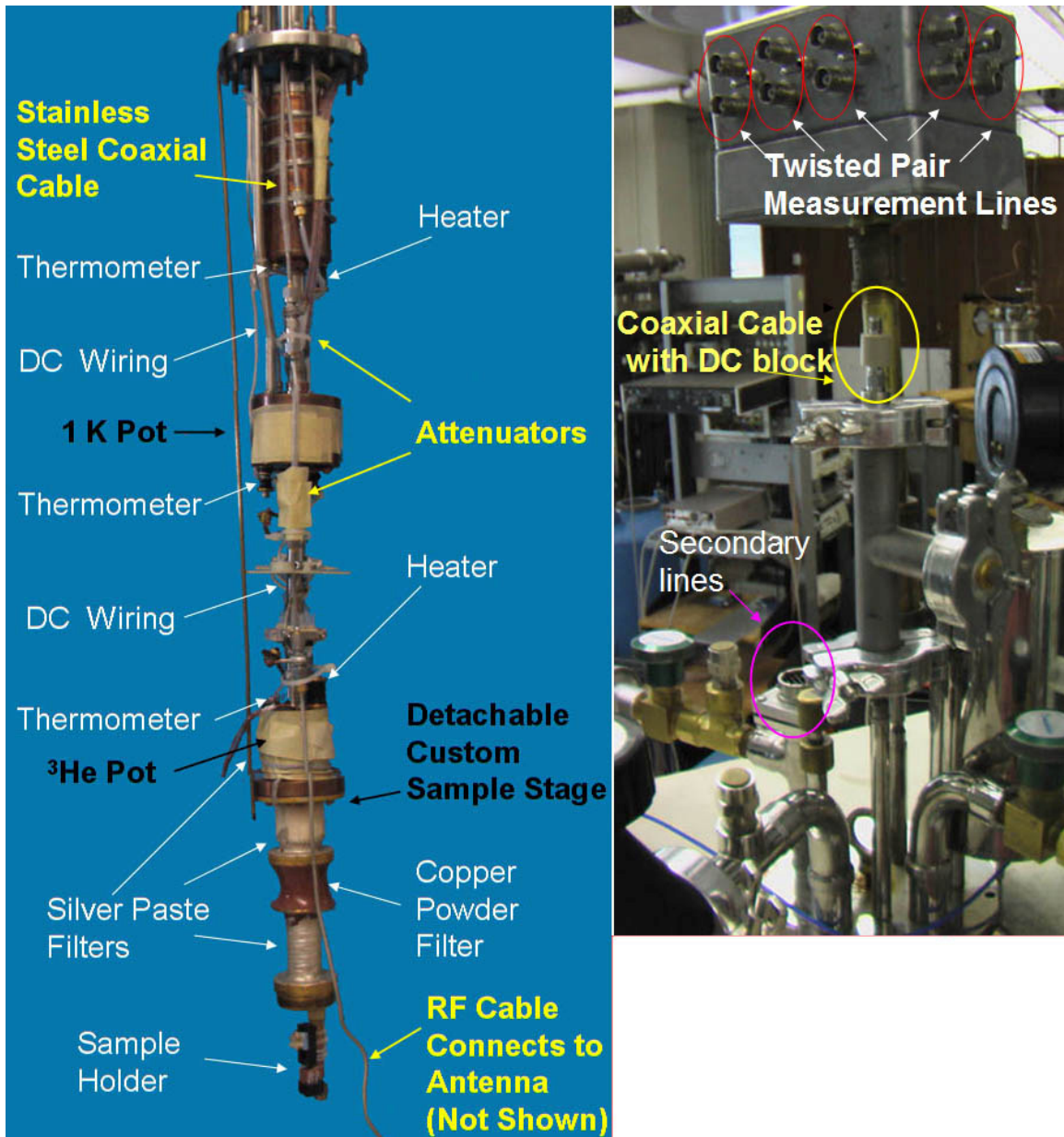


Figure 2.6 Left: Photo of the ^3He cryostat as configured for current experiments. The microwave components are labeled in yellow, the DC components are labeled in white and the mechanical components are labeled in black. Here there are 2 coaxial cables for AC transport measurements. The experiments described in this thesis used only 1 coaxial cable. Right: Photo of the BNC box with 5 of the 8 twisted pair connectors shown, coaxial cable feedthrough and secondary lines feedthrough.

2.3 Transport Measurements

All Samples are wired in a 4-probe configuration with each pair of voltage and current lines a twisted pair of measurement lines as detailed in Fig 2.7. The bias current is applied by an SRS DS 360 hooked up to a standard resistor. The voltage across the standard resistor and that across the sample are amplified using either an SRS SR530 or a PAR 113 preamplifier. The preamplifiers are battery powered and provide for additional filtering via their built-in high pass and low pass filters. The outputs of these preamps are fed into a BNC box connected to a DAQ board. Temperature is measured using a Ruthenium Oxide thermometer which is wired in a 4-probe configuration and measured using a Lakeshore 370A Temperature controller. This device also operates as a PID temperature controller. To achieve the desired temperature the output current is either wired to the ^3He pot or the sorption pump heaters. Using this device we are able to maintain temperatures within approximately 5mK.

The microwave signal is generated by a Gigatronics 1026 function generator. This device can output signals from -99 dBm to $+10\text{ dBm}$ for frequencies in the range of 1 MHz- 26 GHz. The signal is capacitively (and inductively) coupled to the sample through an antenna positioned at the bottom of the sample can. Because of this we were only able to study the sample's response at resonant frequencies, some of which may have depended slightly on the actual sample.

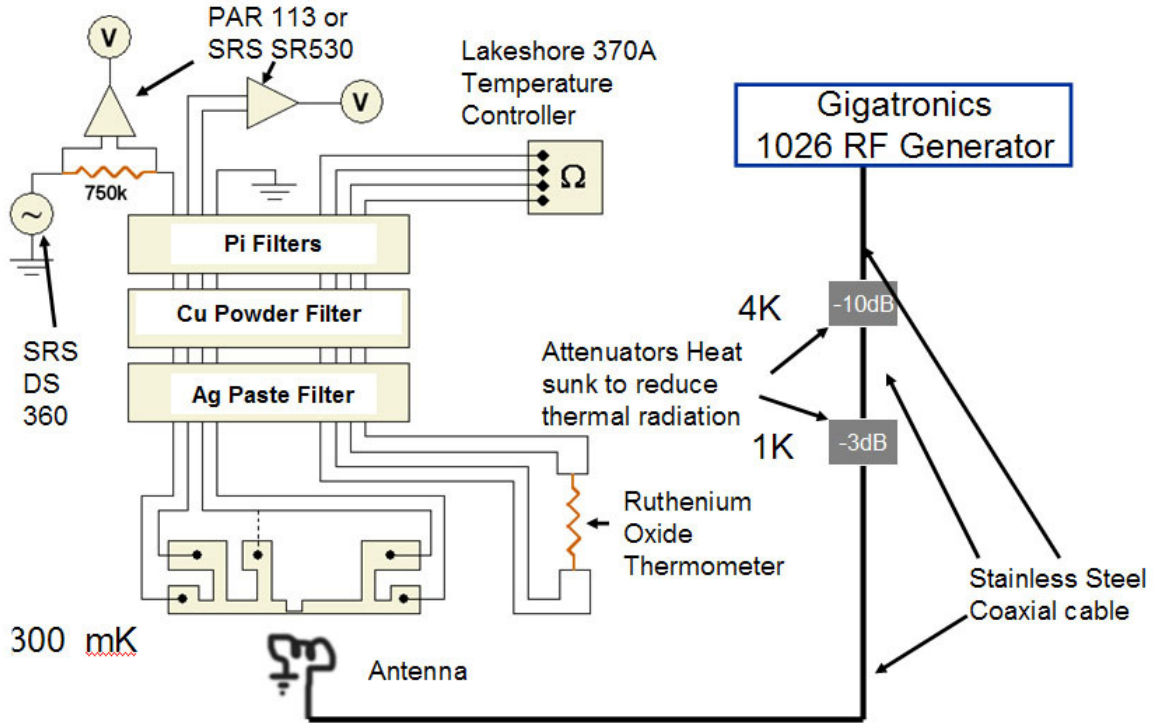


Figure 2.7 Schematic of our 4-probe transport measurement setup. A voltage is applied across a standard resistor from an SRS DS 360. This voltage and the one read from the sample are amplified with either a PAR 113 or an SRS SR530 battery operated preamp. The outputs of these preamps are wired to a BNC box that is connected to a PC via a DAQ board. The 750 k Ω standard resistor is a typical value as this component is interchangeable. The microwave signal is coupled to the sample via an inductive loop at the end of the coaxial cable. This loop is at the bottom of the cylindrical Faraday cage housing the sample.

The majority of our transport experiments were carried out using the BNC box and a LabView program which utilizes a lock-in technique. The voltage applied to the standard resistor is a low frequency (1-11 Hz) sinusoid and may or may not have a DC offset depending on the measurement. The applied voltage is used to measure the current and the measured sample voltage gives the voltage. Both signals are sinusoidal and are recorded for several periods by the program. For R vs. T , there is no DC bias current, but for dV/dI vs. I , I , is the applied DC offset (average) which is incremented as programmed to sweep the current over the desired range. For $V(I)$ curves this data suffices. For R vs. T and dV/dI vs. I curves, n measurements are taken for each data point and the differential resistance is found from the slope of the measured small segment of the $V(I)$ curve. The Resistance, R , or differential resistance, dV/dI , is then taken to be the average of a preset number of measurements. The program also computes the average of both the voltage

and currents and records them. The value of the current for dV/dI vs. I is such an average. Using this method enables us to average many measurements to improve the signal to noise ratio.

2.4 References

- [1] A. Bezryadin, C. N. Lau & M. Tinkham, *Nature*. **404**, 35010060 (2000).
- [2] A. T. Bollinger. Ph.D. Thesis, University of Illinois, (2005).
- [3] U. Coskun. Ph.D. Thesis, University of Illinois, (2005).
- [4] Originally the cryostat was fitted with cable UT-085-SS which has stainless steel outer conductor and silver plated copper weld as an inner conductor. This cable worked well but was replaced by the all stainless steel cable needed to further reduce any unintended thermal noise. This was necessary for more sensitive AC transport measurements involving 2 RF lines. There was no qualitative difference between the two cables with respect to the experiments discussed here. The base temperature using the cable with the SPCW center conductor was about 6 mK higher than it is with the stainless steel center conductor.

Chapter 3

Superconducting and Insulating Wires

In this chapter I will discuss some of the properties of superconducting and insulating nanowires. This was the first project that I worked on and was done in collaboration with Anthony Bollinger, Andrey Rogachev, Mitrabhanu Sahu and Matt Brenner. A great deal of this work was published here [1].

3.1 DC Transport Measurements on MoGe Nanowires

The resistance of our wires was measured using the procedure outlined in chapter 2. The R vs. T curves of samples with superconducting nanowires show 2 transitions. The first transition is the superconducting transition of the electrodes; the second is that of the wire. Wires are classified based on their R vs. T curves. Superconducting wires are wires which have shown a smooth transition and have a resistance that drops below the noise level of our setup. Samples with insulating wires show a smooth transition (as electrodes go superconducting) and, with further cooling, show an increase in the resistance as the temperature is lowered. Inhomogeneous wires are wires that show a lumpy transition. These wires may have either superconducting or insulating behavior, or even a mixture of both, but feature kinks in their R vs. T data [2]. Inconclusive wires are those that show an incomplete superconducting transition, i.e. R does not drop below the noise level for the lowest temperature they are measured at. These classes of wires will be fully explained in the following sections.

3.1.1 Superconducting Wires

The most studied class of wires is those that are superconducting. These wires have resistance measurements at or below the noise level of the system at sufficiently low temperatures and hysteretic $V(I)$ characteristics at temperatures well below T_C . Figure 3.1 shows a representative Resistance vs. Temperature measurement for a short wire, of length $L = 59$ nm along with fits to both variants of TAPS theories. The first thing to note is the transition at higher temperature corresponding to the film electrodes going fully superconducting. The 2-Dimensional film has a higher transition temperature than does a quasi one-dimensional wire. The wires are quasi one-dimensional because their cross sectional dimensions are each $\sim \xi(0)$ which is too small to support a vortex. Once the film transition occurs, we are only probing the resistance of the wire and we assume that the resistance measured after this transition is the normal state resistance of the wire, R_N . Both theories fit the data quite well but give different values for the fitting parameters, T_C and ξ for this particular wire. There is no strong case for one fit being better than the other based on the parameters alone, but in view of the objections to the LAMH model discussed in chapter 1, the Little model will be used in all further discussions. Also, there is an experimental indication that LAMH fits tend to overestimate the critical temperature of the wire [3]. Later in this chapter I will also discuss some numerical simulations on wires with some degree of geometric inhomogeneity and how it can affect the appearance of R vs. T curves.

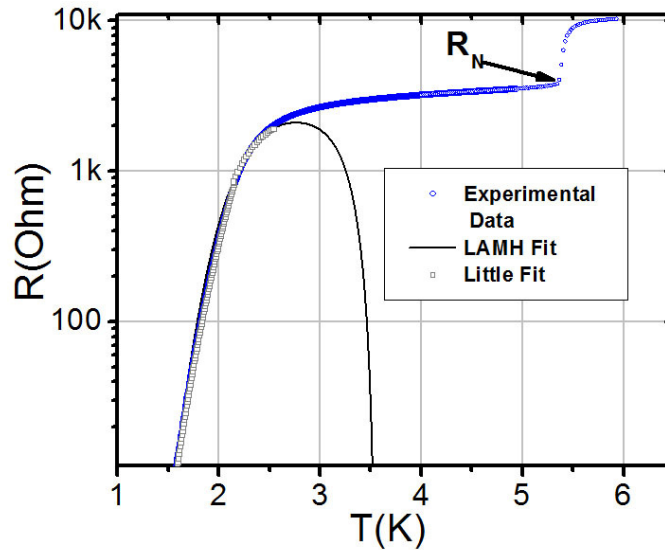


Figure 3.1 R vs. T plot for sample 082905H. The transition around 5.5 K is that of the film electrodes going superconducting; the second fast drop of the resistance is due to the wire becoming more and more superconducting (superconductivity of a thin wire is never perfect since at any nonzero temperature there is a finite, but possibly very small, rate of phase slips). The blue dots are data and the Black curve is a fit to TAPS (LAMH) theory, using $T_C = 3.35$ K, $R_N = 3790$ Ω , $L = 56$ nm, $\zeta(0) = 6.71$ nm (it would be good to check to which mean free path these numbers correspond to). The symbols (which symbols?) are a fit to the Little formula using $T_C = 2.6$ K, $R_N = 3790$ Ω , $L = 56$ nm, $\zeta(0) = 7.5$ nm. The value for R_N is taken to be the value of the sample right below the temperature at which the electrodes go fully superconducting. It is indicated with an arrow.

The voltage-current characteristics, $V(I)$ are plotted for temperatures between 358mK and 4.1K for a representative wire in Fig. 3.2. At temperatures far below T_C the $V(I)$ curves are very hysteretic. For these temperatures as the current is increased from 0 the wire remains superconducting until it reaches a critical switching current, I_{SW} , where it exhibits a sharp jump to a finite voltage state. This state is a normal state created by heating of the wire above T_C and as such will be referred to as a Joule Normal State (JNS)[4, 5, 6]. The switching current is highly stochastic at low temperatures and features a distribution with an increasing standard deviation for decreasing temperatures. The curve in Fig. 3.2 shows 2 different switching transitions at negative bias currents for $T = 600$ mK because of this stochasticity. Once the wire switches into the JNS it remains normal until the current is decreased below the return current, I_R . The return current is

the current at which the Joule heating is insufficient to heat the wire to temperatures above T_C . This current is determined almost entirely by the thermal properties of the wire and is nearly deterministic, since many electronic degrees of freedom are involved in the condensation of normal electrons. The stochastic and deterministic natures of these transitions will be discussed in more detail in chapter 4 as well as the effect that microwave radiation has on this transition. As the temperature is increased from very low to intermediate values the first thing that happens is that the switching current becomes suppressed. At higher temperatures still the return current decreases as well. At some intermediate temperature there is a small finite voltage tail that appears at currents slightly below the switching current. These tails can be seen in the inset of Fig. 3.2 and are caused by thermally activated phase slips [7]. They provide a proof that the switching to the JNS takes places, in general, after more-than-one phase slip occurred in the wire. For temperatures approaching T_C the hysteresis vanishes and as the temperature is increased until these curves slowly lose all non-Ohmic character.

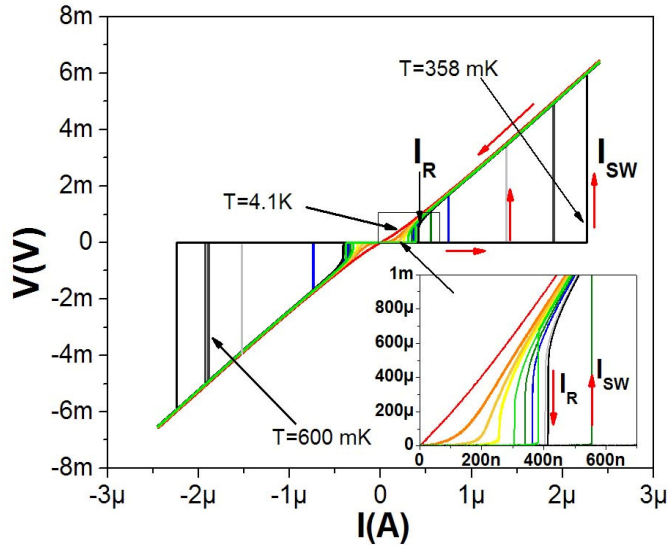


Figure 3.2 Voltage-Current Characteristics for sample 120207C for Temperatures between 358mK and 4.1K. The red arrows indicate the direction the current is swept. Inset: Zoomed-in view of the boxed region showing the appearance of tails in the curves starting with the green curve corresponding to $T=2.4$ K and the disappearance of hysteresis.

3.1.2 Insulating Wires

When thinner wires are fabricated, some of them show an increase in resistance as the temperature is lowered. We call these wires insulating due to this behavior but they may also be called “metallic” or “normal”, since their resistance is not infinitely high but of the order of $10\text{ k}\Omega$. A representative resistance vs. temperature plot is shown in Fig. 3.3 (a) showing a slight upturn in resistance as temperature is decreased below 700 mK . As can be seen in Fig. 3.3 (b), the differential resistance, dV/dI shows a characteristic peak at zero bias current. All wires that show a single upturn in resistance and a peak at zero bias current in the differential resistance are classified as homogeneous insulating wires.

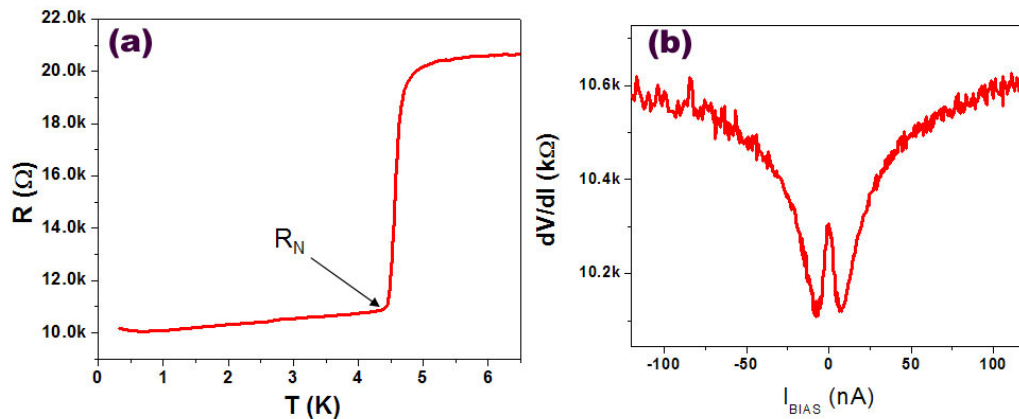


Figure 3.3 (a) Resistance vs. Temperature for sample 022106E with normal state resistance is indicated = $10.7\text{ k}\Omega$. This sample shows an upturn in resistance for decreasing temperatures below 0.7 K . **(b)** Differential resistance, dV/dI vs. bias current for sample 021106B taken at 300 mK .

The cause for this insulating behavior is thought to be proliferation of quantum phase slips (QPS) in wires with normal state resistance, $R_N > R_C \sim R_Q = h/4e^2 = 6.5\text{ k}\Omega$ [1]. In other words, the wires with resistance above some critical value R_C are insulating and the

critical value is approximately equal to the quantum resistance. For wires in this regime the transport properties are controlled by a Coulomb blockade tunneling mechanism [8, 9]. The leads are superconducting at low temperature and low applied magnetic fields and are connected by a short nanowire, which can be represented by a large number of diffusive conducting channels allowing electrons to tunnel from one lead to another. The Coulomb blockade occurs because as an elementary charge transits through the wire, the charge on one of the leads increases while the charge on the other lead decreases. This corresponds to an increase of the electrostatic energy of the system and leads to a suppression of the electrical current through the nanowire. Basically this happens due to the fact that the charge is discrete. Since in our situation the leads are large, the Coulomb blockade is dynamic, in the sense that the situation with increased electrostatic energy does not exist indefinitely, but only for a short time immediately after the tunneling of an elementary charge through the nanowire occurred. This system is modeled using the model of dynamic Coulomb blockade developed by Kauppinen and Pekola (KP). The model is shown in Fig. 3.4 [8]. There is a microscopic theory by Golubev and Zaikin (GZ) that can also be used to model our system. Since the KP model, which is simpler, provides a good description of our data, we focus on this model here. I refer the reader to the literature for discussions of the GZ model [9, 10].

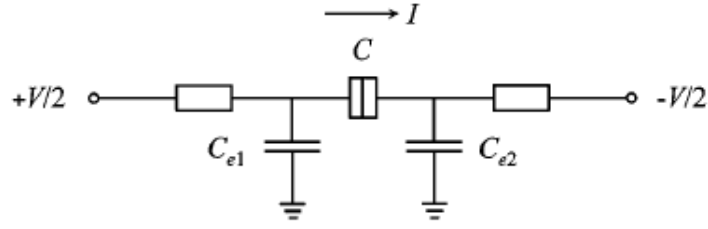


Figure 3.4 Schematic Diagram of the model by Kauppinen and Pekola [8]. In our nanowire system the wire is the central element which is modeled as a tunnel junction having certain capacitance C . The value of the capacitance in our case is determined by the geometry of the leads and not the geometric characteristics of the wire. The wire itself is considered as a point-like scatterer. This capacitor has one important property that it The capacitances $C_{e1,2}$ are taken to be equal.

The conductance of this system is described by the formula below which is valid for weak Coulomb blockade, i.e. when the charging energy is lower than the thermal energy, i.e for $q^2/2C \ll k_B T$. In other words, it describes small corrections to the Ohms law occurring in when the current is flowing through a nanowire.

$$R_N G = 1 - \frac{q^2 / C_{eff}}{k_B T} \left\{ \frac{v \sinh(v) - 4 \sinh^2(v/2)}{8 \sinh^4(v/2)} \right\} \quad (3.1)$$

With q , the charge of the charge carriers in units of e , G , the conductance of the channel, k_B , the Boltzmann constant, T , the temperature and $v = qV/k_B T$. The effective capacitance $C_{eff} = C + 1/2C_e$ between the leads is determined by a “horizon”, discussed in ref. [8]. In our case we estimate it as the mutual capacitance of the thin-film electrodes immediately attached to the nanowire. The voltage V is the voltage between the superconducting leads attached to the wire. If the leads are superconducting it does not matter which points on the leads are selected for voltage measurements. If the leads are not fully superconducting, as is the case in high magnetic fields, then Resistance vs.

Temperature measurements are used to infer the normal state film resistance and the voltage drop across the leads is subtracted off.

The zero bias behavior of the wire can be studied as a function of Temperature using the following formula which is the zero voltage limit of equation 3.1.

$$(1 - R_N G)^{-1} = \frac{18 C_{eff} k_B T}{e^2} \quad (3.2)$$

Using this formula we can fit data obtained from Resistance vs. Temperature measurements. Figure 3.5 shows such fits for 3 insulating samples and the values for C_{eff} that give the best fits for the linear region.

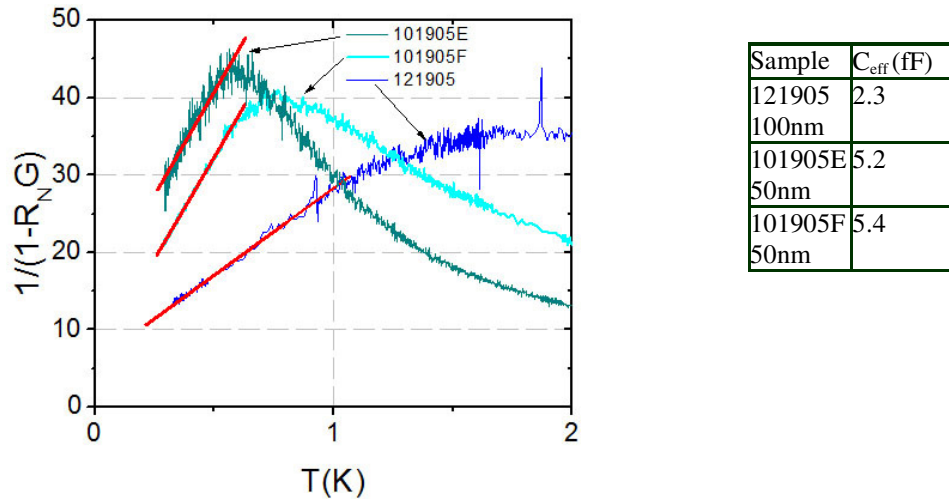


Figure 3.5 Fits of equation 3.2 for different temperatures for three samples as indicated. The fits are linear and valid only for low temperatures. At higher temperatures some additional contribution to the sample resistance, possibly due to weakening of the superconducting proximity effect, occurs in such samples. The table shows the value of the capacitance in fF used as a fitting parameter and the length of the trench used to fabricate the wires. The capacitance does scale appropriately for other samples analyzed in this manner.

The behavior of the insulating wire system is also very interesting when a magnetic field is applied to it. Figure 3.6 shows data for sample 101905E which is a sample classified as insulating and measured at different applied magnetic fields. The field was applied so that it was perpendicular to the film electrodes and perpendicular to the wire axis. The most pronounced effect of the magnetic field is the strong increases of

the sample resistance. Mostly it is due to the fact that the thin-film leads are measured in series with the wire and as magnetic field is increased superconducting vortices enter the leads and make them resistive. Superconductivity in the leads is suppressed as the field reaches $\sim 9\text{T}$. At these high fields the film is normal and its differential resistance is not current dependent. Thus, at fields as high as 9T , the variation of the differential resistance with the bias current is solely due to the nanowire. To analyze these experiments we take dV/dI data to get $G = dI/dV$ and use equation 3.1 with q and C_{eff} as fitting parameters. The results of this fitting procedure are shown in Fig. 3.7 for sample 101905E. The interesting thing to note here is that the best fitting value for q is greater than one for the zero field case, whereas when the field is at 8.5 Tesla $q = e$ gives a good fit. We do not have a definite explanation to this observation. A tentative explanation is based on the fact that the wire analyzed are insulating. Thus a coherent superconducting condensate does not exist in such wires. The transport is carried by normal electrons. But, if the leads are superconducting, normal electrons experience Andreev reflection at point where the normal (insulating) wire is connected to the superconducting leads. Such phenomenon effectively leads to doubling of the effective charge. Since the probability of Andreev reflection is less than one, the effective charge needed for the fitting is between e and $2e$. As magnetic field is applied, the leads become normal and Andreev reflection can not occur. All current is carried now by independent single electrons and the effective charge becomes e .

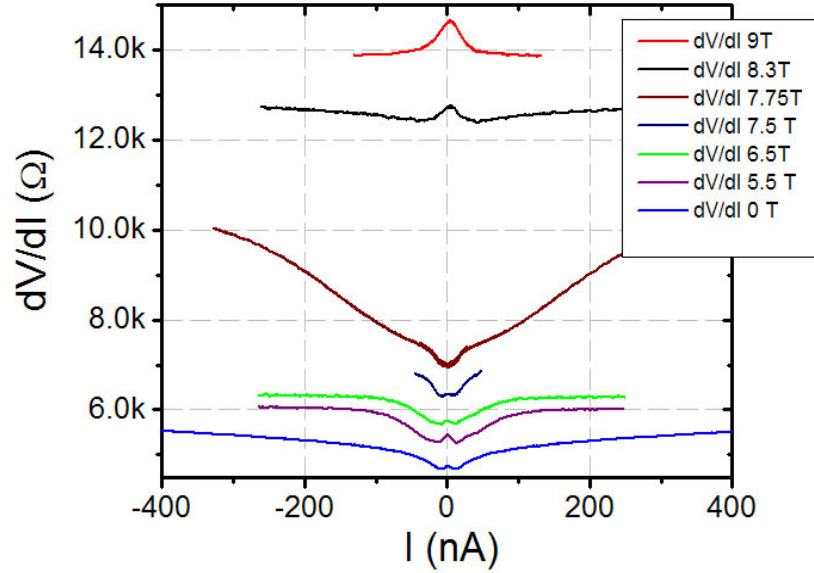


Figure 3.6 Differential resistance vs. Bias current measurements for sample 101905E measured at different values of applied magnetic field. The field strength is indicated in the legend and increases from 0 for the bottom graph to 9T for the top graph. The zero bias peak disappeared for intermediate field strengths. This is attributed to vortices entering the film, causing the peak to be smeared out.

So far in this chapter I have discussed the transport properties of superconducting and insulating nanowires. There is a clear distinction between the two classes of wires. In the next section I will discuss the physical reasons behind this difference.

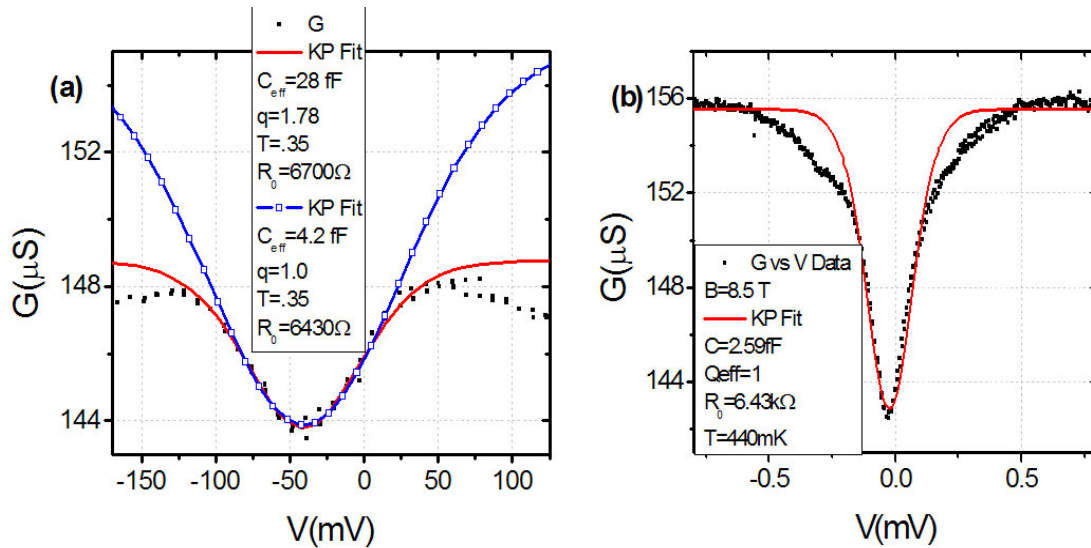


Figure 3.7 Conductance vs Voltage for sample 101905E with temperature as indicated along with fits to the Kauppinen-Pekola formula with fitting parameters indicated. R_0 is the fitting parameter for R_N in equation 3.1 (a) Results for zero applied field. Here one fit is performed with forcing $q = 1$ and the second fit is performed using a best fit algorithm in Igor Pro with q being a free fitting parameter. (b) Results for an applied field of 8.5 T. Say what is the normal resistance in (a).

3.2 The Superconductor – Insulator Transition in Quasi-One-Dimensional Wires

I have already discussed superconducting nanowires and the thinner insulating wires that we are able to fabricate and study. But what is it that causes a wire made out of a continuous, homogenous superconducting metal or alloy to become an insulating wire rather than a superconducting wire. One possible reason is that our insulating wires are simply too thin so that they may not be uniform and continuous due to granularity or over oxidation. The nanowires, even if perfectly homogeneous, may also have a transition from a regime where QPS are infrequent and hence have little bearing on their transport properties to a state where the QPS rate is so large that the wire is always normal. Another possibility is that our quasi-one-dimensional wires exhibit a dissipation-

driven quantum phase transition similar to that one observed in shunted Josephson Junctions described by McCumber-Stewart (RCSJ) model, where the total resistance of the shunt, R_N , determines whether the wire is superconducting or insulating [11, 12, 13]. This theoretical description is based on the famous result by Caldeira and Leggett who showed that a quantum system with dissipation will show macroscopic quantum tunneling (MQT) if the effective viscosity coefficient in the quantum system is below some critical value [14]. The critical value is given by the quantum resistance $R_Q = h/(2e)^2 = 6.45 \text{ k}\Omega$. The shunted junctions are superconducting if $R_N < R_Q$ and insulating otherwise. Equation (1.8) is a differential equation for the phase evolution in the RCSJ model. It is the tunneling of this phase variable leads to a decay of the supercurrent and to the loss of a purely zero-resistance behavior. If Josephson Junctions (JJs) have a shunting resistance greater than this critical value then the dissipation for the phase evolution is too low and MQT happens in the form of a quantum phase slip, otherwise there is enough dissipation to prevent QPS. This result was verified experimentally by Penttilä [15] and the two-dimensional (2D) analog was also observed in thin films [16]. This theoretical result was extended to 1D wires with the result that the normal state resistance of the wire controlled the transition [17]. Similar to JJs, nanowires with $R_N > R_Q$ are expected to be insulating because there is not enough dissipation to prevent QPS whereas wires with $R_N < R_Q$ are expected to be superconducting because QPS are suppressed.

To test whether or not this model describes our nanowires we fabricated many dozens of wires and measured their DC transport properties. The samples that were included in this study came from all members of our research group who worked on superconducting and insulating wires prior to 2006 [18]. Figure 3.8 shows all of the wires fabricated by myself in an attempt to produce 50 nm wires with a normal resistance as close to R_Q as possible that were included in this study [1]. To produce these wires the film thickness was tuned by varying the sputtering time and wires were chosen based on their estimated dimensions from the SEM images. Using this technique several wires were fabricated with resistances between 4 and 8 $k\Omega$. Each wire that could be classified as superconducting or insulating was then used to construct a phase diagram. These wires along with dozens of other samples were carefully scrutinized for their inclusion in the

phase diagram, in order to eliminate non-homogeneous wires, since this was our goal: to verify the existence and the properties of the SIT quantum phase transition in homogeneous or almost-homogeneous wires.

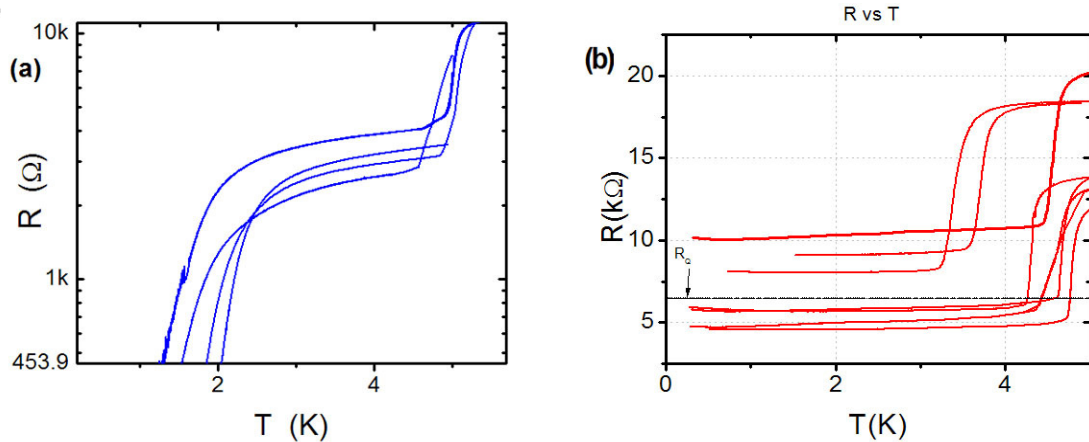


Figure 3.8 (a) R vs. T data for all 50nm Superconducting wires fabricated by myself that were candidates for inclusion in the phase diagram. The noise on the R - T curve with the lowest transition temperature was caused by filling the dipstick with He and pumping on it to lower the Temp from 1.5K to about 1.2K. (b) R vs. T data for all insulating wires I contributed to the diagram. These 11 samples as well as some wires made while the paper was being written represent my experimental contribution to the phase diagram paper [1].

Each sample was carefully examined before including it on the phase diagram. Nanowires which showed signs of inhomogeneity were not included. The Scanning Electron Microscope images were measured using a micrometer to ensure that all lengths were taken as the distance between ends of the white spots (see Ch. 2). Superconducting wires had to meet two criteria. The first is that resistance measurements needed to reach the noise level of our system. Some wires did not show this in our 1.5 K test system and did not survive the transfer to the He3 system. The second is that they do not show any signs of inhomogeneity in the form of multiple transitions [2]. An insulating wire was classified as insulating if it showed a single upturn in the R vs. T data and a zero bias peak in the dV/dI measurement.

Figure 3.9 shows Resistance vs. Temperature data for all samples that were not included in the phase diagram. These wires were broken up into 3 categories; inhomogeneous wires (Fig. 3.10), inconclusive wires (Fig 3.11), and anomalous wires

(Fig 3.12). Inhomogeneous wires are those that show signs of multiple superconducting transitions or a superconducting transition and then an insulating transition. These wires are believed to be inhomogeneous due to a defect or some type of damage that occurred prior to measurement. Previous work done in our group showed that wires that were deliberately made to be inhomogeneous showed the same type of multiple transition behavior [2]. In addition to this experimental evidence that inhomogeneity causes the superconducting transition to broaden and appear lumpy, I will present some numerical results in the next section of this chapter that also strengthens this assertion. Inconclusive wires are those samples that do not show a definitive superconducting state (Resistance at or below our measurement noise level) or a clear insulating upturn or peak in dV/dI . These wires were not measured in our ^3He cryostat and were not included in the phase diagram because there was not enough evidence to classify them. The final class of wires were those that were anomalous. These wires were simply hard to classify and were not clearly superconducting or insulating like the vast majority of other wires. In the end only 2 such wires were found. They are believed to be either suffering from some hidden inhomogeneity or simply not well-attached to the leads.

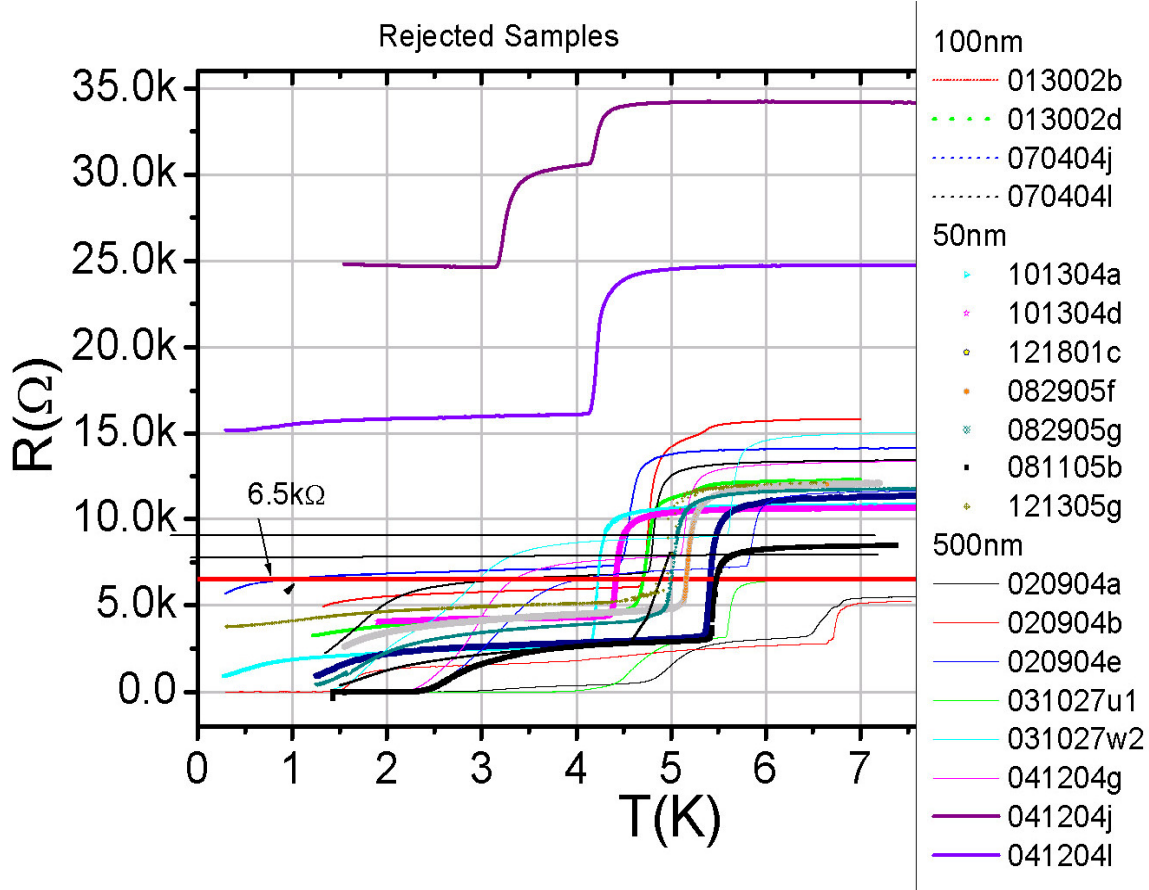


Figure 3.9 Resistance vs. Temperature data for the 19 samples that were not included in the phase diagram, which is shown in Fig??. The line representing $R = 6.5 \text{ k}\Omega$ is the red horizontal line indicated with an arrow. The sample numbers and trench size are indicated in the legend this length along with the angle the wire crosses the trench determines the length of the wire. The following 3 figures detail the reasons for their rejection.

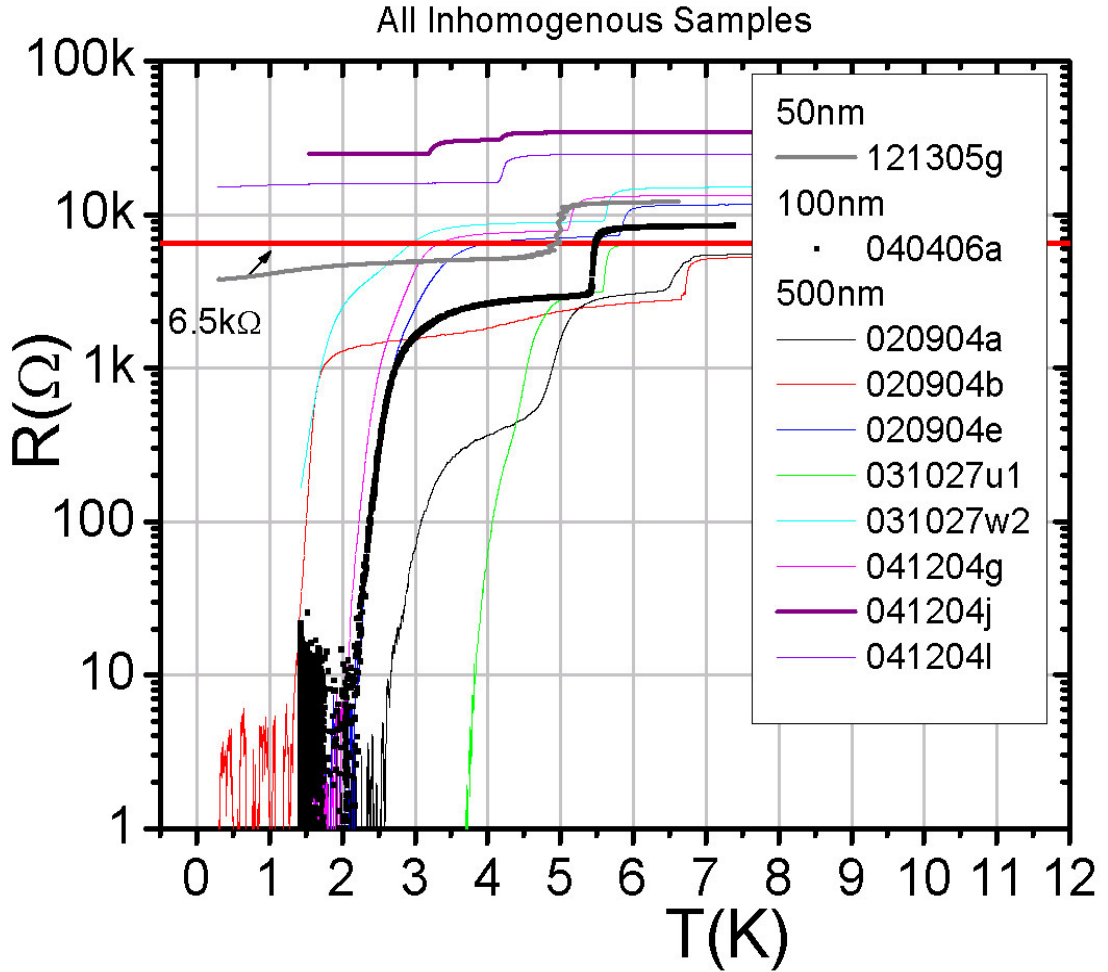


Fig 3.10 R vs. T data for all Inhomogeneous samples with the line corresponding to $R=6.5\text{ k}\Omega$ as indicated. Inhomogeneous wires show signs of multiple superconducting transitions or a superconducting transition and an insulating resistance upturn. Most of the inhomogeneous wires are those fabricated using 500nm trenches indicating that our fabrication method may not work as well for longer wires or that they are somehow damaged between fabrication and

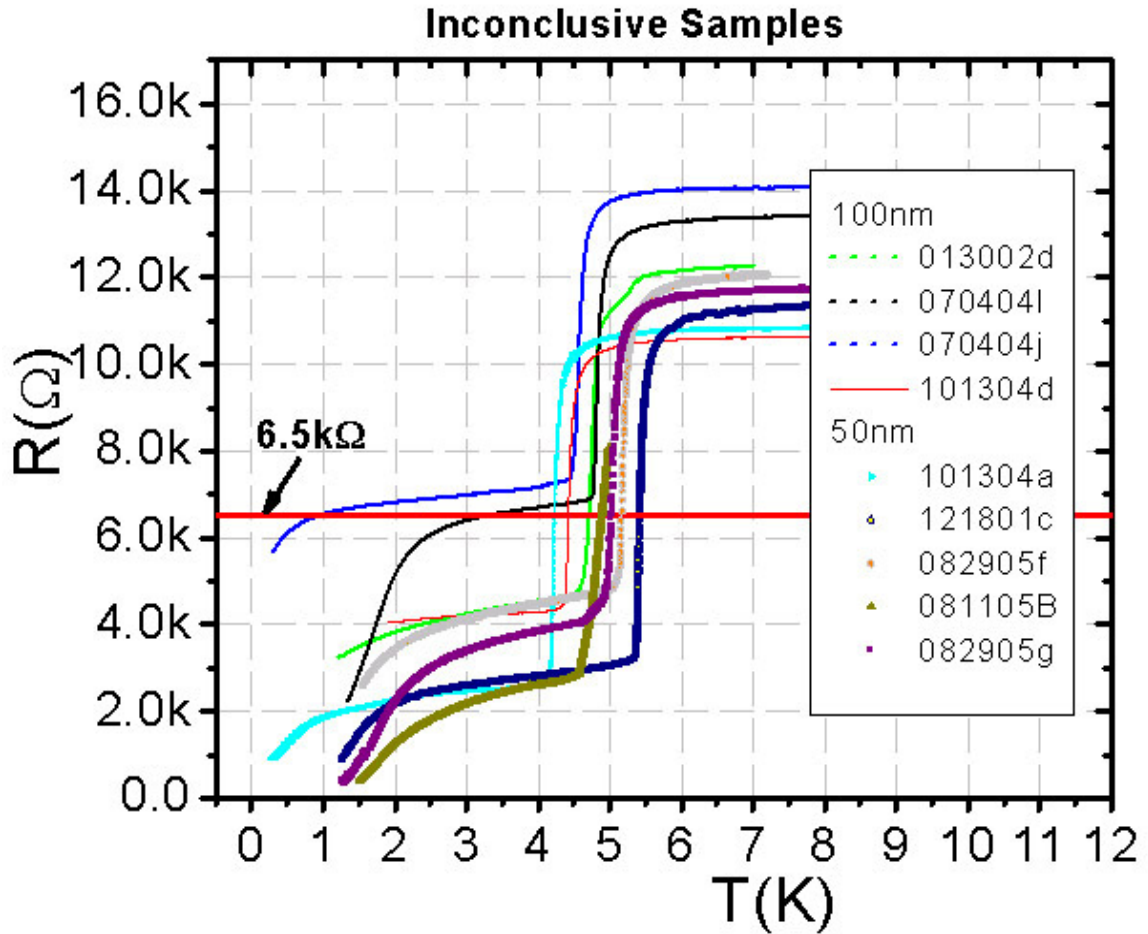


Figure 3.11 *R vs. T data for all Inconclusive samples with the line corresponding to $R = 6.5 \text{ k}\Omega$ as indicated. Inconclusive samples are those samples that may have been classifiable as superconducting or insulating if they were measured down to lower temperatures. Most samples in this category appeared to be superconducting wires that were only measured to 1.5K which was not cold enough for the wire to complete the superconducting transition and go below the noise level which is 1-5 Ohms.*

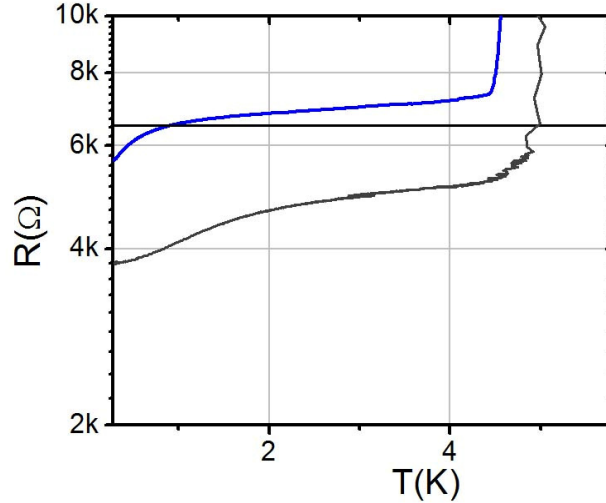


Figure 3.12 R vs. T data for wires categorized as anomalous samples with the line corresponding to $R= 6.5 \text{ k}\Omega$ as indicated. These wires were difficult to categorize and were mentioned as possible outliers on the phase diagram.

Once all the data were confirmed the phase diagram was constructed to see if a clear transition could be found based on either cross sectional area or the normal resistance of the wire. Figure 3.13 is the final version of this phase diagram. The data are plotted against the axis L/R_N , which is proportional to cross sectional area of the wire, and the wire length L . From the figure one can see that the line formed by $R_N = R_Q$ separates the insulating wires from the superconducting wires quite well for lengths less than 350 nm. Longer wires are not expected to follow the $R_N = R_Q$ separation while shorter wires are expected to exhibit an SIT quantum transition at $R_N = R_Q$ [17]. Theory explains this behavior by the presence of QPS-antiQPS dipoles. In shorter wires with $R_N < R_Q$ these QPS-antiQPS dipoles are bound due to dissipation. This results in no free QPS and thus a fully superconducting state at $T=0$. For wires with $R_N > R_Q$ the dipoles are free and the nature of QPS in the wire is determined by the fugacity of QPS. This fugacity, $\zeta \sim \exp(-bL/R_N)$ depends on the Length of the wire, L , its normal resistance and a constant, b . For short wires having resistance near the critical point R_Q this fugacity is large, leading to a proliferation of QPS and hence an insulating behavior. For sufficiently long wires (here also we are discussing the wires near the critical point $R_N \sim R_Q$) this fugacity is small and QPS are suppressed leading to apparently superconducting behavior even in wires with $R_N > R_Q$, which would appear insulating if an infinitely precise test would be

possible. Note also that it is not possible to choose a separatrix in Fig.3.13 that would be horizontal. This fact indicates that the critical point can not be defined simply as some critical wire diameter. In other words, the diameter is definitely not the only factor that controls the existence and rate of QPS. If that would be the case the separatrix would appear horizontal.

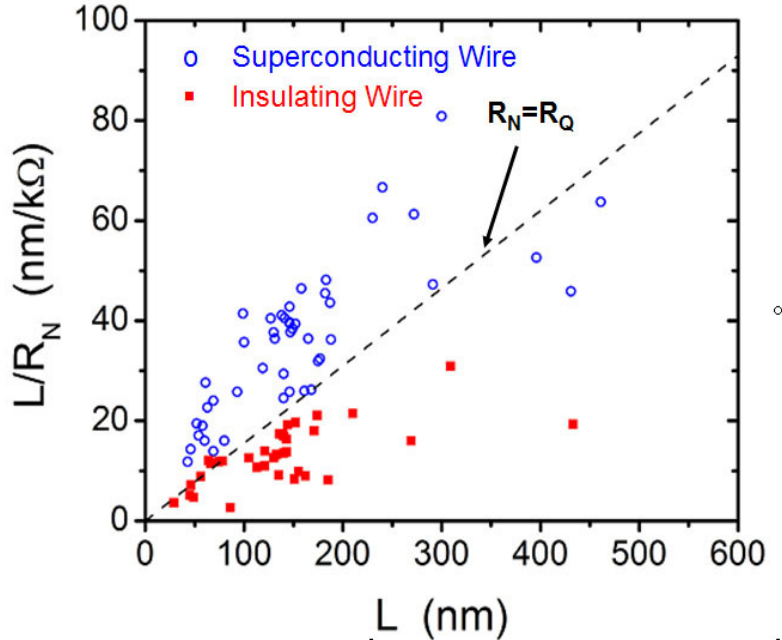


Figure 3.13 Phase Diagram for Superconductor – Insulator Transition in quasi 1-D wires. L/R_N is proportional to cross sectional area. The line $R_N = R_Q$ forms a very convincing separatrix for wires less than 350 nm long.

The evidence we present for a dissipation controlled quantum phase transition as predicted by theory [11, 12, 13,17] is quite strong, however there is still some slight deviations, most notably in really short wires that are insulating and have $R_N < R_Q$. This could be due to our not precise knowledge of the wire normal resistance, due to the influence of the film electrodes via some mechanism such as the proximity effect. The proximity effect, as noted earlier in this chapter, could cause the wire to effectively be shorter and thus have a lower measured resistance compared to its actual resistance. Another effect that could lead to deviations from the ideal phase diagram expected for the Schmid transition is the depairing surface effect. These wires are very thin so there might

be a critical cross sectional area, below which the order parameter of nanowires is suppressed to zero. All of our MoGe wires are exposed to atmosphere after the sputter-deposition of the metal. This oxide layer is approximately 3nm thick and the oxidation process quenches after this layer forms [2]. Recent work in our group studied the effect of this oxide layer which contains a high concentration of Oxygen which is known to be paramagnetic [19]. The authors of this study present evidence for the suppression of the critical temperature, T_C , in wires due to the presence of some localized spins or magnetic moments on the surface of the wire, possibly due to this Oxygen. The pair breaking effect that these magnetic dipoles have on the supercurrent in the wire causes T_C to be significantly lower than it would be if there were no magnetic moments present. An important parameter in their model is the surface concentration of magnetic moments. Treating the wire as a circular cylinder with this constant layer of magnetic moments it is easy to see that the surface concentration of magnetic moments, which is proportional to the surface area to volume ratio for the non-oxidized portion of the wire, depends strongly on the diameter of the wire. Their analysis estimates that T_C is suppressed to zero for wires with a diameter less than ~ 3.5 - 4.4 nm, because at this small diameter the effective volume concentration of spins is as high as is needed to suppress superconductivity according to Abrikosov-Gor'kov pair-breaking theory. From the diagram in figure 3.3 and an estimate for the resistivity of $\text{Mo}_{79}\text{Ge}_{21}$ of $180 \mu\Omega\text{-cm}$ we have no samples that are superconducting with a diameter below 4.4 nm.

3.3 Numerical Study of the Resistance vs. Temperature Behavior in One-Dimensional Wires

In this section I will present numerical results that were performed to try to understand the effects that inhomogeneities might have on the Resistance vs. Temperature curves of a thin wire. For this study a nanowire was modeled as a chain of independent segments each with their own values for T_C , ξ , R_N , A , L (see Fig. 3.14). The

resistance for each of the N segments of the with index, i , was computed using the Little formula (eq 1.29) which can be written as follows:

$$R_i(T) = R_{Ni} \exp\left(-\frac{1.76\sqrt{2}}{3} \frac{R_Q}{R_{Ni}} \frac{L_i}{\xi_i(0)} \frac{k_B T_{Ci}}{k_B T} (1 - T/T_{Ci})^{3/2}\right) \quad (3.3)$$

This equation reduces to the equation 1.29 for the case where all the T_C , ξ , R_N , A are the same for each segment and $L = \sum L_i$. The parameters R_N , L and A are related through the simple relationship $R = \rho L/A$, where the value for ρ was taken to be that of $\text{Mo}_{79}\text{Ge}_{21}$ which is approximately $180 \mu\Omega\text{-cm}$.



Figure 3.14 The wire is modeled as a series of N small one dimensional links, each with their own value of T_C , ξ , R_N , A , L . The resistance of each segment, $R_i(T)$ is given by the Little formula using the set of parameters chosen for numerical computation.

The primary reason for this work was to determine what effect, if any, a weak section of the wire would have on the overall R-T curve and to understand the role that each parameter played in the shape of the curve. A weak section of the wire can either be one with a lower T_C than the other segments of the wire or a smaller cross sectional area. Lowering the value of either of those parameters results in an additional kink on the $R(T)$ curves or in the resistance hitting “noise level” at a lower temperature. There are also some peculiarities in the fitting parameters we used when fitting experimental data with the Little formula or the LAMH formula. Several of the wires that were fit with either TAPS theory required the use of values of the coherence length that were much larger than the value in bulk $\text{Mo}_{79}\text{Ge}_{21}$ which is about 5 nm [20]. The value of the GL coherence length depends on the value of the critical temperature, T_C , as will be shown below.

In the dirty limit the GL coherence length is related to the Pippard coherence length, ξ_0 , and the electronic mean free path, l_e , as follows:

$$\xi(T) = 0.855 \sqrt{\frac{\xi_0 l_e}{1 - T/T_C}} \quad (3.4a)$$

$$\xi(0) = 0.855 \sqrt{\xi_0 l_e} \quad (3.4b)$$

Using equation 1.21 we can write $\xi = \xi(0)$ in terms of the BCS gap.

$$\xi_0 = \frac{\hbar v_F}{\pi \Delta(0)} \quad (1.21)$$

$$\xi(0) = 0.855 \sqrt{\frac{l_e \hbar v_F}{\pi \Delta(0)}} \equiv \xi_{BCS} \quad (3.5)$$

We can then use the well known relationship $\Delta(0) = 1.764 k_B T_C$, an estimated value for the Fermi velocity of 10^6 m/s, and 4 Angstroms for the mean free path (estimated to be 3-4 Angstroms [20]), to arrive at the following relationship for the coherence length:

$$\xi_{BCS} = \frac{20.38 nm}{\sqrt{T_C}} \quad (3.6)$$

The coherence length computed using equation 3.5 will be denoted, ξ_{BCS} , because it makes use of results from the BCS theory for the gap. This coherence length is simply the GL coherence length in the dirty limit with an explicit dependence on T_C .

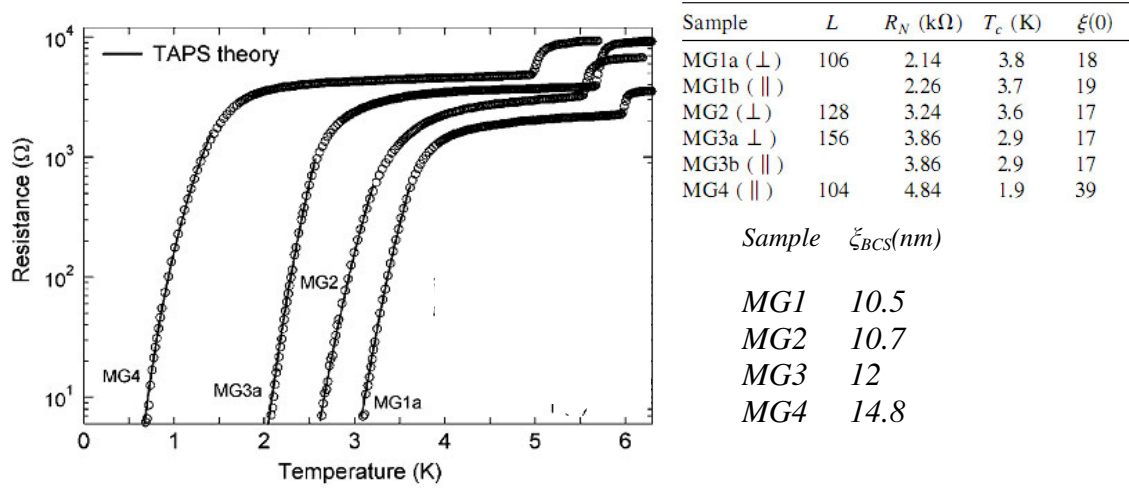


Figure 3.15 Resistance vs. Temperature data and fits to TAPS theory along with a table (top right) containing the relevant fitting parameters as they appeared in ref [19] with L and ξ in nm. The perpendicular and parallel symbols refer to the orientation with respect to the applied magnetic field in other measurements discussed in the publication. The lower table shows the value of ξ from the relationship $\xi_{BCS} = 20.38(T_C)^{-1/2}$

Figure 3.15 shows R vs. T data as it appears in Ref. [19] along with a table of the fitting parameters for TAPS theory as well as values of ξ_{BCS} computed using equation 3.6. Note the discrepancy between the computed values and those used for the curve fitting. To study this further, numerical simulations were performed to generate many model curves corresponding to wires with randomly generated parameters describing inhomogeneity. The parameters for the entire wire were set at the start of the computation. These global wire parameters are L , T_C , and R_N . From these parameters we can determine the average cross sectional area and the value for ξ_{BCS} . The number of wire segments, N , is then chosen and the average values for each parameter is then computed. The average values for each parameter for individual segments are; $\langle L_i \rangle = L/N$, $\langle R_{Ni} \rangle = R_N/N$, $\langle A_i \rangle = \rho L/R_N$, $\langle T_{Ci} \rangle = T_C$ and $\langle \xi_i \rangle = \xi_{BCS}$. With the values set and the averages computed we then performed a few simple numerical experiments. The results of one such numerical experiment are shown in Fig. 3.16. For these calculations the cross sectional areas for a ten segment wire were generated from a Gaussian distribution with mean $\langle A_i \rangle$ and increasing variance to produce model wires

with the desired variation in cross section. For these simulations all other parameters were chosen to be their average values and the areas were then rescaled after being computed to give the same total normal resistance as that chosen for the entire wire. After performing several such experiments, some even varying T_C , it was found that the weakest link had the greatest impact on the low temperature even for model wires with two rather thin segments (see Fig 3.17). For this reason the absolute relative deviation of the weakest link was chosen as the classifying parameter for these computations. This quantity is simply $\Delta A/A = (\langle A_i \rangle - A_{weak}) / \langle A_i \rangle$. The conclusions one can draw from Fig. 3.16 is that small deviations in the Area < 20% do not significantly alter the shape of the R vs. T curves, however, for variations greater than 25% the effect is noticeable. For a hypothetical wire with a very weak segment this could lead to a larger value for the coherence length if it was fit to TAPS theory assuming that it was homogenous. This effect can be seen by comparing the curves computed with no variation in area but with larger values for the coherence length.

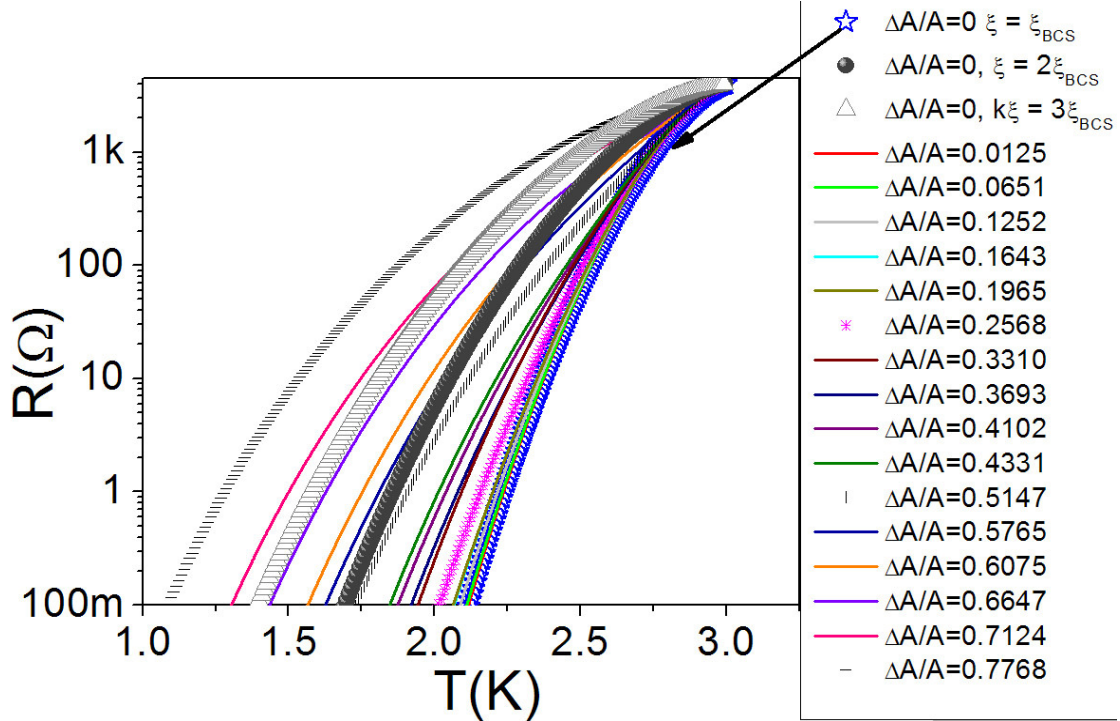


Figure 3.16 Numerical R vs. T curves for wire segments with randomly generated cross sectional areas. For this wire L was chosen to be 120 nm, $T_C = 3K$ and $R_N = 3k\Omega$. The quantity $\Delta A/A$ is the relative deviation of the smallest area from that of the average area A . The first 3 curves listed in the legend are with no deviation in area, but instead using a value for the coherence length different from the value given by equation 3.6. The curves with the relative deviation close to 25%, 50% and 75% are distinguished to aid in interpretation. It is notable that a cross sectional area that deviates by as much as 20% from the average value has very little effect on the shape of the R vs. T curve.

Many Simulated R vs. T curves were generated and then fit using TAPS theory. Figure 3.17 shows results for one simulated curve. Note how well the fit appears to be for lower resistances. The quality of this fit is very similar to that obtained using TAPS theory to fit experimental data. It is also interesting to note that the shape of the fitting curve closely follows the resistance of the weakest link at low temperatures. This result shows that a weak link may lead to an erroneous fit if the wire is assumed to be homogeneous and that ζ can assume any value.

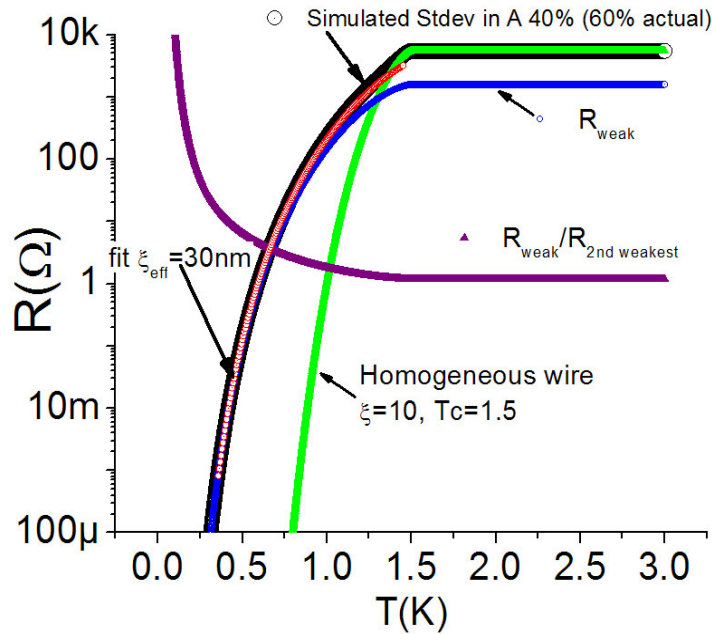


Figure 3.17 Simulation results for a 10 segment model wire with $L = 120\text{nm}$, $R_N=6\text{k}\Omega$, $T_C = 1.5\text{ K}$ with a chosen standard deviation for the cross sectional area to be 40% (60% actual deviation due to randomly generated values) The Resistance vs. Temperature is plotted for the simulated wire, the weakest link in that simulated wire and for a homogenous wire with the same L , R_N , T_C and ξ . The ratio of the resistance of the weakest link to that of the second weakest link is also shown. The simulated data is then fit using the parameters for the whole wire and finding the best value for ξ (denoted ξ_{eff}). In this particular case the fitting value for ξ is 3 times the value of ξ_{BCS} .

In an attempt to see if this idea could be applied to our actual experimental data, many resistance vs. temperature curves were analyzed using a different fitting procedure. Instead of assuming L and R_N and due to their dependence on each other, A , were fixed parameters for TAPS fits, they were allowed to vary and ξ was computed from T_C using equation 3.5. The fitting parameters then reduced to T_C , A_{WEAK} , and R_N with L and ξ constrained by the values of the 3 free parameters. When all the fitting was completed there were 2 sets of fitting parameters for the experimental curves, one for the fits based on the assumption that the wires are homogeneous and one for a fit assuming there was a weak link. For the simulated curves there was one set of data for fitting using the traditional curves and a set for the underlying structure of the simulated wire. From this information Fig. 3.18 was constructed to see if the two models produced consistent results for the experimental and numerical data sets. Figure 3.8 shows the ratio of

coherence lengths needed to fit the data assuming a homogeneous wire to that from equation 5 and compares that to the ratio of the deviation in the cross sectional area for a non homogenous wire to that of a homogenous case. This does not give evidence for favoring one method to the other only that the simulated data set shows results consistent to experimental data when the two analyses are compared.

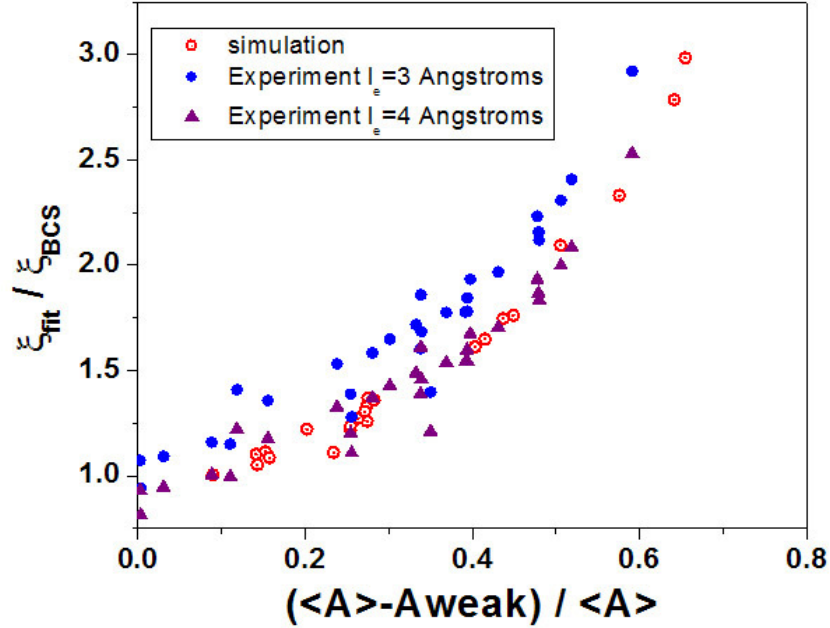


Figure 3.18 Comparison between TAPS fitting procedures for experimental data and numerical simulations. The ratio of coherence lengths used for the different fitting procedures is plotted vs. the relative deviating in cross section for a weak link. The experimental data were analyzed using equation 3.5 for 2 values for the mean free path, whereas the simulated curve used $l_e = 4$ Angstroms. The quantity ξ_{fit} is the coherence length used as a fitting parameter assuming the wire was homogenous and ξ_{BCS} is obtained from equation 3.5. The trend in the simulated data set shows that for increasingly weak links, one can fit the data using a larger ξ_{fit} . Or in other words weak links can lead to the effect we see in our experimental data that forces us to conclude ξ is considerably larger for thinner wires than it is for thicker wires or in films.

Using the TAPS fits based on a weak link a new set of fitting parameters were obtained for our wires. These parameters were analyzed to determine whether or not we could provide evidence that weak links dominate the resistive transition as opposed to our assumption that the wires are homogeneous. Figure 3.19 shows the comparison between values of T_C and of $I_C(0)$ obtained using the 2 methods of analysis [21]. The values for

$I_C(0)$ remain essentially unchanged, however the T_C values do shift lower and the set appears to have more of a correlation to the diameter .

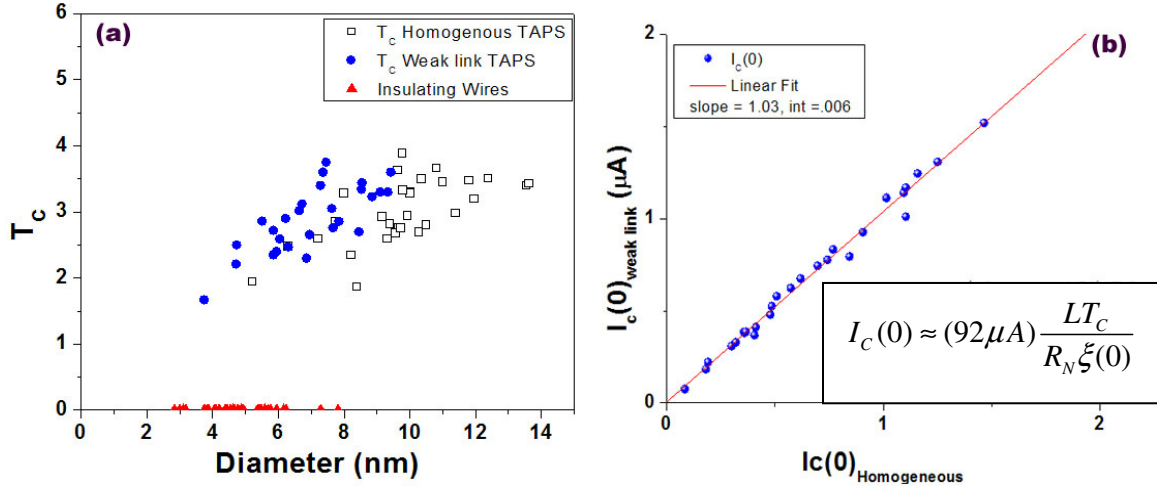


Figure 3.19 Comparison between T_C and $I_C(0)$ for the different TAPS fitting procedures. (a) T_C vs. Diameter for the different fitting procedures. The diameter of the weak link is used for the weak link fitting method. Insulating samples are plotted here for comparison and their diameter is computed based on their resistance. A considerably overlap of the family of superconducting and the family of insulating wires is observed in terms of their diameter values. So there is no way to infer whether or not there is some sort of critical diameter using this analysis. (b) $I_C(0)$ is computed for the weak link method and plotted against $I_C(0)$ obtained using the homogenous fit.

The fact that we can fit wires assuming a there is a weak link does not give us enough evidence to prove one treatment of the data is better than the other. On the other hand, the previously published analysis of the correlations between the normal state resistance and the apparent diameter of the wires (both insulating and superconducting) indicates that the wires are homogeneous [22, 23]. With recent advancement in fabrication techniques [24] it is possible to intentionally damage wires and study their behavior. Preliminary data suggest that by artificially creating a weak link in the wire the shape of the $R(T)$ curve changes qualitatively and can not be fit with a TAPS theory even if the coherence length is taken as a free parameter. This is because in the wire with the artificial weak link it was observed that the curvature of the $\ln(R)$ vs. T curve is positive

at low temperatures while in any TAPS model it is always negative (due to the presence of the Boltzmann exponent).

This concludes the introductory chapter on transport measurements for MoGe nanowires. I have discussed superconducting wires, insulating wires and wires that were inhomogeneous or inconclusive. I have presented evidence for a dissipation controlled quantum phase transition in the form of a very careful analysis of many dozens of samples. In addition to experimental work I discussed a small numerical study that shows some evidence that inhomogeneous wires may have broader R vs. T curves and if fitted with a model written for homogeneous wires can give an anomalously large coherence length. Yet, the entire scope of evidence we have (including measurements on wires with artificial weak links and the analysis of the normal resistance of wires) indicate that our wires are homogeneous (except those which show explicit signs of inhomogeneity such as multiple bumps on the $R(T)$ curves, and which were excluded from the diagram of Fig.3.13). In the next two chapters I will focus on the main topic of this thesis: transport properties of superconducting nanowires in the presence of microwave radiation.

3.4 References

-
- [1] A. T. Bollinger, R.C Dinsmore III, A. Rogachev, A. Bezryadin, *Phys. Rev. Lett.* **101**, 227003 (2008).
 - [2] A. T. Bollinger et. al., *Phys. Rev. B* **69**, 180503(R) (2004).
 - [3] Sang L. Chu, A. T. Bollinger, and A. Bezryadin, *Phys. Rev. B* **70**, 214506 (2004).
 - [4] M. Tinkham, J. U. Free, C. N. Lau and N. Markovic, *Phys. Rev. B.* **68**, 134515 (2002).
 - [5] M. Sahu, M. Bae, A. Rogachev, D. Pekker, T. Wei, N. Shah, P. M. Goldbart, A. Bezryadin, arXiv:0804.2251v2 (2008).
 - [6] N. Shah, D. Pekker, P. M. Goldbart, *Phys. Rev. Lett.* **101**, 207001 (2008).
 - [7] A. Rogachev, A. T. Bollinger, and A. Bezryadin, *Phys. Rev. Lett.* **94**, 017004 (2005).
 - [8] J.P Kauppinen and J.P Pekola, *Phys. Rev. Lett.* **77**, 3889 (1996).

-
- [9] A. T. Bollinger, A. Rogachev, A. Bezryadin, *Europhys. Lett.* **76** 3 505-511 (2006).
- [10] A. D. Zaikin, D. S. Golubev, A. van Otrerlo, G. T. Zimanyi, *Phys. Rev. Lett* (1997). 1552
- [11] S. Chakravarty, *Phys. Rev. Lett.* **49**, 681 (1982).
- [12] A. Schmidt, *Phys. Rev. Lett.* **51**, 1506 (1983).
- [13] S. A. Bulgadaev, *JETP Lett.* **39**, 315 (1984).
- [14] A. O. Caldeira and A. J. Leggett, *Phys. Rev. Lett.* **46**, 211(1981).
- [15] J. S. Penttilä *et al.*, *Phys. Rev. Lett.* **82**, 1004 (1999).
- [16] A.V. Herzog, P. Xiong, F. Sharifi, and R. C. Dynes, *Phys. Rev. Lett.* **76**, 668 (1996).
- [17] D. Meidan, Y. Oreg, and G. Refael, *Phys. Rev. Lett.* **98**, 187001(2007); G. Refael *et al.*, *Phys. Rev. B.* **68**, 214515 (2003) G. Refael, E. Demler, and Y. Oreg, arXiv:0803.2515.
- [18] Samples included were fabricated and studied by: Alexey Bezryadin, Anthony Bollinger, Matthew Brenner, Mitrabhanu Sahu, Andrey Rogachev and myself.
- [19] A. Rogachev *et. al.*, *Phys. Rev. Lett.* **97**, 137001 (2006).
- [20] J. M. Graybeal and M. R. Beasley, *Phys. Rev. B* **29**, 4167 (1984); J. M. Graybeal, Ph.D. thesis, Stanford University, (1985).
- [21] M. Tinkham, & C. N. Lau. *Appl. Phys. Lett.* **80**, 80, 2946-2948 (2002).
- [22] A. Bezryadin A, C.N. Lau, and M. Tinkham, *Nature* **404**, 971–974 (2000).
- [23] A. Bezryadin, *J. of Phys. Condens. Matter* **76**, 043202/1–19 (2008).
- [24] M. Remeika, and A. Bezryadin, *Nanotechnology*, **16** No 8 (2005).

Chapter 4

Microwave Response

This chapter will focus on the general microwave response in superconducting nanowires. When a microwave signal (MW) is applied to the wires and its power is increased we observe first a reduction in the critical switching current, I_{SW} , followed by the appearance of a dynamical superconducting state, i.e. a phase slip center (PSC), which is characterized by the appearance of Shapiro steps. It is an important fact since in our experiments on wires not subjected to a microwave radiation PSCs were not observed, but only the normal state, as the current exceeds the switching current. The behavior of the switching current of the wire and of the PSC were studied extensively and these results are the focus of this chapter. Integer and fractional Shapiro steps is the topic of the next chapter though it is mentioned here. The observed microwave-induced phase slip centers appear to be qualitatively different from the usual PSC described by the Skockpol, Beasley and Tinkham model [1].

4.1 Experimental Observations: The Critical Currents

The DC current-voltage characteristics of our nanowires show hysteretic behavior (Fig. 4.1a). As the bias current is swept from zero to higher values the wire switches to a resistive state, which is a normal state due to Joule heating. This switching current I_{SW} is stochastic, meaning that each time the $V(I)$ curve is measured one obtains a slightly different value for I_{SW} . Once in the normal state, the $V(I)$ curve is linear with the slope almost exactly equal to the normal resistance of the entire wire. As the bias current is decreased below the switching current, a retrapping event is observed at the retrapping current I_R . At this current the wire jumps back to the superconducting state. This

retrapping current is not stochastic, meaning that in every measurement the same value of I_R (with the precision of the setup) is observed. This deterministic nature indicates that the resistive state involved is simply a normal state, due to Joule heating of the wire [2,3,4]. In this case the retrapping is explained by cooling of the wire below T_C as the bias current is decreased [2]. Since the cooling process involves a macroscopic number of degrees of freedom, associated with normal electrons, the fluctuation of the I_R is not observed.

Increasing the temperature from 300 mK suppresses the switching current while the retrapping current remains constant up to $T \sim 2.5\text{K} < T_C$. At intermediate temperatures $2.5\text{K} < T < 3.1\text{K}$ both I_{SW} and I_R are suppressed with increasing temperature and there is a finite voltage due to thermally activated phase slips which appears as tails in the $V-I$ curves, before the switching occurs. This fact is important evidence indicating that phase slips do occur randomly in the wire even before it switches into JNS. In other words, multiple phase slips are required to switch the wire. Such multiple phase slip process is well described by the models developed by Shah et al. [3,4]. As the temperature increases from $T = 3.1\text{K}$ to $T = T_C = 4.1\text{K}$, the hysteresis disappears and the critical current goes to zero.

The microwave response of the wire shows some similarity to the temperature response but it is different enough to rule out the trivial heating of the nanowire with the microwave radiation (MR). Figure 4.1 compares the behavior of a wire due to increasing the temperature to that due to increasing the applied MW power. When the power of the MW signal is increased from zero, the first effect that is noticed is that the switching current of the wire decreases and the retrapping current remains the same. In that respect the effect of MW is like the effect of heating. At higher powers of applied MW an additional step occurs in the $V(I)$ curve (see Fig. 1b insert), either before the switching to the normal state as the current is increased (sweeping-up branch) or after the retrapping from the normal state as the current is decreased (sweeping-down branch). The occurrence of the step takes place at some critical power, P^* , in the sweeping-up branch, and at P^R in the sweeping-down branch of the $V(I)$ curve. We interpret this step as a microwave-assisted phase slip center (PSC). These observations are similar to the

observations of Anderson and Dayem on thin film constrictions [5], performed on quasi-two-dimensional superconducting bridges.

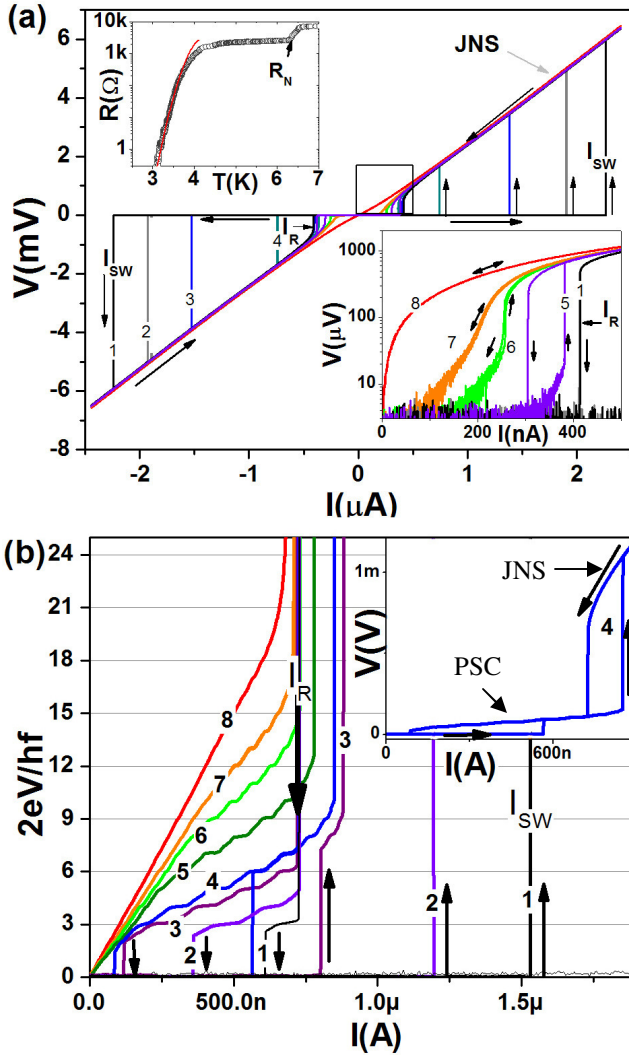


FIG. 4.1 (a) Current-Voltage characteristics for sample 121707C numbered according to increasing temperature: Curve (C) 1: $T = 358\text{mK}$; 2: $T = 1\text{K}$; 3: $T = 1.8\text{K}$; 4: $T = 2.5\text{K}$; 5: $T = 2.9\text{K}$; 6: $T = 3.1\text{K}$; 7: $T = 3.4\text{K}$ and 8: $T = 4.1\text{K}$, above T_C of the wire. The critical currents I_{SW} and I_R are indicated. Lower Inset: log scale of the boxed region with curves 2-4 removed for clarity. Upper Inset: R vs. T for the sample with fit to TAPS theory with parameters $R_N=2760\ \Omega$, $T_C=4.1\text{K}$, $L=110\text{nm}$, $\zeta(0)=10.2\text{nm}$. The resistance drop at 6.5K is due to the leads going superconducting, The normal resistance of the wire is taken to be the value measured after this transition as indicated (b) Positive bias $V(I)$ characteristics for sample A for frequency of MW $f = 7.34\text{GHz}$ and at $T = 350\text{mK}$. The voltage is normalized by the radiation photon energy, as indicated (here h -Planck's constant, e - the electron charge and f is the frequency). Shapiro steps are clearly observed

at integer values of the normalized voltage. The curves are numbered according to increasing microwave power, P , measured at the source in dBm; Curve (#: dBm) 1: -5.1; 2: -4.7; 3: -4.2; 4: -3.4; 5: -2.5; 6: -1.0; 7: 0.2; 8: 2.0. The trend with increasing power for this frequency is as follows: First I_{SW} is reduced and a PSC appears in the sweeping-down branch (1). Upon increasing the power I_{SW} is further reduced and a PSC appears in the sweeping-up branch (3). At higher powers still there is no longer a fully superconducting state (5) but the transition into and out of JNS is hysteretic. Further power increase causes the hysteresis to disappear (Curve 6) and eventually I_R becomes slightly suppressed. For curves 1-6 the retrapping current, I_R , is the same and it is shown by the thick, solid, downward arrow. Inset full scale positive bias $V(I)$ curve for curve 4 with arrows indicating the sweeping-up and sweeping down branches and showing that there are 4 distinct transitions for this power.

The effects of increasing MW power on the critical currents are better summarized in Fig. 4.2. As the microwave power is increased from 0 to P^* the switching current I_{SW} for $S \rightarrow$ JNS transition monotonically decreases while remaining stochastic and the $JNS \rightarrow S$ transition at I_R remains constant and deterministic. Figure 4.2a shows this trend by plotting 100 values for I_{SW} and I_R vs. MW power. The kink in the plot is indicative of the onset of a PSC branch in the sweeping-up branch, which occurs at the power P^* . For powers greater than P^* two jumps on the V-I curve are observed, corresponding to the two transitions: first $S \rightarrow$ PSC and the second $PSC \rightarrow$ JNS, as the current is increased. While the transition $S \rightarrow$ PSC remains highly stochastic (Fig. 4.2b), the transition $PSC \rightarrow$ JNS exhibits a very narrow, almost deterministic distribution (Fig. 4.2a). While below P^* there is only one jump on the V-I curve (denoted I_{SW}), there are two jumps at $P > P^*$. Thus, for $P > P^*$, we introduce two notations for the jumps: I_{SW}^{PSC} (this is the first jump, representing the transition $S \rightarrow$ PSC), and I_{SW} (this is the second jump representing the transition $PSC \rightarrow$ JNS). Thus in all case I_{SW} is the current at which the wire switches to the normal state. As the current is reduced we also observe either one or two retrapping events. The retrapping current for the transition from the normal branch to either the fully superconducting branch (S) or the PSC state is denoted as I_R . The retrapping current for the transition from the PSC branch to the fully superconducting branch (S) is denoted as I_R^{PSC} . The PSC is a dynamic superconducting state as evidenced by the appearance of Shapiro steps and the stochastic nature of both the switching current (I_{SW}^{PSC}) and retrapping current (I_R^{PSC}). Both of these phenomena are depicted in Fig. 4.2c. Unlike the $S \leftrightarrow$ JNS transition, the $S \leftrightarrow$ PSC transition is clearly stochastic in both directions. The transition $S \rightarrow$ PSC follows the same trend as the transition $S \rightarrow$ JNS at powers lower than P^* , in the sense that (a) the width of the distribution of I_{SW} for $P < P^*$ is very similar to the width of the distribution of I_{SW}^{PSC} at $P > P^*$, and (b) the slope of the curve I_{SW} vs. P for $P < P^*$ is very similar to the slope of the curve I_{SW}^{PSC} vs. P at $P > P^*$. This behavior will be discussed in greater detail in section 4.3. These observations strongly indicate that the same physics for the transition out of the superconducting state to the normal state and out of the superconducting state to the phase slip center is

involved. This is obvious, for example, due to the fact that the retrapping event $\text{PSC} \rightarrow \text{S}$ is clearly stochastic (Fig. 4.2c, insert, left distribution).

The Shapiro steps occur due to synchronization of the superconducting phase difference rotation with the applied high frequency MW radiation and will be discussed in detail in Chapter 5 of this manuscript. The steps appear at voltage values given by $2eV = n \cdot hf$, as expected. Shapiro steps are only present in the portion of the $V(I)$ curve attributed to the PSC. The lack of SS in the high voltage regime (JNS) independently verifies that it is a non-coherent (i.e. normal) regime. Among other things, this confirms the “hot spot model” previously developed by Tinkham et al. [2]

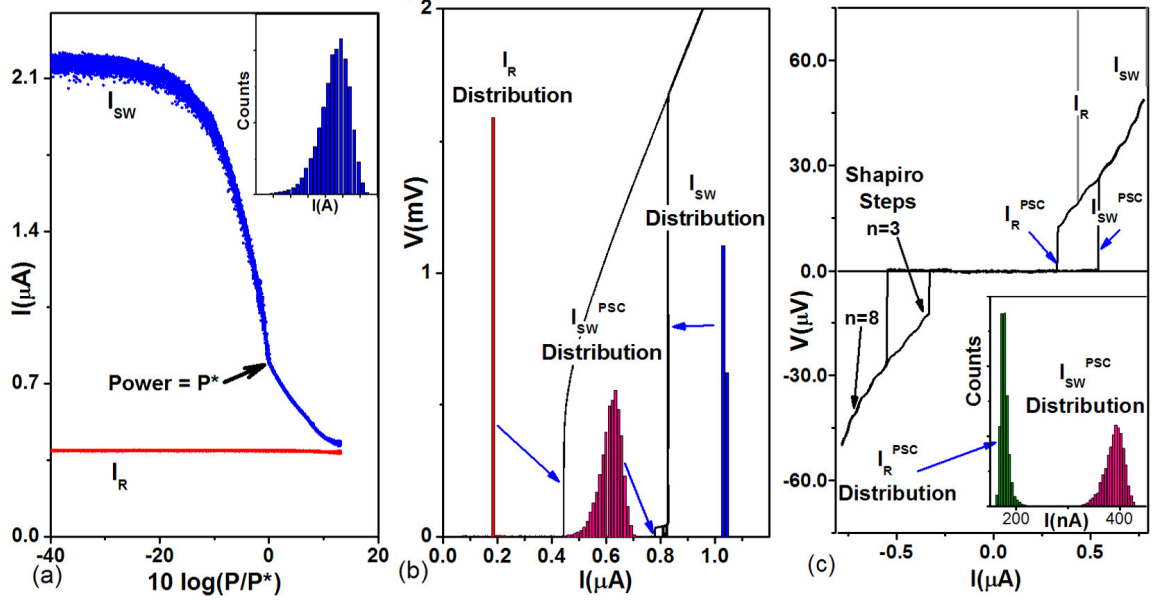


Figure 4.2 Switching and retrapping currents in different MW power regimes. (a) Switching current into the normal state, I_{SW} and retrapping from the normal state, I_R vs. applied MW power at 3 GHz for sample 121707C. 100 Points were taken at each power showing the spread due to the stochasticity of I_{SW} at low microwave powers. At all powers for I_R and at high powers of MW the spread in I_{SW} is smaller than the point size. The power P^* , indicated above, is defined as the power when a PSC first appears in the switching branch. P^* also corresponds to the kink in the curve. Inset A representative histogram for I_{SW} at power $P < P^*$. (b) Positive bias segment of a $V(I)$ curve for 10 traces for a power just above P^* . The histograms shown are for counts of a given I_R , I_{SW} and I_{SW}^{PSC} , indicated by the blue arrows for 10,000 total scans and are scaled to fit the figure. (c) $V(I)$ curve at $P > P^*$ and at a bias slightly below I_{SW} with normal state transitions drawn in to guide the eye. Shapiro steps are visible with steps corresponding to $V = n \cdot hf/2e$ with $n=3$ and $n=8$ indicated by arrows. Inset: distributions for the switching current, I_{SW}^{PSC} , and the retrapping current, I_R^{PSC} , for the PSC for 10,000 scans. Both critical currents for the PSC are stochastic. All data shown here were measured at a temperature of 500 mK.

4.2 Discussion and Analysis

In this section I will discuss the observations of a microwave assisted PSC in further detail. First I will compare our results with the hot spot model by Skockpol, Beasley and Tinkham [1] that I discussed in chapter 1. Then I will present a model for the transition from the PSC to the JNS that predicts a maximum supercurrent that depends on the power of MW applied. This model does not describe our nanowires, but

since we do not have an explanation for what we observe, it is still an interesting effect. In the next section I will discuss the stochastic switching currents we observe in the wires when exposed to microwave radiation.

4.2.1 Microwave Induced PSCs and the SBT Model

In previous studies PSC have been observed in wires near T_C even without microwave radiation [6]. The main difference is that our nanowires are extremely thin and remain quasi-one-dimensional (quasi-1D) down to zero temperature, while most of previous studies have been done on wires which are quasi-1D only close to T_C . Thus our type of wires open up a possibility of studying the dynamics of the quasi-1D condensate, including phase slip centers, down to low temperatures. In our type of nanowires, on the other hand, the heating prevented us from observing PSC without MW applied. One key difference is that long filaments are only one-dimensional (1D) near T_C where $\xi(T)$ diverges. For our wires $\xi(0)$ is on the order of 10nm. Our quasi-1-D wires are too narrow to support a normal vortex core even at zero temperature thus enabling us to study phase slip centers down to the lowest available temperature, much lower than T_C . In the SBT model [1] of phase slip centers the order parameter is suppressed in a small region of the wire that is on the order of 2ξ . The Bogoliubov quasiparticles then diffuse a distance Λ_Q , a length longer than ξ near T_c , away from the center of the PSC before relaxing back into the condensate. This model predicts the voltage of the PSC to be given by: $V=2 \Lambda_Q \cdot \rho(I - \beta I_S)/A$ with I , the DC bias current, I_S , the supercurrent outside the PSC region, which is equal to the bias current, A the cross sectional area of the wire, and β , a constant on the order of $1/2$ such that βI_S is the offset current, which is the average supercurrent in the PSC. This model predicts the differential resistance of the PSC to be given by $R_{PSC}=2 \Lambda_Q \cdot \rho/A$ or equivalently $R_{PSC}/R_N = 2 \Lambda_Q/L$ with R_N and L being the normal state resistance and length of the wire. The dynamic resistance we measure in MW-assisted PSC depends strongly on the MW frequency and ranges from nearly 0 Ohms to 1000 Ohms at radiation powers slightly above P^* . Figure 4.3 is a plot of R_{PSC}/R_N vs f for 6 different samples. Note that according to the SBT model, if applied to our observations, the ratio R_{PSC}/R_N should be equal to the length of the core of the PSC divided by the total length of the wire.

But, of course, the observed very low values of this ratio, suggesting that the core is smaller than the coherence length in some cases, are probably unphysical because the SBT model was not derived for the case when a microwave signal is applied. We use this model here because (a) no theory for microwave-induced PSC does exist at present and (b) to emphasize the qualitatively different physics observed on microwave-induced PSC compared to regular PSC. The average resistance of the phase slip center was taken from available data by a linear fit of the $V(I)$ curve for powers near P^* . The data show a monotonic dependence of the average differential resistance of the PSC on MW frequency. Since the voltage steps are linearly proportional to frequency it is possible that the dynamic resistance of the PSC branch is masked by the presence of the Shapiro steps, however this slope still has physical significance. Also PSCs appear at low frequencies, ~ 100 MHz without observable Shapiro Steps and with a slope on the order of 10 ohms. Figure 4.3 shows measurements of R_{PSC}/R_N and the normalized offset current, I_{Offset}/I_{SW} , for sample MS3 as a function of applied MW power at 3 different frequencies. It is interesting to note that the resistance of the PSC measured in this manner decreases slightly for increasing power and then has a discontinuous jump after which it increases with the applied MW power. The offset current decreases steadily to zero as the MW power is increased.

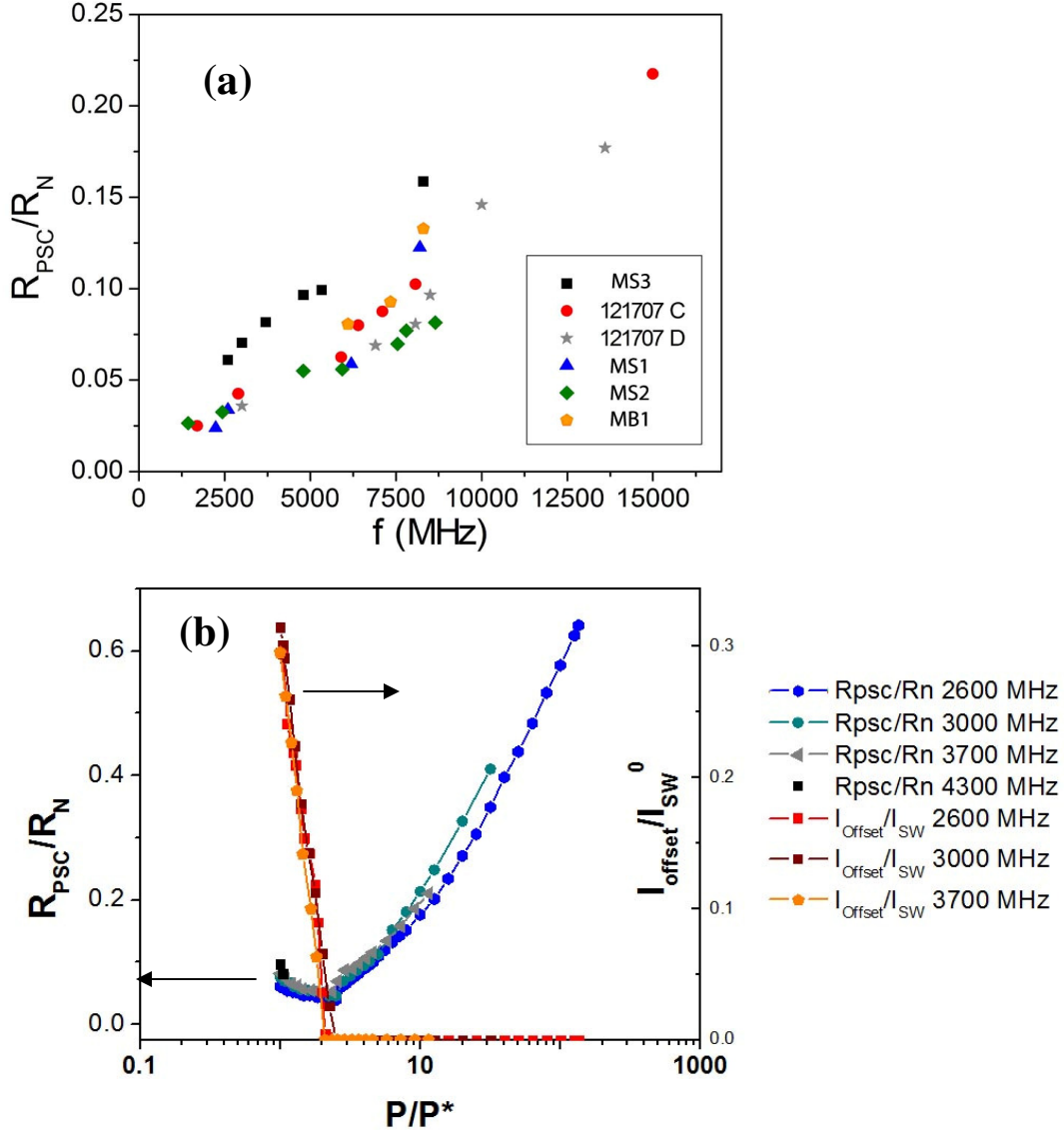


Figure 4.3 (a): Average normalized resistance, or equivalently relative length of the MW-assisted PSC with respect to the resistance of the NHS, R_N , for 6 samples taken at $T \sim 300\text{mK}$ and MW power slightly greater than P^* . The data show that the average resistance of the MW-assisted PSC monotonically increases with the frequency of applied MW. **(b)** R_{PSC}/R_N and I_{offset}/I_{SW} vs. P/P^* for 3 frequencies for the sample MS3. Resistance is taken as a linear fit of the first few steps in the $V(I)$ characteristic. The kink in R_{PSC} occurs near where the offset current goes to zero. This might be when $P_{RF}^{1/2} \sim I_S$ max of the PSC because the “higher” resistance behavior shows up in the numerical calculations as well.

It has recently been shown that phase slips at high bias currents generate enough heat to drive a nanowire into the normal state (i.e. into JNS) [3,4]. We propose here an addition to that model, namely that, if microwave radiation is present, there is an

intermediate, dynamic superconducting state, i.e. a PSC, that the wire switches into first and then switches normal because the heat generated in the PSC is enough to heat the whole wire above T_C . It is important to recall that our nanowires are suspended structures typically measured in vacuum and therefore can only conduct heat along their length to the electrode bath. In the presence of microwave radiation we are able to separate these two transitions and study their qualitatively different physics. Depending on the frequency of MW and the sample, the PSC branch appears in the $V(I)$ characteristics at some critical power in either the current-sweeping-up branch or the current-sweeping-down branch first and then in both branches at higher powers. The reason for this is not fully understood but may be due to a combination of three factors. If we assume that a PSC branch always exists, but is hidden due to overheating then the location and slope of this branch will determine whether it appears first in the current-sweeping-up or current-sweeping-down branch. If the wire were to switch into a PSC at high bias current it would immediately switch normal due to overheating. If this happens we do not observe a PSC branch. In addition to that the apparent frequency dependant slope of the PSC branch and its offset current determines where the PSC branch intersects with the overheating-controlled hysteresis curve. The offset current for the PSC decreases with increasing microwave power so a low resistance PSC will appear first in the current-sweeping-up branch at P^* and then in the current-sweeping-down branch when the offset current, which decreases with applied power, is decreased below I_R . At higher frequencies the average slope of the PSC branch becomes higher and for powers below P^* the intersection of the PSC branch with the overheating transition occurs at a very high voltage and the power dissipated in the wire, IV , in addition to the heat generated by phase slips is high enough to heat the wire above T_C . Thus, for this case, when the wire switches into the PSC branch it immediately goes normal because the wire can not dissipate the heat generated by the bias current. In this case the PSC appears in the retrapping branch at P^R which is the power at which the offset current is sufficiently below I_R so that the PSC branch is stable. A PSC that appears first in the current-sweeping-down branch will appear in the current-sweeping-up branch at a slightly higher power. At higher power the switching current, I_{SW} , is further reduced and it intersects the PSC branch at a lower voltage. This voltage is low enough that the joule heating due to

the bias current and phase slips is not sufficient to heat the wire above T_C . At powers in this regime a stable dynamic superconducting state exists and the system stays in the PSC branch until the current is increased to I_{SW} .

4.2.2 Transition into the Normal State

The transition into the normal state at I_{SW} is not very stochastic when a PSC is present and therefore its dynamics are different from those of the transition into the PSC. This transition, from PSC \rightarrow JNS is similar to the switching transition at higher temperatures in the absence of microwaves. There are 2 similarities between the high temperature S \rightarrow JNS and the low temperature, High MW power PSC \rightarrow JNS transition. The first is that they occur at currents much lower than the base temperature switching current. This factor is not significant on its own because the switching current for the transition S \rightarrow PSC is even lower than that for the transition PSC \rightarrow JNS and it has a very broad distribution. The second similarity is that each of these transitions show very strong phase diffusion in the form of finite increasing voltage tails before the switching transition. This can be seen and compared in curves 5 and 6 in figure 1a and curves 6 and 7 in figure 1b. It has been shown [7] that phase diffusion can be enhanced by microwave radiation in superconductor-insulator-superconductor junctions having $E_J \gg E_C$. For our wires $E_J = \hbar I_{C0} / 2e$, using the maximum switching current as an estimate for the depairing current, I_{C0} , is about 1/2 meV, whereas the charging energy, E_C , given by $e^2 / (2C)$, using $C = l f F$, is about 10 μ eV [8]. Thus our system is in the regime where this model predicts that microwaves cause the enhancement of phase diffusion. The authors predict that the maximum supercurrent that a Josephson junction can carry when microwaves are present at high powers scales as $P^{-1/4}$.

To test if this model is applicable to our system we analyzed data for various observed switching transitions in several wires. Figure 4.4(a) shows transition currents plotted vs. applied MW power for sample 121707C taken at 2900MHz. The higher power region for I_{SW} before it merges with the I_R was fit to determine its power dependence at several frequencies to determine the exponent α in the relation: $I_{SW} \sim P^{-\alpha}$.

Figure 4.5 shows data for switching current vs. power for sample 121707C this data was also fit using the above relationship. The results of these fits are summarized in Table 4.1 for 3 samples measured at different frequencies. The fits did not show any general trend and give α values that are not far from the predicted value $\alpha=0.25$. Although the experimental values of α varied significantly from sample to sample and from one frequency to another, this variations might be within the range of uncertainties and the noise of the experiment. We suggest this especially because no clear trend of the values of α was observed. Figure 4.4(b) shows the DC power at each transition for 2 samples. The dissipated Joule power, IV , in the wire, when it switches, actually increases with applied MW power. The current at which switching occurs decreases, but switching occurs at a higher voltage. The cause for this behavior is unknown.

The frequency behavior of the switching transition was also studied. Figure 4.5 summarizes the results of this study on sample 121707C. The data were taken by varying the microwave power and measuring the switching current 100 times at each power. The curve taken at 3GHz is the same one that appears in Fig. 4.2(a). The powers are all normalized to P^* for comparison. The curves show the same trend at different frequencies however their shapes are different and the current at which the PSC appears (i.e. the power P^*) shows some frequency dependence. This frequency dependence is shown in Fig. 4.5(b). When plotted on a log-log scale the frequency dependence looks very regular and we hoped to see if this could tell us anything about the wire. When the frequency dependence of the switching current is extrapolated to the “DC” case (measured at 11Hz) it gives a current of 4.5 μA which is much higher than the DC switching current of 2.4 μA . Although the switching current is lower than the fluctuation free critical current, I_{C0} , this value is too high to be the actual depairing current. Therefore this type of analysis does not seem to give us a means to determine I_{C0} . The cause for frequency dependence on the switching current is not known.

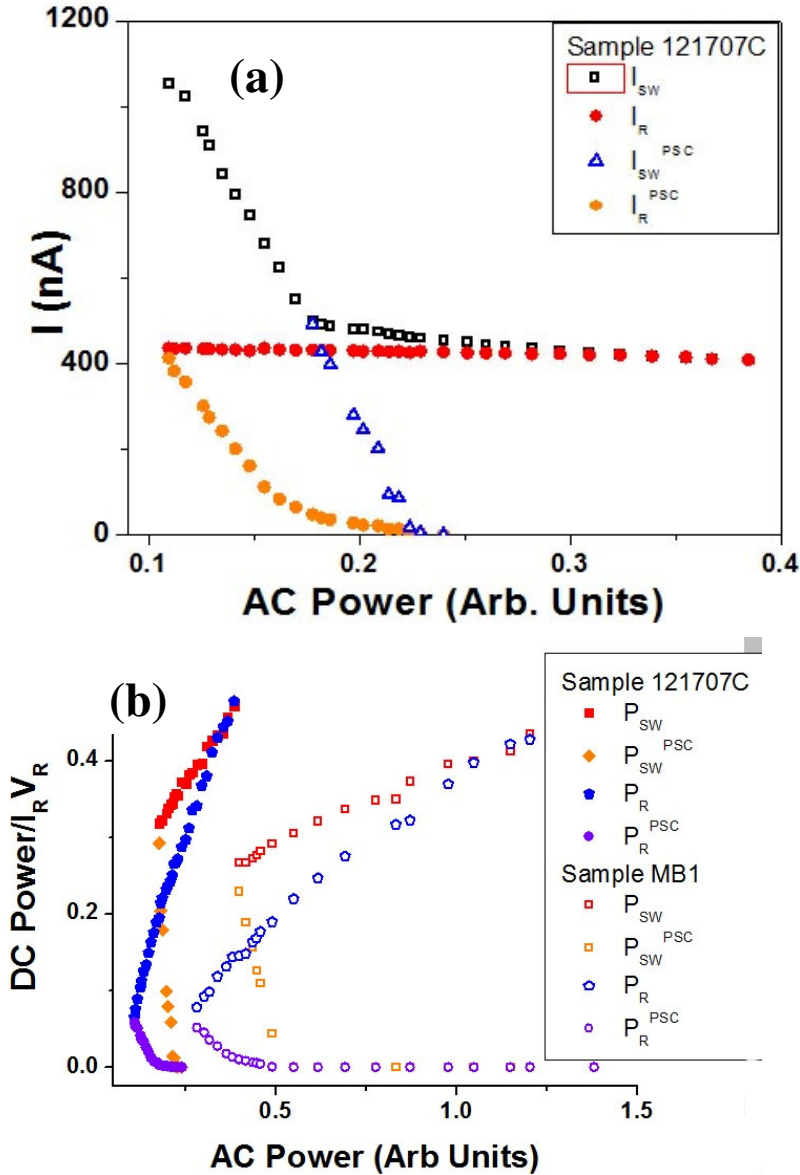


Figure 4.4 (a) Various transition currents in samples 121707 at 2900 MHz plotted vs. applied MW power. Note how I_{SW}^{PSC} follows the same trend as I_{SW} once there are 2 switching currents. This indicates that the same physical mechanism must underly the transition $S \rightarrow JNS$ and $S \rightarrow PSC$. **(b)** DC power at each transition, $I \cdot V$, normalized to the retrapping power, $I_R V_R$ which is constant for low RF powers. Each power is measured in the PSC branch. I.e. it is the voltage of the PSC branch * I at the transition. The data for sample 12170C was taken with MW at 2900 MHz and the data for sample MB1 was taken at 7300 MHz. The switching (retrapping) power for the PSC tends to zero because the switching (retrapping) current does.

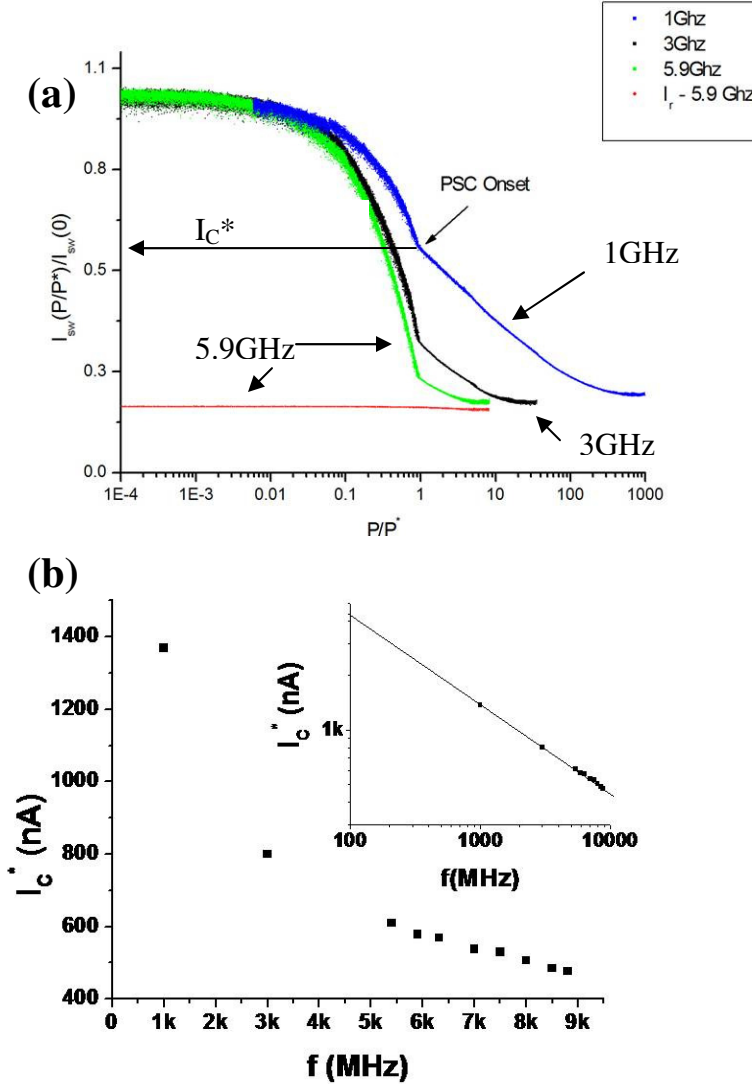


Figure 4.5 Switching current behavior for different frequencies for sample 121707C. (a) I_{SW} vs. applied microwave power for 3 frequencies as indicated. I_C^* is indicated for the curve taken at 1 GHz. The retrapping current I_R is shown for 5.9 GHz and shows the same behavior for other frequencies. The straight portion of the curve for powers greater than P^* are fit to determine the power dependence $I_{SW} \sim P^{-\alpha}$. (b) I_C^* plotted vs. the frequency it was measured at. Inset log-log plot of same data. The intercept of the line is $4.5 \mu\text{A}$, which is $2 \mu\text{A}$ higher than the “DC” (11 Hz) value for the switching current. The slope of a linear fit was -0.479 .

Sample	Exponent alpha in $I_{SW} \sim P^{-\alpha}$	MW Frequency (MHz)
121707 C	0.2462	5900
121707 C	0.2217	8500
121707 C	0.21	8800
121707 C	0.25	5400
121707 C	0.19	1000
MS3	0.17	3000
MB1	0.24	7300

Table 4.1 Summary of fits of switching current I_{sw} vs. power. The straight portions of I_{SW} vs P curves as shown in Fig 4.5 are fit. (It would be good to show one of such fits on the graph.) The results are close to the predictions of the Koval-Fistul-Ustinov model [7].

4.3 Phase Slips and Switching in Superconducting Nanowires

In this section I will discuss the stochastic nature of switching currents I_{SW} and I_{SW}^{PSC} in our nanowires when they are exposed to MW radiation. The switching process is caused by the occurrence of phase slips in the wire at high bias currents or by Joule heating, which brings the wire to the normal state. First I will review the recent results by a fellow member of my group as they are key to understanding the physics of the switching current in our wires. Next I will present observations for the behavior of the Switching Current Distribution (SCD) when exposed to microwave radiation. Finally I will present a model to explain this behavior. This section is the central result of this chapter.

4.3.1 Switching Current Distributions Without Microwave Radiation and Quantum Phase Slips

Before discussing the behavior of the switching transition in a wire exposed to microwave radiation, I will first review the recent results on this process in the purely dc case [3, 4]. The authors study the stochastic nature of the switching current at different temperatures to understand the underlying mechanism that leads to the transition from the superconducting state to the JNS. What they found was that the distribution of switching currents became broader as the temperature was lowered and that this rather counter-intuitive trend is due to the decrease, with decreasing temperature, of the number of phase slips required to heat the wire to the normal state. Also, they were able to show the presence of QPS in our wires by studying their behavior at low temperatures and at high bias currents.

Figure 4.6 shows the trend they observe in the SCD at temperatures between 2.3K and 300mK as well as the behavior of the standard deviation of the SCD. They observe a general broadening of the SCD as the temperature is lowered with a corresponding rise in the standard deviation. The theoretical reason for this behavior is explained here [4]. In this model, developed in the Goldbart group, the thermal conductivity of the superconducting nanowire system is taken into account and the conditions for overheating the wire above its current-dependent critical temperature are found theoretically. The wire is a suspended structure and it is located in a vacuum chamber during the measurements. As such any heat dissipated in the wire in the form of phonons must be conducted to the leads where it can dissipate further. Heat is generated when a phase slip occurs. When this happens a small region of the wire becomes normal and thus will dissipate more heat due to the well known Joule heating effect. For the case of a nanowire it can be shown that the wire is heated by a “quantum” of energy, $I h/2e$, for each phase slip [4]. Here I is the bias current so it can be seen that the higher the current the more heat it will dump into the wire by each phase slip. Using this relationship and a numerical model for the thermal conductivity they were able to show that at temperatures

lower than ~ 500 mK a single phase slip event is enough to overheat a small segment of the wire and to trigger to wire to switch from the superconducting state to the JNS.

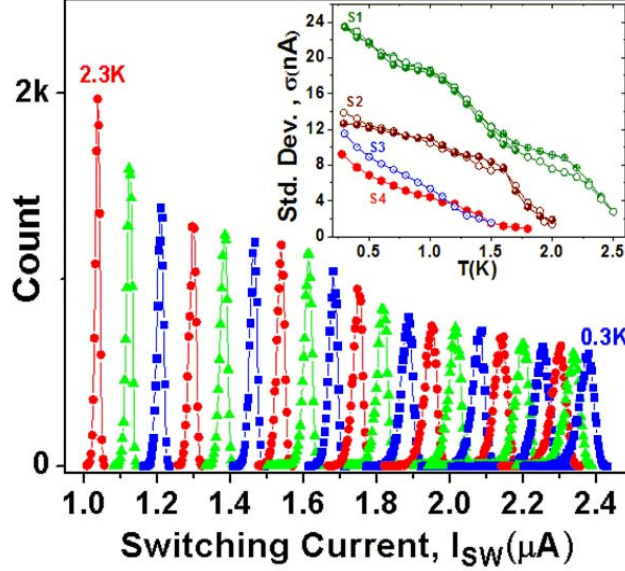


Figure 4.6 Switching Current Distribution (SCD) at different temperatures from [3]. The main plot shows SCD for temperatures between 0.3 K (right most) and 2.3 K (left most) with $\Delta T = 0.1$ K for sample S1. The SCD broadens as the temperature is decreased. This broadening results in an increasing standard deviation. Inset: Standard deviation of the SCD for the 4 samples included in the study. The standard deviation increases dramatically as the temperature is lowered.

To determine whether this single phase slip is due to thermal or quantum fluctuations further analysis was needed. The SCD can be converted into a switching rate using formulas used by Fulton and Dunkleberger (FD) [9]:

$$\Gamma(K) = \frac{dI}{dt} \frac{1}{\Delta I} \ln \left(\frac{\sum_{j=1}^K P(j)}{\sum_{i=1}^{K-1} P(i)} \right) \quad (4.1)$$

To use this relationship the SCD is converted into a histogram with bin width, ΔI , and channel with the the largest value of the current is indexed, K . The measured rates are then compared to the rates for the two types of phase slip processes (i.e. thermal activation and quantum tunneling):

$$\begin{aligned}
\Gamma_{\text{TAPS}} &= \Omega_{\text{TAPS}} \exp\left(-\frac{\Delta F(T, I)}{k_B T}\right) \\
&= \left(\frac{L}{\xi(T)}\right) \left(\frac{1}{\tau_{\text{GL}}}\right) \left(\frac{\Delta F(T)}{k_B T}\right)^{1/2} \exp\left(-\frac{\Delta F(T, I)}{k_B T}\right) \quad (4.2a)
\end{aligned}$$

$$\begin{aligned}
\Gamma_{\text{QPS}} &= \Omega_{\text{QPS}} \exp\left(-\frac{\Delta F(T, I)}{k_B T_{\text{QPS}}}\right) \\
&= \left(\frac{L}{\xi(T)}\right) \left(\frac{1}{\tau_{\text{GL}}}\right) \left(\frac{\Delta F(T)}{k_B T_{\text{QPS}}}\right)^{1/2} \exp\left(-\frac{\Delta F(T, I)}{k_B T_{\text{QPS}}}\right) \quad (4.2b)
\end{aligned}$$

The expression 4.1 b represents the phenomenological Giordano model of quantum phase slips [10]. Here $\tau_{\text{GL}} = [\pi\hbar / 8k_B(T_C - T)]$ the Ginzburg-Landau relaxation time, Ω , the attempt rate, T_{QPS} , the temperature dependent effective temperature for a quantum phase slip from the Giordano model [10] with the free energy barrier given by [11]:

$$\Delta F(T, I) = \frac{\sqrt{6}\hbar I_C(T)}{2e} \left(1 - \frac{I}{I_C}\right)^{5/4} \quad (4.3)$$

Figure 4.7 shows the results of fitting rates obtained from SCD to the overheating model for the case of only TAPS (Fig. 4.7a) and for both TAPS and QPS (Fig. 4.7 b). The results show that the overheating model predicts a single QPS event as the cause for the wire to switch at very low temperatures.

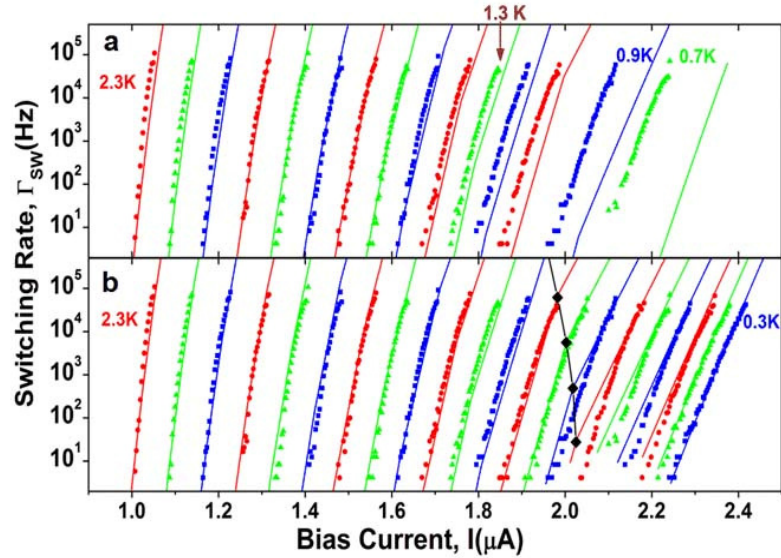


Figure 4.7 Switching Rates vs. Temperature from [3]. (a) Shows fits to the overheating model rates from equation (4.2a). Note how poorly the fits are for temperatures lower than 1.3K. (b) Fits to the overheating model using both QPS and TAPS, with a crossover to all QPS at the lowest temperatures. The model shows a single QPS can be used to fit the data at low temperatures. The black diamonds and connecting lines represent the boundary between switching due to a single QPS (to the right) and multiple QPS events (to the left).

Before I finish this subsection I would like to discuss the temperature dependent behavior of sample 091808B which is the sample that was studied the most thoroughly with MW and its SCD were measured. Figure 4.8 shows SCDs and rates for this sample for temperatures between 300mK and 2K. According to the overheating model this wire is in the single QPS regime for all temperatures below 1.2K.

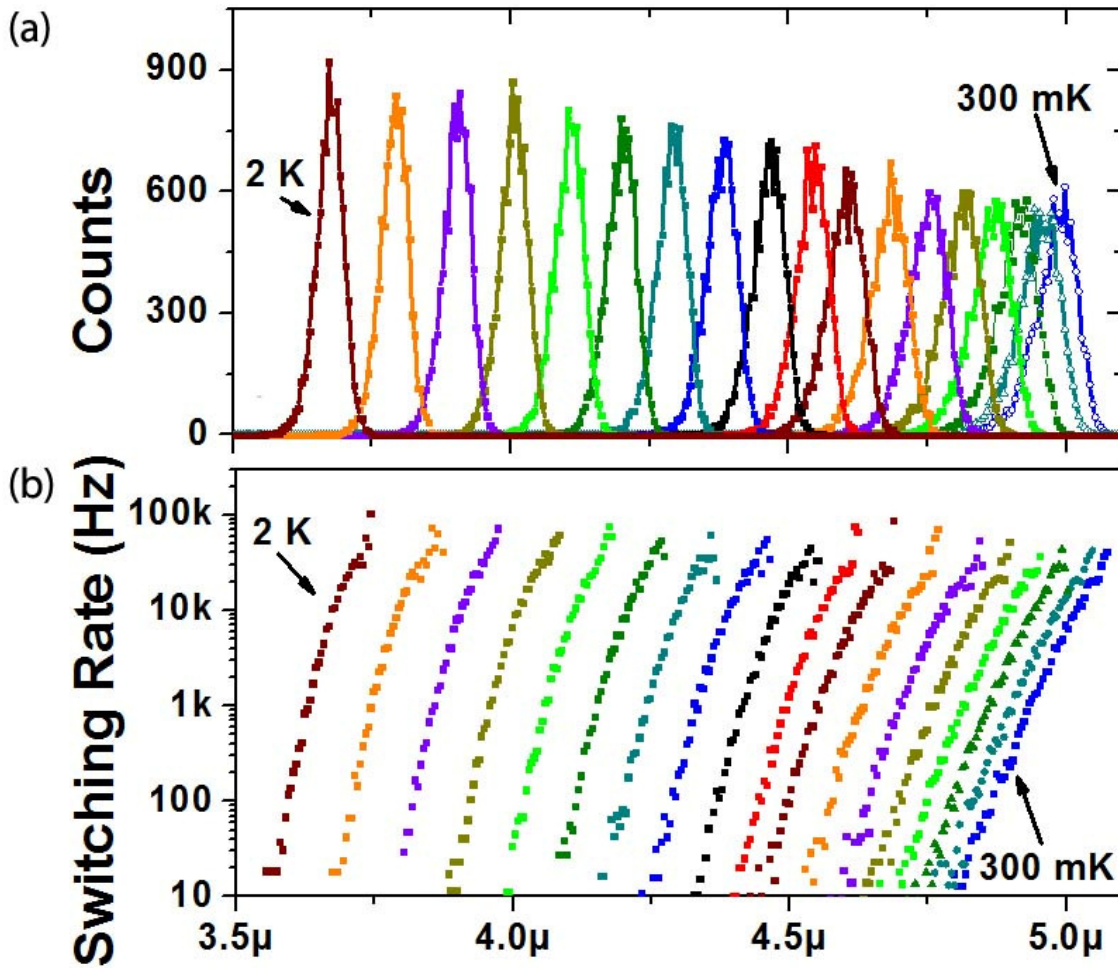


Figure 4.8 Switching Current vs. Temperature for sample 091808B. (a) SCD for temperatures 0.3K to 2.0 K in 0.1K steps. For each SCD 10K points was taken. (b) Rates for the distributions in (a). This data was analyzed by M. Sahu using the overheating model. The single QPS regime was determined to be for all T below 1K with a constant T_{QPS} value of 1.2K.

4.3.2 The Effect of Microwaves on the Switching Current Distribution

I have already discussed how MWs can lead to the suppression of the switching current, but now I will discuss how they affect the SCD. Figure 4.9 shows SCDs and rates for sample MS3 for increasing applied MW power from -44 dBm to -17 dBm. The data for this particular sample were not very good because they were measured using a higher sweep frequency (50 Hz vs. the usual 11 Hz) that may not have been optimal or because the source, which was later repaired, was starting to develop problems. One of these issues may have caused the SCDs to be a little inconsistent in their overall shape. One example of this is that the SCD for the lowest power studied, -44 dBm, exhibits what appears to be two peaks. Measurement issues aside, the data were good enough to perform some preliminary analysis.

According to the analysis performed by M. Sahu using the overheating model this wire is in the single QPS regime at 400mK, thus a single quantum phase slip is enough to cause the wire to switch from a superconducting state to the JNS state. In this case the rate of QPS is the same as the switching rate and we can use equation 4.2b, however we need to incorporate the MW radiation into this model. When we expose the wire to MW radiation we introduce an AC bias to the wire in addition to the DC bias we apply using our 4-probe setup. In this case we can compute the free energy barrier for a phase slip to oscillate following the equation:

$$\Delta F(T, I) = \frac{\sqrt{6}\hbar I_C(T)}{2e} \left(1 - \frac{I_{DC} + I_{RF} \sin \omega t}{I_C} \right)^{5/4} \quad (4.4)$$

Here I_{DC} is the dc bias current and I_{RF} is the ac bias current having angular frequency, ω , induced in the wire from the MW antenna and t is the time.

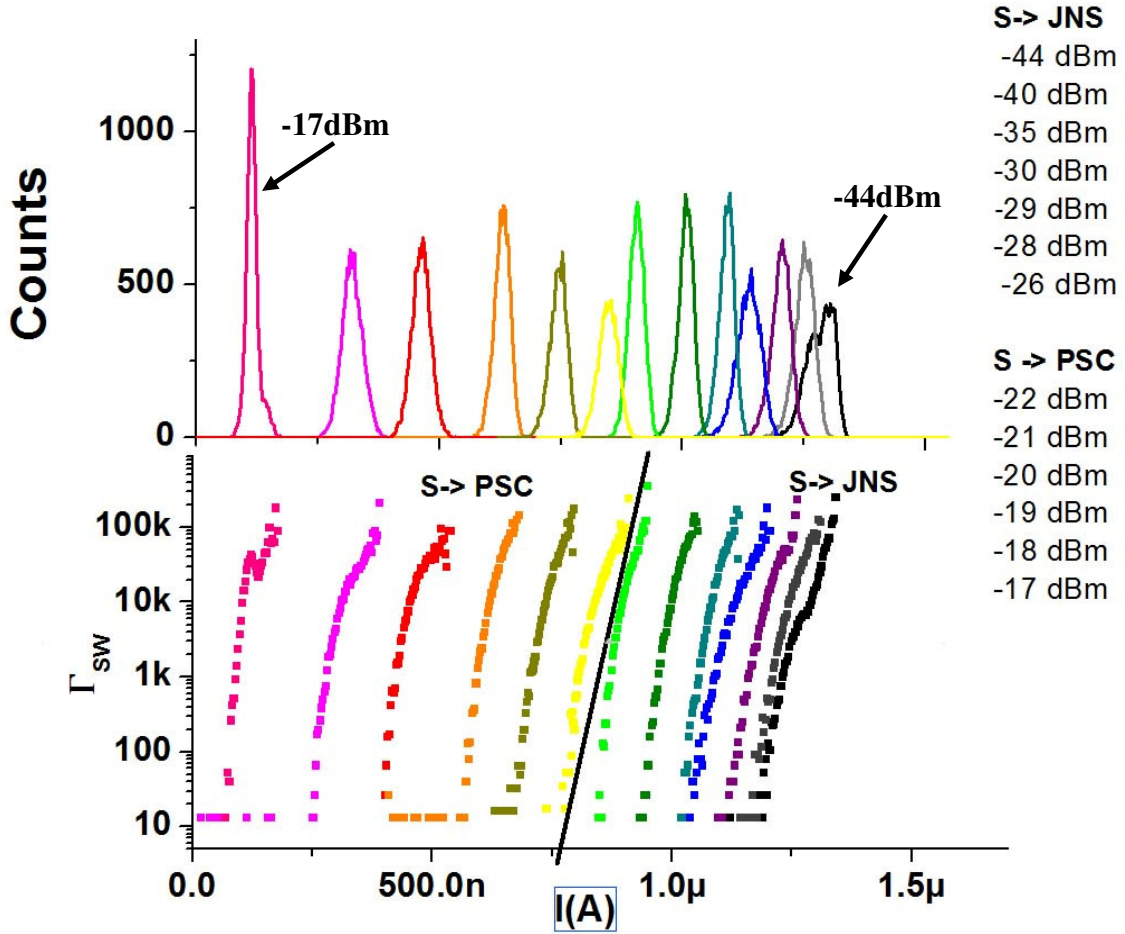


Figure 4.9 Switching current distributions and switching rates for sample MS3 at different MW powers taken at $T=400\text{mK}$. Top: SCD for the powers shown in the legend. The SCD is shifted to the left for higher powers. Bottom: switching rates for the above distributions. The line denotes the division between the transitions from superconducting state to JNS to the transition into the PSC. Note that there is no distinguishing characteristic between the two types of transitions indicating that a PSC state may always be the intermediate state. Also this data was taken using a 50Hz sweep to measure the $V(I)$ curve. This does not give as good results as data taken at the usual 11Hz.

By using equations 4.2b and 4.4 we can compute the switching rate for a single QPS event. To do this we must first average over one period of the microwave signal to get the time averaged switching rate. The approach is based on the assumption that the frequency of the microwave signal is still much lower than the attempt frequency of phase slips; thus simple averaging over one period of the microwave signal is appropriate.

Using this strategy we can compute the switching rate as a function of temperature, dc bias current, $I_C(T)$, ζ , T_C , T_{QPS} and the ac bias current amplitude I_{RF} and use this computed curve to fit the experimental data. The parameters ζ and T_C are taken to be the values obtained using TAPS fits and T_{QPS} and $I_C(T)$ are determined by the overheating model for temperature dependence data presented in Fig. 4.8. The parameters used for the case of MW may be changed slightly from those values however they remain fixed for all rates at different MW powers, so the only thing that will be changed to fit the rate data corresponding to various power values of microwave is I_{RF} . SCDs are measured for one wire at a constant temperature at several MW powers. The rates are then computed using the FD formula and they are fit using this model by varying I_{RF} . The real value of I_{RF} is not known however it must be proportional to the square root of the applied MW power. This applied ac bias current, I_{MW} , in arbitrary units, is computed from the applied MW power as $I_{MW} = (10^{P/10})^{1/2}$ where P is the power in dBm. If the fits done with this model on a set of data produce I_{RF} values that are proportional to I_{MW} then the model is consistent with out experiment. It is important to note that this simple model is not expected to work for values of I_{RF} that approach the critical current. Figure 4.10 shows the results of applying the fitting procedure to the low power rate data for the data shown in Fig 4.9.

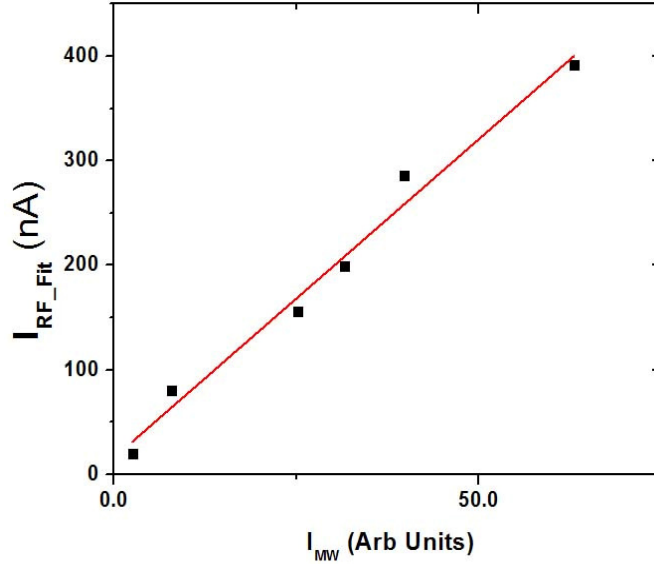


Figure 4.10 Fitting parameter, I_{RF} vs. applied MW current for sample MS3. The rate data are those between -40dBm and -26dBm shown in Fig 4.9. For these fits $I_C(T)$ was $1.6 \mu\text{A}$ and the fits started to fail to fit the data for $IRF \sim 600 \text{ nA}$. The rates for higher power are for the PSC regime which may have a different switching behavior.

The behavior of the standard deviation, σ , of the SCD for the transition $S \rightarrow JNS$ for $P < P^*$ and $S \rightarrow PSC$ for $P > P^*$ was studied for this sample. Figure 4.11 shows σ for the transitions as a function of applied MW power. From this graph we see that σ for the $S \rightarrow JNS$ (for $P < P^*$) transition is similar to its value for the $S \rightarrow PSC$ transition. This leads us to conclude that the transition out of the superconducting state is governed by the same process for each type of transition. The most plausible explanation is that in both cases just one phase slip is needed to switch from the superconducting state. On the contrary, for the transition $PSC \rightarrow JNS$ the σ value is much lower than in the other two transitions. Thus a different physics governs the $PSC \rightarrow JNS$ transition.

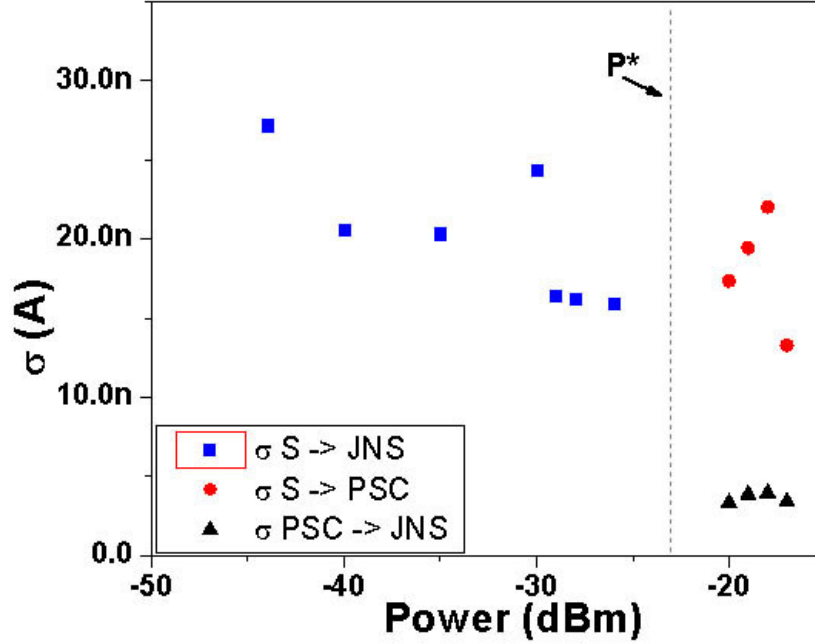


Figure 4.11 Standard deviation of SCD vs. applied MW power for sample MS3. P^* is denoted by the dashed line. We observe that σ for the transition $S \rightarrow JNS$ for $P < P^*$ is similar to σ for the transition $S \rightarrow PSC$ for $P > P^*$. For the transition $PSC \rightarrow JNS$ σ is about 4 nA, i.e it is much lower compared to the other two transitions.

Measurements like those detailed above were performed more rigorously on sample 091608B. Figure 4.12 shows SCD and the computed rates for this sample taken with a 5Hz sweep rate and 10,000 points for each distribution. The rates are fit to the single QPS model using the procedure outlined above. The results of the fitting procedure for the values of I_{RF} are plotted vs. the applied microwave current, I_{MW} in Fig 4.13. The linear fit in Fig. 4.13 is rather good which indicates that the single QPS model is consistent with our experimental measurements. The effects of applying MW and increasing the temperature are compared in Fig. 4.14. The two effects are very similar, however only MW leads to the formation of a PSC which leads us to

We are able to show that microwaves can enhance the rate of quantum phase slips. By applying a single quantum phase slip model we are able to show that our experimental results follow the same trend as our numerical model. Thus applying MW to superconducting nanowires provides a mechanism for studying the phase slip process by

lowering the free energy barrier. The similarity between the effects that temperature and MW have on our wires is because they both lower the free energy barrier in similar ways. The temperature enters into the free energy barrier through the critical current,

$$I_c(T) = I_c(0) \left[1 - (T/T_c)^2 \right]^{3/2} \quad [12].$$

Microwaves enter into the barrier as show in equation 4.3 however they can also synchronize with the phase slip process. This synchronization is the topic of the next chapter, but it must also play a role in the formation of the PSC. The physics behind the formation of the PSC is not yet understood, but we do understand how the barrier is suppressed and in the next chapter I will discuss the behavior of the PSC branch and lock-in process of the PSC and the microwave, which leads to the occurrence of integer and fractional Shapiro steps.

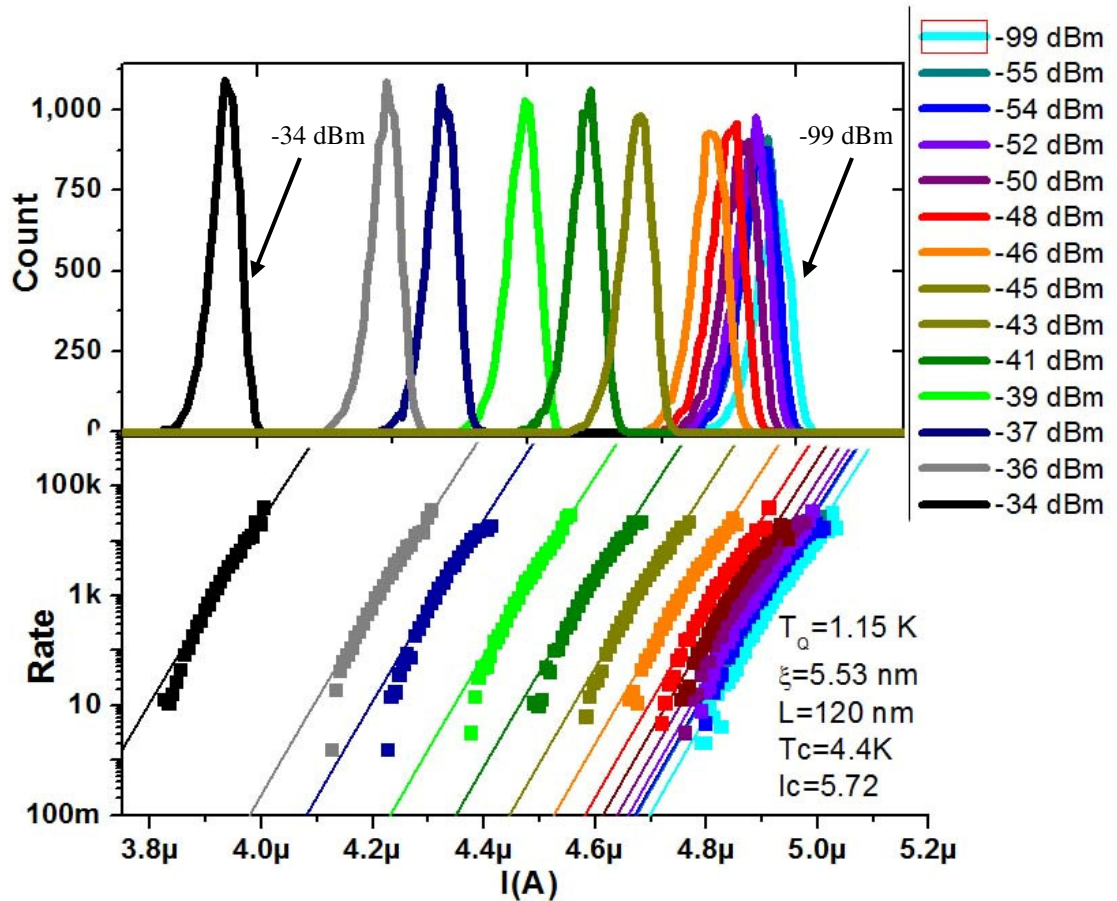


Figure 4.12 Switching current distribution and rates at different MW powers taken at $T = 300$ mK. Top: 10,000 point SCDs taken at the MW powers given in the legend. Bottom: Rates for the SCDs in the top graph along with fits to the single QPS model. The fitting parameters are shown in the lower legend and are close to the values used in the overheating model. The values for I_{RF} were changed to fit each curve and these will be shown in Fig 4.12. The fits (solid straight lines) are obtained from the Giordano model of QPS (eq 4.2b) by averaging of the rate over one microwave period, using eq.4.4.

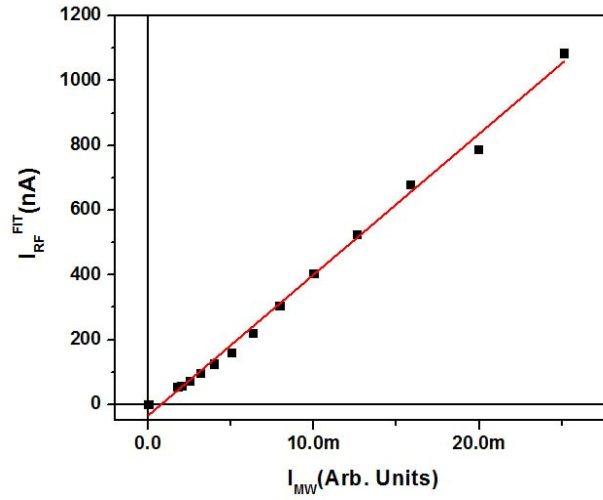


Figure 4.13 Fitting parameters, I_{RF}^{Fit} , vs. applied MW current for sample 091608B. The other parameters used are those given in Fig. 4.11. The linear fit shows that our fitting parameters are consistent with the values of applied MW power used in our experiment.

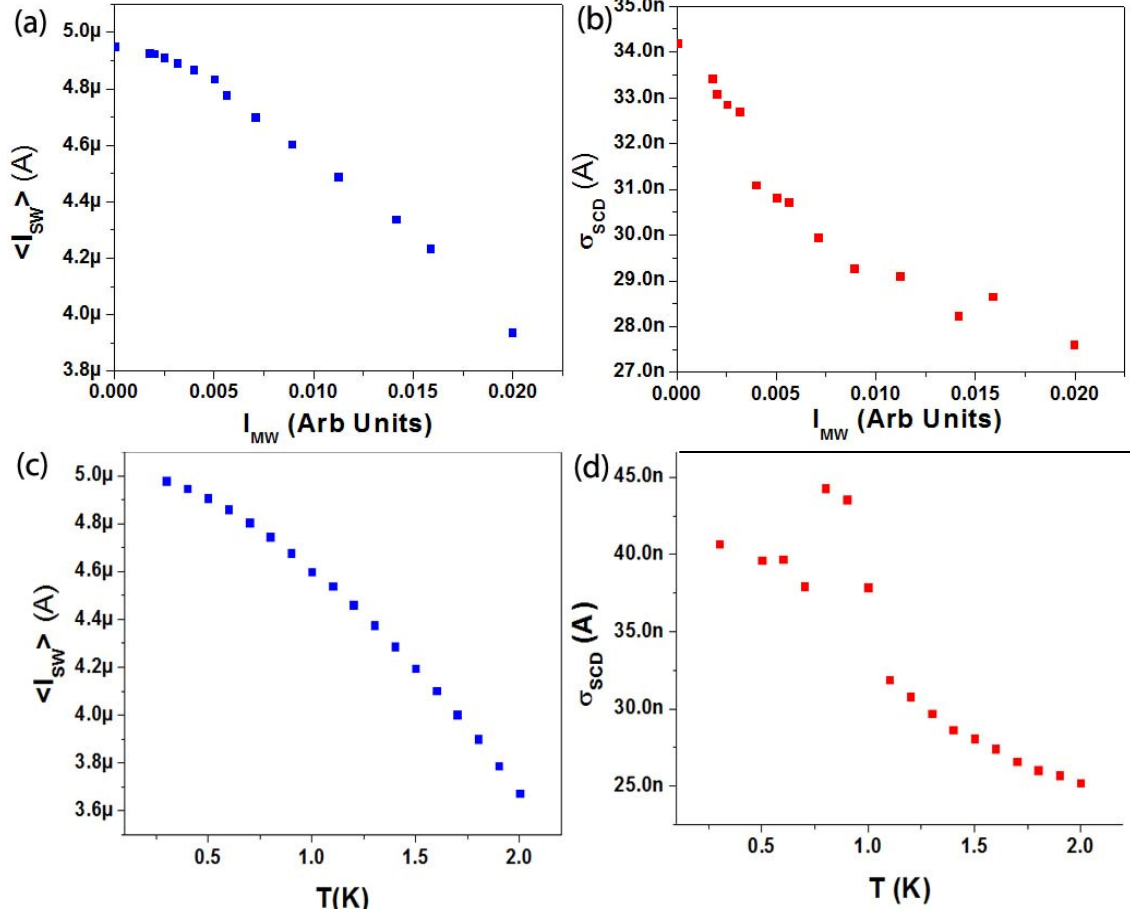


Figure 4.14 Comparison between SCD behavior due to applied MW and temperature. The temperature data have been obtained by M. Sahu. (a) Mean switching current plotted against applied MW current. (b) The standard deviation of the SCD, σ_{SCD} , plotted against applied MW current (c) Mean switching current plotted against temperature (d) σ_{SCD} plotted against the temperature. The outlying points could be due to errant points in the SCD. The two effects are similar, but increasing the temperature does not lead to the formation of a PSC.

The temperature dependence of these transitions in the presence of MWs was also studied. This study was done by measuring 10,000 transitions for $S \rightarrow JNS$ (if present), $S \rightarrow PSC$ (if present), and $PSC \rightarrow JNS$ (if present) for one power slightly below P^* and one above P^* at base temperature. In this case the applied power used was -21.5 dBm and -20.5 dBm. The SCDs taken at -20.5 dBm applied MW power are plotted in Fig 4.15 at temperatures between 318 mK and 1900 mK. This figure shows that the PSC behaves similar to the wire with respect to the temperature evolution of the SCD except that there

is no suppression in switching current until the sample is heated above 500 mK. The lower power case did not have a PSC present at the base temperature of 318mK, but a PSC did form at this power at higher temperatures. Figure 4.16 summarizes these measurements for the switching currents and standard deviations at all temperatures measured. The most important observation is that the standard deviations for the transition $S \rightarrow JNS$ for $P < P^*$ are nearly indistinguishable from the transition $S \rightarrow PSC$ for $P > P^*$ at the same temperature. This observation is another piece of evidence that the same physical process is responsible for the transition out of the superconducting state and into either the PSC or JNS.

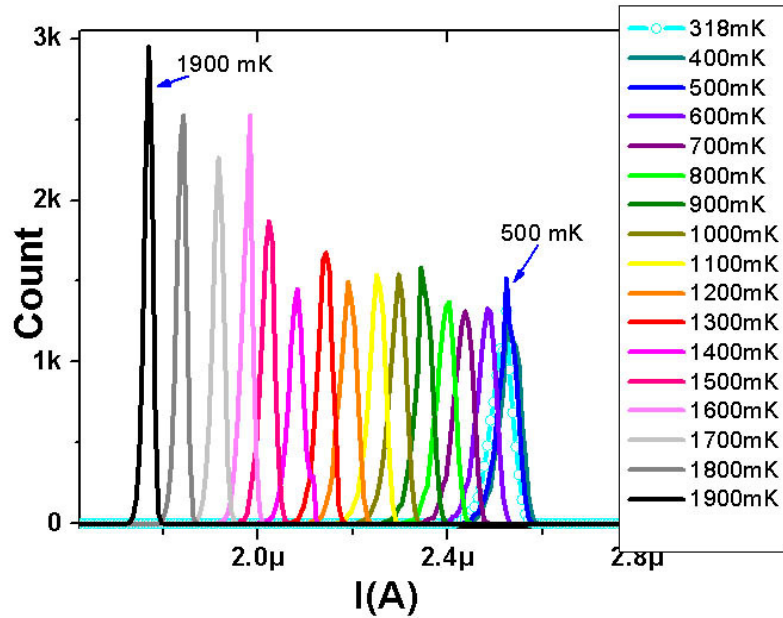


Figure 4.15 Switching current distributions for the transition $S \rightarrow PSC$ for T between 318 mK and 1900mK for sample 091608B. The SCDs for 318, 400 and 500mK are very similar. Data was taken with MW power -20.5 dBm which was greater than P^* . For Higher temperatures the trend is similar to that observed in wires without MW present.

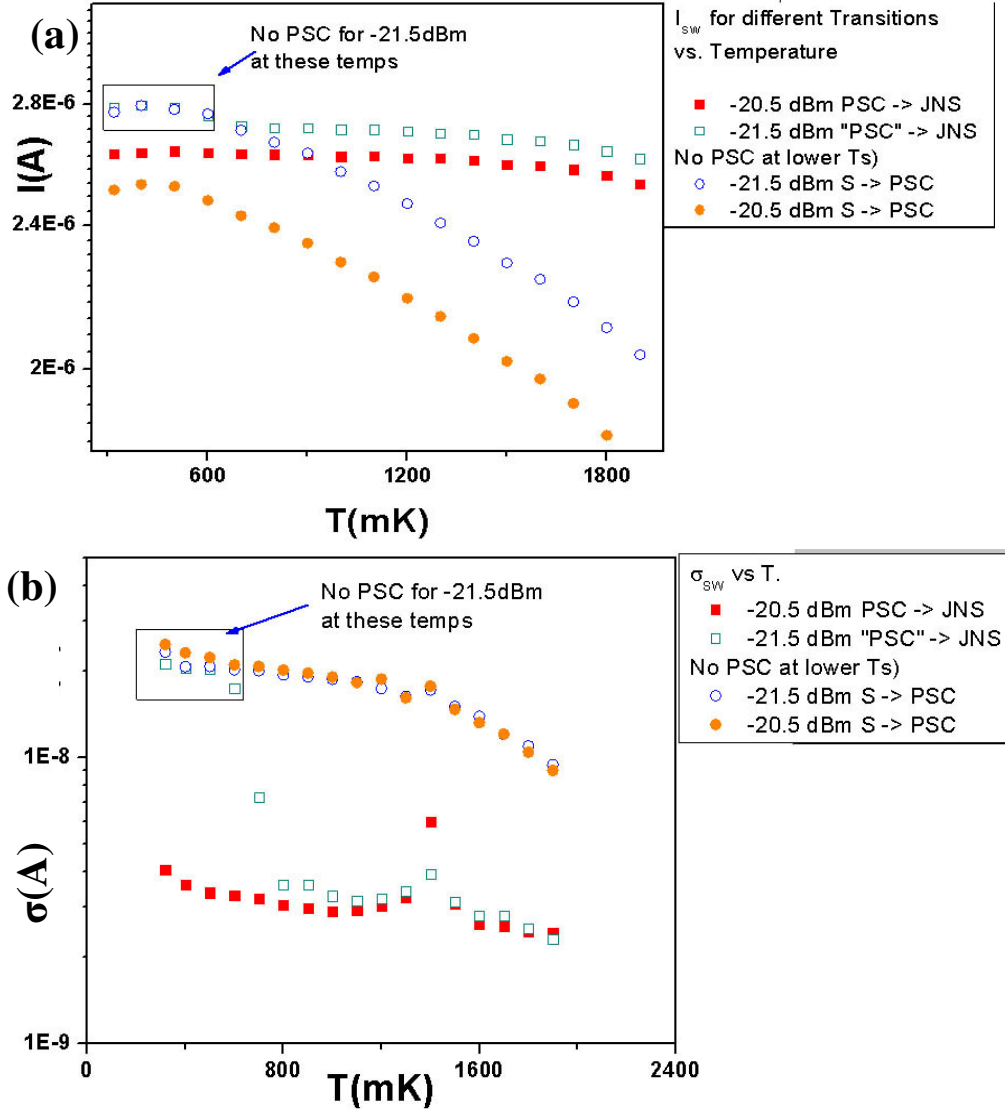


Figure 4.16 Mean switching currents, I_{SW} , and standard deviation, σ_{SW} for vs. temperature for MW $P=-20.5$ and -21.5 dBm for sample 091608B. **(a)** I_{SW} for the 4 transitions shown in the legend. For $P=-21.5$ dBm a PSC is not always present until the temperature is raised to 800mK. **(b)** σ_{SW} for the 4 transitions given in the legend. From this data one can see that σ_{SW} is 3-4nA for the process PSC \rightarrow JNS. Looking at the temperatures where there is no PSC at -21.5 dBm (below P^*) and comparing σ_{SW} to that obtained at -20.5 dBm (above P^*) one can see that they are very similar. The kink in the graph at 1400mK represents a jump in σ_{SW} from 4 nA to 7nA and may be due to one or 2 bad data points in the distribution. These 2 measurements could be removed and not effect any of the conclusions we make.

4.4 Additional Observations

In this section I will discuss several observations that were made that are not well understood. The first will be the low MW frequency behavior of nanowires. Second, I will show results of a zero-crossing voltage branch. Finally I will discuss the behavior of a wire exposed to both magnetic fields and microwaves.

4.4.1 Low Microwave Frequency Response

When our wires are exposed to MW radiation in the range of 100-200 MHz an anomalous type of phase slip center occurs. Figure 4.17 shows a $V(I)$ curve for sample MS2. The main difference between these steps and the PSC observed at higher MW frequency is that they do not show Shapiro steps, and they have a very low resistance. If these steps were analyzed in the manner presented in section 4.2.1 they would have a very large negative offset current. It is also possible to observe 2 such steps on short wires, something we have not seen with higher frequency MW stabilized PSCs. These flat steps only appear for very low frequencies and their behavior appears to be distinct enough from the higher frequency PSCs that they may be due to a different underlying mechanism. This phenomenon was not studied in depth, but it is interesting enough to acknowledge. These low frequency PSCs do not follow any of the predictions by the traditional SBT phase slip model. For example, the phase slip core size (give the estimated value) estimated from the resistance (give the value) corresponding to these steps is much less than the coherence length, which is already quite small (5-10 nm). Such small core size is unphysical. This effect would make an excellent future study.

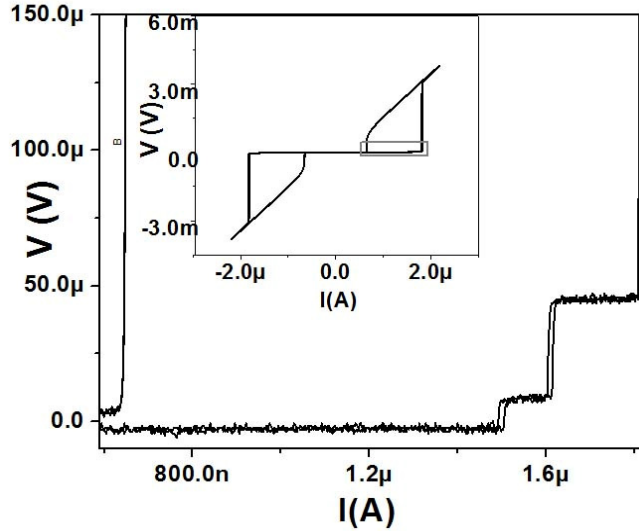


Figure 4.17 Voltage-current characteristic for sample MS2 with MW at 100 MHz and $T = 300$ mK. These steps do not correlate with the Josephson relation and have a very small slope. There are also 2 of these steps unlike our observations of the PSC at higher frequencies, which always showed just one step. Inset: Full $V(I)$ curve showing region zoomed in on for main graph.

4.4.2 Nanowire as a Rectifier

Another phenomenon that was only observed at lower frequency was the appearance of zero-crossing voltage steps in sample MB2. Zero-crossing means that there is a finite voltage on the wire at zero applied bias current, as in Fig.4.18. In other words, a part of the applied microwave signal is rectified by the superconducting nanowire and leads to a constant dc voltage. These results were similar to what we observed in focus ion beam milled BiSCCO Intrinsic Josephson Junction (IJJ) samples [13]. The phenomenon of zero-crossing is not well understood in any superconducting system. Figure 4.18 shows measurements of this phenomenon on sample MB2. This behavior is interesting because it may show evidence for a ratchet potential in our wires under certain conditions, occurring, for example, due to the multi-valued current-phase relation.

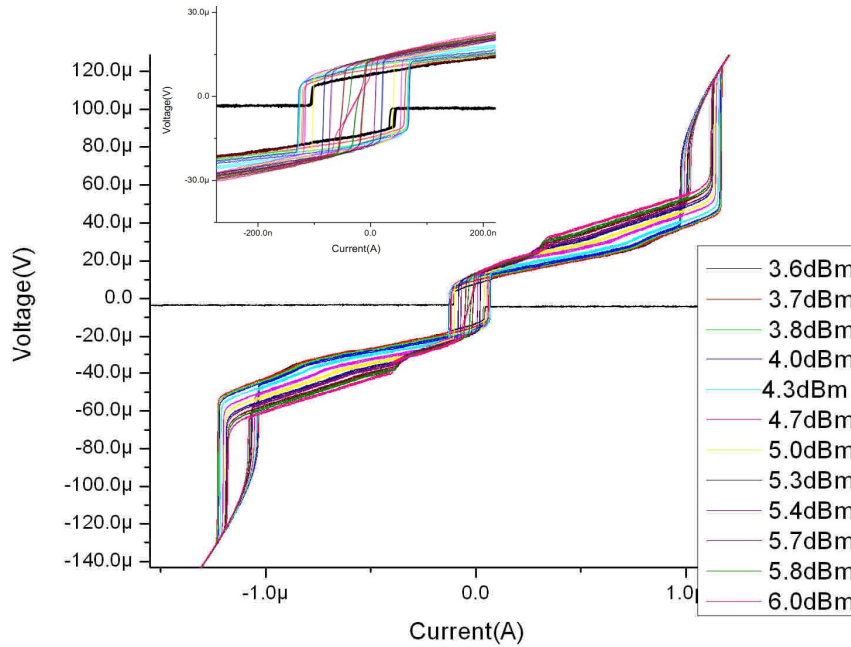


Figure 4.18 Zero-crossing voltage steps in sample MB2 for different MW powers at 320 MHz. Inset shows zoomed in region to highlight the zero-crossing. The shape of these curves are very similar to those observed in IJJs [13]. The curve for applied MW power of 3.6 dBm is emphasized to show that it retraps to the zero voltage state unlike the other curves

4.4.2 Magnetic Field Response

We can apply a magnetic field to our wires while exposing them to MW radiation. These experiments were performed with the wire and film both oriented perpendicular to the applied magnetic field. What we observed is that an applied magnetic field suppresses the MW response in our wires. This observation is similar to those of Anderson and Dayem who attributed this to the presence of vortices in the film [5]. We tried to observe some evidence of an oscillation in the switching current with applied B field similar to what is observed in Josephson Junctions (JJ) [14]. It was thought that the MW PSC might behave more like a JJ when exposed to a magnetic field and exhibit some oscillation in its critical current. Figure 4.19 shows several $V(I)$ curves measured at different field strengths. Applying a magnetic field does reduce the effects of the MW

quite dramatically, however there is some sign of an oscillation. Perhaps vortices in the film are masking the oscillation of the critical current. Figure 4.20 shows switching current vs. magnetic field. Here 100 values for the switching current are recorded for each value of magnetic field and plotted vs. the field strength. The curve taken at the higher microwave power shows some signs of an oscillation.

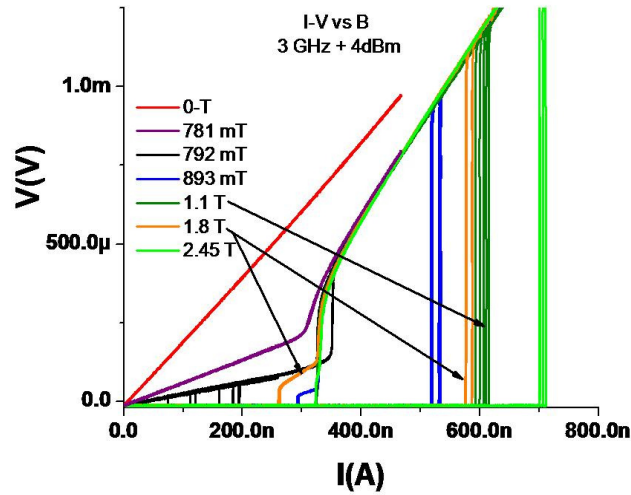


Figure 4.19 Voltage-current characteristics with MW at 3GHz and +4dBm for 7 different values of the applied magnetic field for sample 121707B. The Switching current increases with applied magnetic field as the effects of the MW are diminished, however there is a sign of non-monotonic behavior because the switching current increases when the field is changed from 1.1 T to 1.8T.

These results are not conclusive enough to determine whether or not there is some oscillation of the critical current the PSC with applied field. The observed non-monotonic behavior can be due to local magnetic moments present on the wire surface, similar to the results published by Rogachev et al. [15] and analyzed theoretically by T. C. Wei et al. [16]. It is also possible that vortices entering the film are masking this effect. A good future experiment would be to perform these measurements again on a sample that was oriented so that the wire was perpendicular to the magnetic field with the film parallel. This configuration would ensure that no vortices would enter the film due to the applied field and also ensure that we were able to get a few flux quanta through the wire because the largest area of it would be penetrated by the field.

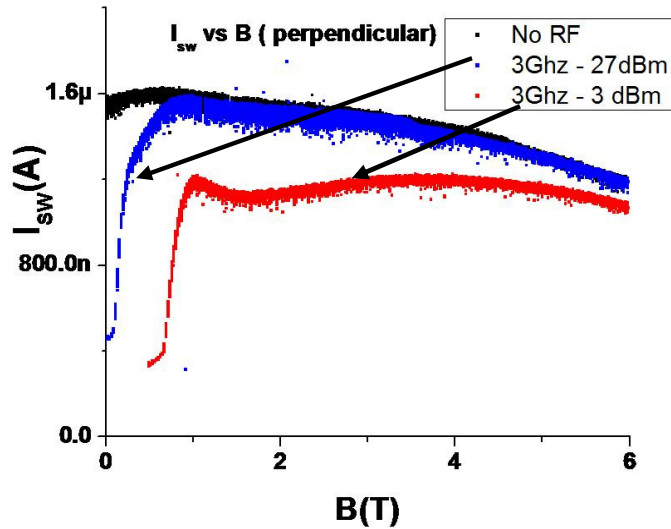


Figure 4.20 Switching current vs. applied magnetic field for sample 121707B. Here 100 measurements for the switching current were taken at each value of the applied field. Curves were taken with no MW and for 2 different MW powers at 3 GHz. The curve taken at the higher MW power shows some sign of an oscillation.

4.5 Summary of Microwave Effects

The physical properties of microwave induced PSCs were examined in detail in this chapter. We compare the transitions $S \rightarrow \text{JNS}$ in the absence of microwaves and at low to intermediate MW powers to the transition $S \rightarrow \text{PSC}$ at sufficiently high MW powers. We present strong evidence that those transitions are triggered by the same mechanism, most probably a single phase slip event. In Fig. 4.4a it is shown that the mean switching current for the $S \rightarrow \text{JNS}$ follows a continuous trend into the $S \rightarrow \text{PSC}$ transition when the PSC appears at power P^* . In Figure 4.11 we show that the standard deviation of the $S \rightarrow \text{JNS}$ transition at powers below P^* is very similar to that for the $S \rightarrow \text{PSC}$ transition at powers above P^* . The most convincing evidence for this claim is presented in Fig. 4.16 where the standard deviation is compared for $S \rightarrow \text{JNS}$ and $S \rightarrow \text{PSC}$ transitions and is shown to be nearly identical for the two processes. We thus conclude that the underlying process leading to this transition is the phase slip process.

Further by comparing our results with the Giordano model [10] for the quantum phase slip rate we are able to understand the results and suggest that a single quantum phase slip can lead to a switching event. The model also produces the same suppression in mean switching current with applied MW power that we observe in our wires. Therefore we conclude that a single quantum phase slip in the presence of MW radiation can trigger a phase slip center in superconducting nanowires.

4.6 References

-
- [1] W. Skockpol, M. R. Beasley, and M. Tinkham, *J. Low. Temp. Phys.* **16**, 145 (1974).
 - [2] M. Tinkham, J. U. Free, C. N. Lau and N. Markovic, *Phys. Rev. B.* **68**, 134515 (2002).
 - [3] M. Sahu, et al. arXiv:0804.2251v1 (2008).
 - [4] N. Shah, D. Pekker, and P. M. Goldbart, *Phys. Rev. Lett.* **101**, 207001 (2008).
 - [5] P. W. Anderson and A.H. Dayem, *Phys. Rev. Lett.* **13**, 195 (1964).
 - [6] J. D. Meyer, *Appl. Phys.* **2**, 303 (1973).
 - [7] Y.Koval, M. V. Fistul, A. V. Ustinov, *Phys. Rev. Lett.* **93**, 087004 (2004).
 - [8] A. T. Bollinger, A. Rogachev, A. Bezryadin, *Europhys. Lett.* **76** 3 505-511 (2006).
 - [9] T. A. Fulton & L. N. Dunkleberger, *Phys. Rev. B.* **9**, 4760–4768 (1974).
 - [10] N. Giordano, *Phys. Rev. Lett.* **61**, 2137 (1988).
 - [11] M. Tinkham and C. N. Lau, *App. Phys. Lett.* **80**, 2946 (2002).
 - [12] J. Bardeen, *Rev. Mod. Phys.* **34**, 667–681 (1962).
 - [13] Myung-Ho Bae, R. C. Dinsmore III, M. Sahu, Hu-Jong Lee, and A. Bezryadin, *Phys. Rev. B* **77**, 144501 (2008)
 - [14] M. Tinkham, *Introduction to Superconductivity*, 2nd ed. (McGraw-Hill, New York, 1996).
 - [15] A. Rogachev et. al., *Phys. Rev. Lett.* **97**, 137001 (2006).
 - [16] T. C. Wei, D. Pekker, A. Rogachev, A. Bezryadin, P. M. Goldbart, *Euro. Phys. Lett.* **75**, 943 (2006).

Chapter 5

AC Josephson Response in Superconducting Nanowires

In this chapter I will discuss the dynamic superconducting state and its interaction with microwave radiation in quasi-one-dimensional nanowires. The most pronounced feature of this interaction is the Shapiro steps. On the $V(I)$ curves of our nanowires we observe integer as well as fractional Shapiro steps, which are explained by a numerical model involving non-sinusoidal current-phase relationship of nanowires. Much of what is discussed here and the data I obtained also appears in the publications [1,2]. I will begin by discussing our experimental procedure and results and then move on to the numerical simulations and the model we use to describe this phenomenon.

5.1 Observation of Shapiro Steps in Superconducting Nanowires

All experiments were performed in our ^3He cryostat following the measurement procedure outlined in Chapter 2 for measuring $V(I)$ characteristics and dV/dI curves. The microwave radiation (MW) is fed in through the coaxial cable and the power and frequency is controlled either manually or by LabView program. The MW signal is capacitively coupled to the sample via an antenna on the bottom of the sample Faraday cage. Because of this we can only perform studies at certain resonant frequencies corresponding to resonances of the Faraday cage. These frequencies also vary slightly from sample to sample. Using this method we also cannot determine the absolute value

of the MW power that reaches the wire itself. We can only compare applied powers at the same frequency.

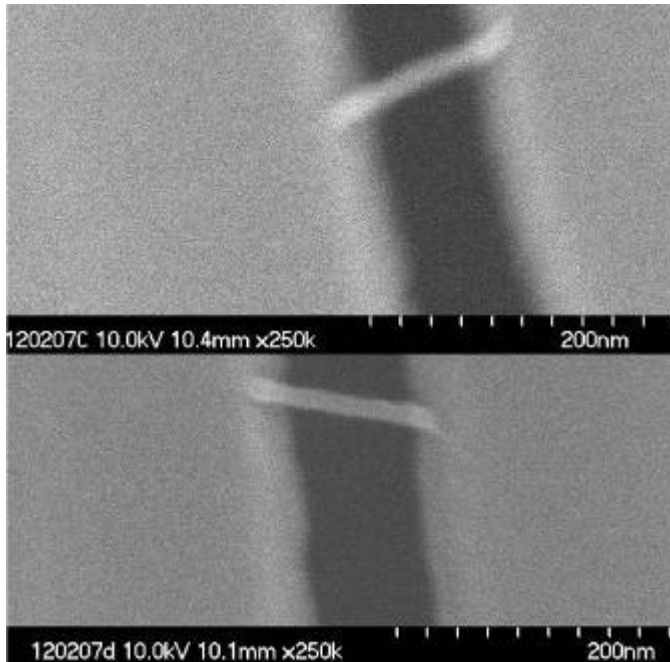


Figure 5.1 SEM images for Sample 121707 C and D. Sample 121707 C is 130 nm long and Sample 121707D is 140nm Long

The general behavior of the $V(I)$ curves consists of 2 distinct types of behavior. The first is that as the microwave power is increased from zero, the switching current of the wire is suppressed. This phenomenon is discussed in detail in Chapter 4. At sufficiently high MW power a new dynamic superconducting state, i.e. a phase slip center, appears in the $V(I)$ curve. Shapiro Steps (Ss), representing lock-in resonances, appear on this branch; yet they do not appear after the wire switches to the JNS branch, indicating that we are correct in calling that a normal state. Ss appear at voltages that correspond to integer multiples of the microwave photon energy, i.e. satisfy the relationship $2eV=hf*n$, for n an integer for the so called integer steps or n can be a fraction for fractional steps, which we observe in our wires. These observations are similar to the observations of Anderson and Dayem on their thin film constrictions [3]. Fig 5.2 shows this behavior for sample 121707D.

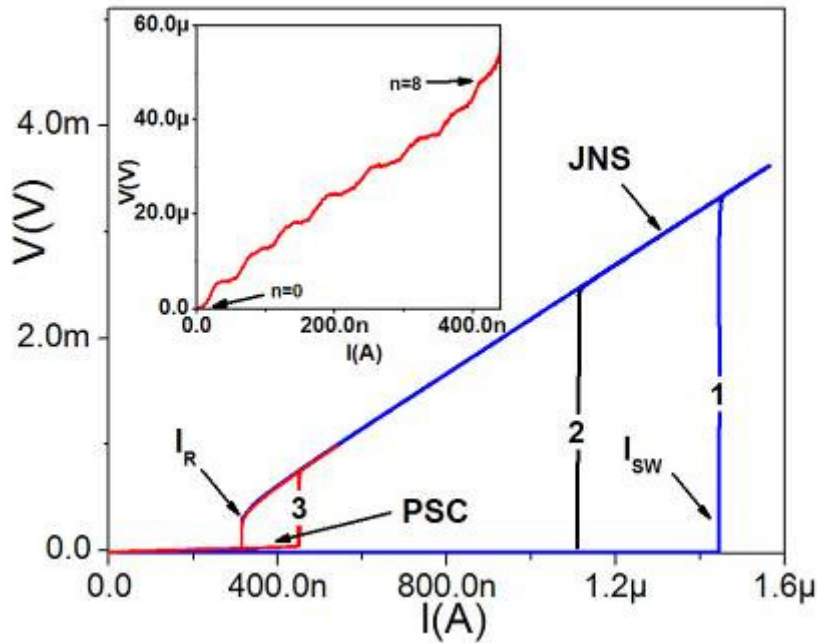


Figure 5.2 $V(I)$ characteristics for sample 121707D for 3 different MW powers at 3GHz. The switching current, I_{SW} , retrapping current, I_R and PSC and JNS are all indicated with arrows. The power setting as read from the source are: Curve 1 is with no MW, Curve 2 and 3 are at -31dBm and -21dBm. Inset. Lower bias measurement for -21dBm. Here the bias current is kept just below the switching current so that many curves could be averaged. The $n=0$ and $n=8$ Ss are indicated with arrows.

$V(I)$ characteristics are not adequate for studying the AC Josephson response in detail. This is due to the fact that the steps are rather noisy and they are not very strongly pronounced. Also there is quite a bit of hysteresis in the $V(I)$ curves which make averaging many curves impractical. Because of this much of the work is done by measuring dV/dI curves. Our method for measuring dV/dI allows us to average many curves for each data point and we are able to resolve details that are difficult to see in $V(I)$ curves. By employing this method we are able to observe resonances in the dV/dI curves that correspond to fractional Ss. The lock-in resonances appear in the dV/dI vs. I data as local minima. Our dV/dI program also records average V vs. I data which gives $V(I)$ curves. Figure 5.3 shows data obtained by this method for sample 120207C at 8 GHz.

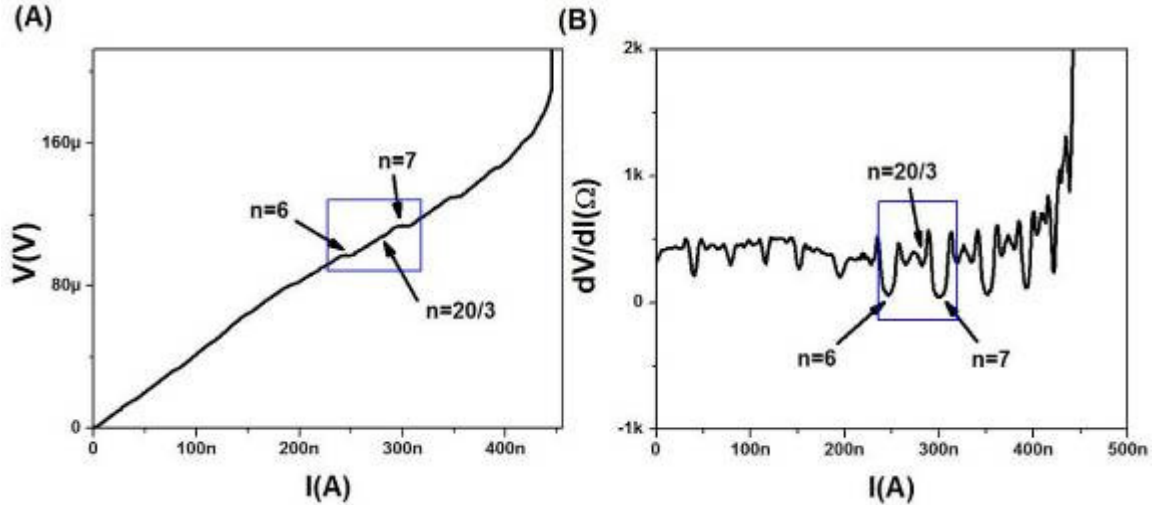


Figure 5.3 Data for sample 121707 C at 8GHz at -5.9 dBm taken using our dV/dI Labview program. (A) a $V(I)$ curve and (B) the corresponding dV/dI curve from the same measurement. The boxed region shows the same current interval in each graph. The fractional steps are very easily seen in the dV/dI curve but are just slightly visible in the $V(I)$ curve.

The first sample to be extensively studied was sample MB1. The largest collection of data for this sample was $V(I)$ and dV/dI data obtained at 7.34 GHz at various applied powers. Figures 5.4 and 5.5 summarize this data and show $\frac{1}{2}$ integer Ss. The first thing to notice here is that the phase slip center first appears in the retrapping branch for this sample at this frequency and the first step to appear is the $n=3$ step. These missing steps are similar to that observed in quasi-2D structures, the so called Dayem bridges first studied by Anderson and Dayem in 1964 [3]. As the power is increased, higher integer steps appear before the $n=2$ and $n=1$ steps do. When these lower n steps appear the $V(I)$ curve appears to have a higher average slope for the low biased region that it does for the region before it transitions to the JNS. This behavior produces what appears to be a kink in the $V(I)$ curve and is observed in all samples. Because of this, for sufficiently high powers, the lower integer steps are considerably less pronounced than the higher integer steps.

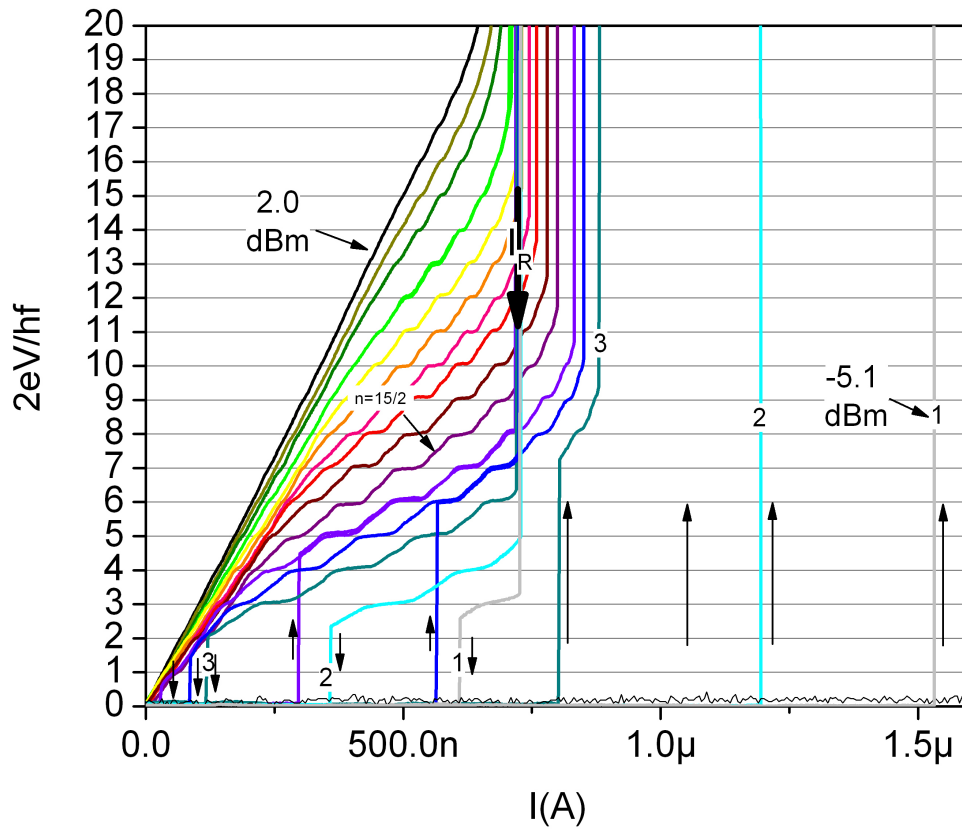


FIG. 5.4 Current-Voltage characteristics for sample *MS_1* as microwave power is increased from the onset of the PSC at -5.1dBm up to 2.0dBm . The voltage is normalized by the photon energy hf . The first 3 curves are numbered for clarity. Curve 1 ($P = -5.1\text{ dBm}$) shows the onset of the PSC and the $n=3$ Shapiro step at the return branch. Curve 3 shows the onset of the PSC in the switching branch.

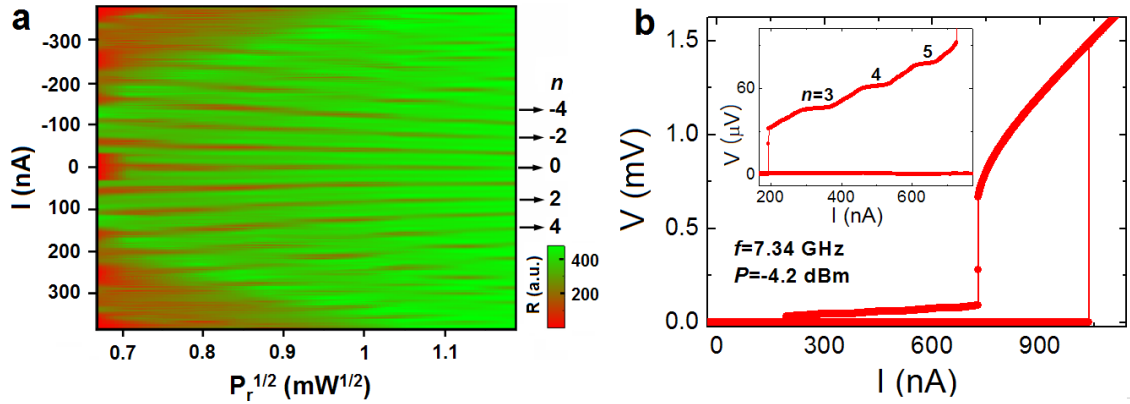


Figure 5.5 **a**, $dV/dI-I-P_r^{1/2}$ plot of sample MB_1 at $f=7.34$ GHz **b**, I-V curves showing the supercurrent branch and the phase-slip branch at the same current range under microwaves. Inset: I-V curves in a low voltage regime, where the resonance steps are shown as indicated by index numbers. (This figure also appears in the supplementary online material for this reference [2])

The Power dependence for the size of the steps was studied for sample 121707D. Figure 5.6 shows the results for the first time it was measured. Before we discuss our results, we remind that in regular Josephson junctions the size of each Shapiro step is described by a Bessel function of the applied MW power. Let us now consider the results obtained on our nanowires. At powers slightly greater than P^* only the $n=2$ step is present in this wire at This graph shows how the lower integer steps get quickly suppressed to a point below which we cannot accurately measure the step width and remain suppressed while the higher order steps appear. The step widths were determined graphically as depicted in the top graph of Fig. 5.6. Many curves were taken for each power and the raw data was sorted and averaged to produce the red curve (Fig 5.6b). Lines were drawn in by hand as shown and their points of intersection were used to determine the step width. This method did not work well for very small steps. These steps do not follow the normal Bessel Function behavior for Josephson Junctions(JJs), nor do they resemble other results obtained for current biased JJs [4]. Later in this chapter I will discuss this difference in the context of the Resistively Shunted JJ model and numerical simulations using a model based on a multi-valued current-phase relationship.

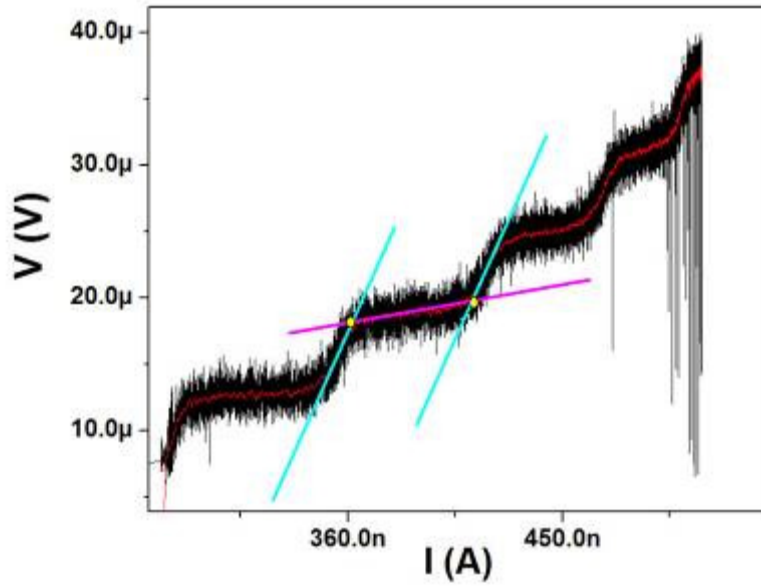
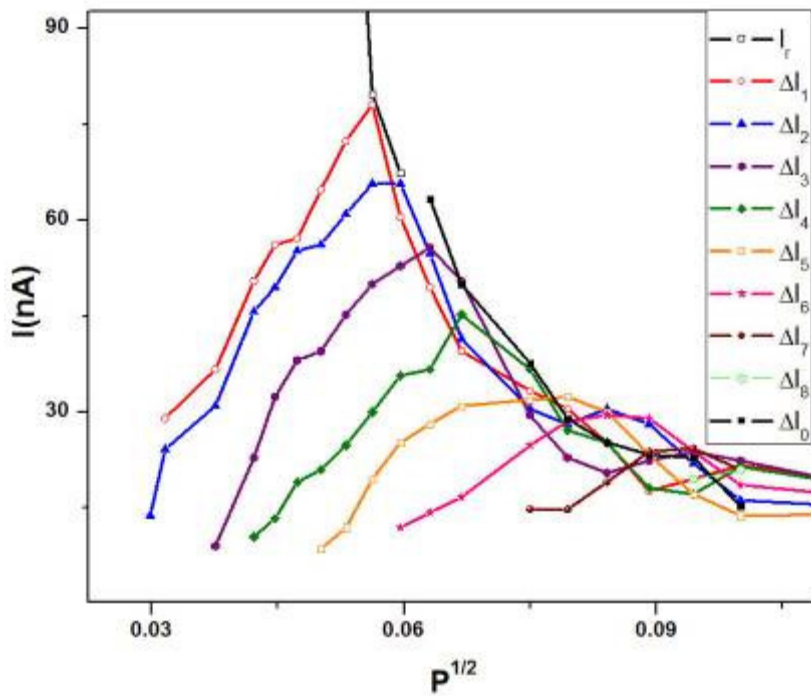


Figure 5.6 Shapiro Step width for increasing MW power for sample 121707D taken at 3GHz. Top: Sample $V(I)$ curve showing how the step width was obtained. The step width was found by taking the distance between the 2 yellow dots on the I -axis. Bottom: Power dependence for the Ss. The steps do show some oscillation with power, but quickly hit the detection level, which is about 10-15 nA.



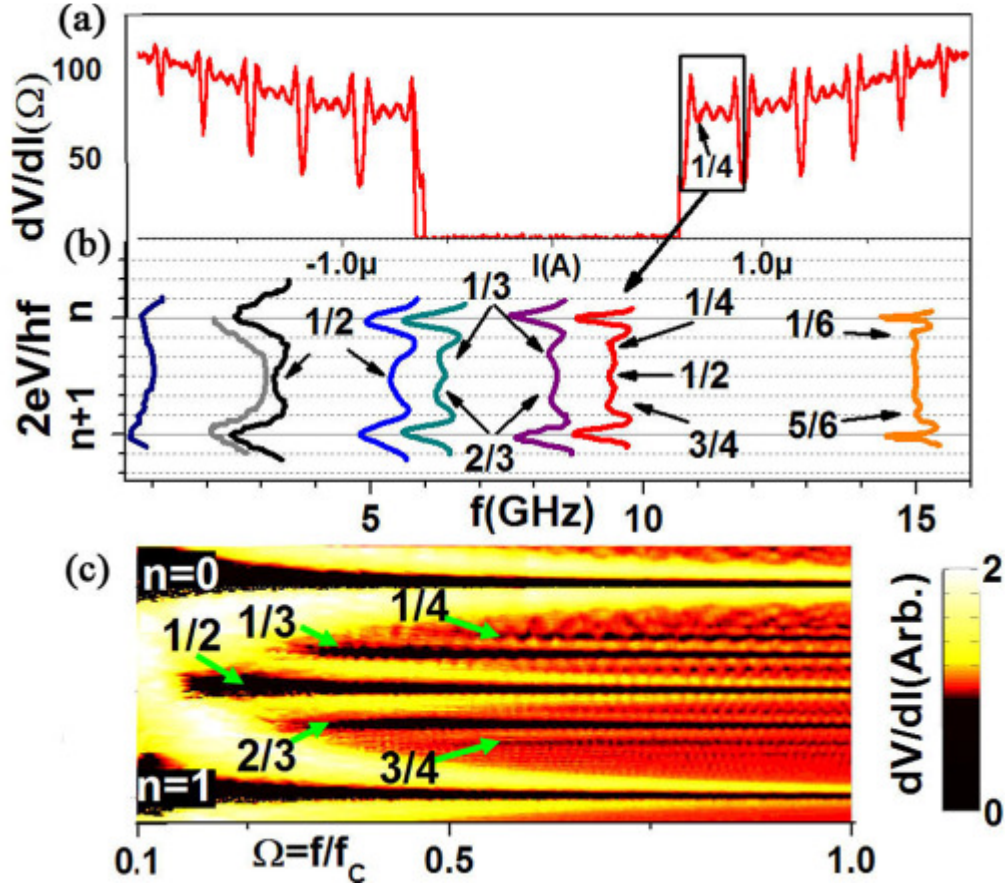
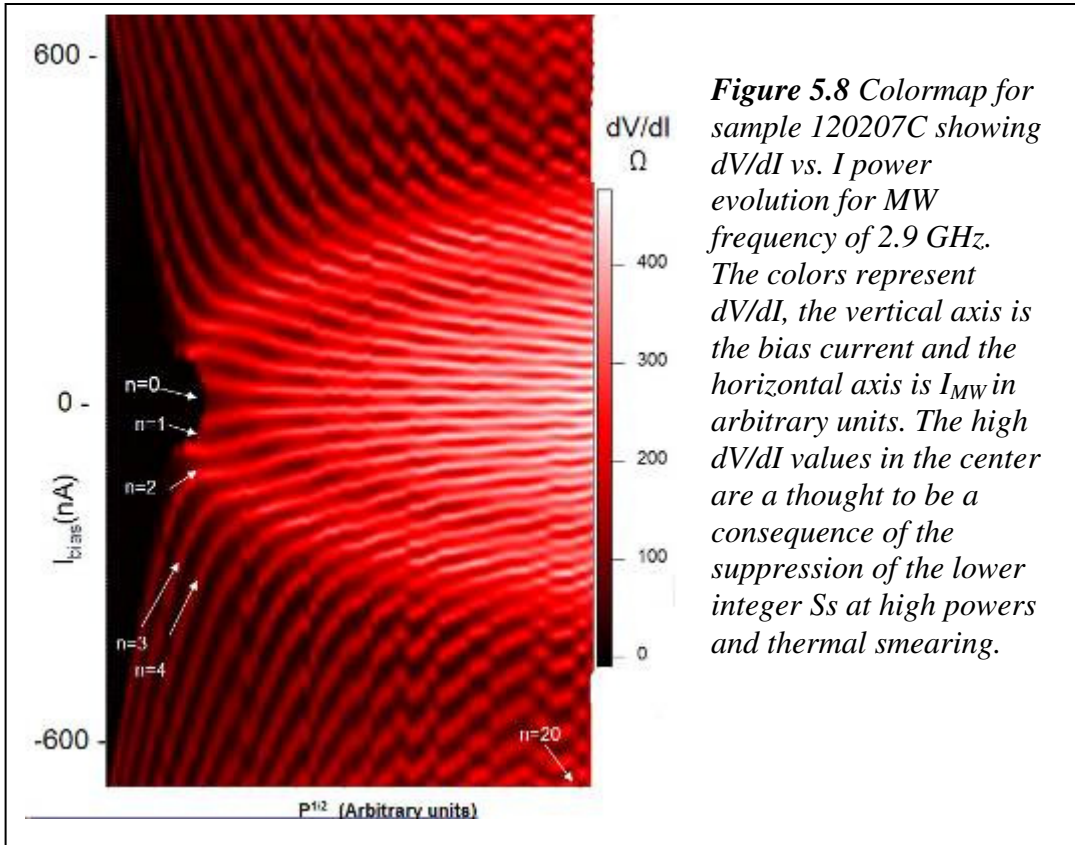


Figure 5.7. (a): dV/dI for sample 121707C taken at 9.5 GHz and 500 mK showing clear $1/4$ resonances. Boxed region portion of the curve plotted in (b) which is between step $n=3$ and $n=4$ (b): Frequency evolution for sample B. The horizontal axis is normalized dV/dI centered on the frequency it was obtained at. The vertical axis is normalized voltage, $2eV/hf$. The frequencies starting from the left in GHz: 0.9, 2.7, 2.9, 5.4, 6.2, 8.2, 9.5, 15. The appearance of fractional steps is indicated by arrows. (c) Numerical simulation for all the resonances between the $n=0$ and $n=1$ step using the current-phase relationship (CPR) and model described in section 5.3 as a function of the normalized frequency, $\Omega=f/f_c$, $f_c=2eI_cR_N/h$ taken at $Irf = I_c$ and $L/\zeta=130/6$.

An interesting behavior observed in these experiments is the appearance of fractional Shapiro steps at higher frequencies. As one can see in Fig 5.4, sample MB_1 shows $1/2$ steps at 7.38 GHz, these $1/2$ steps were not observed at 3GHz. At first this was thought to be due to our inability to distinguish these steps with our system, however what was observed with sample 121707C led to a reinterpretation of these results. This sample

showed strong resonances, especially well pronounced as local minima in the dV/dI curves, at frequencies above 8 GHz. It was the only sample to really do so. Others showed only slight suppression of the switching current at higher frequencies, but this sample showed a PSC at frequencies between 8-9.5 GHz and near 15 GHz. This sample showed higher order fractional steps at higher frequencies. As the frequency is increased the order of fractional steps that are observed also increases. Figure 5.7b summarizes this behavior. This sample only shows integer resonances for frequencies below 2.9 GHz, but shows half integer resonances abruptly at 2.9GHz. At higher frequencies we observe $\frac{1}{3}$, $\frac{1}{4}$. And even $\frac{1}{6}$ resonances. This data was obtained by fine tuning the setup and taking dV/dI curves with high averaging. Even as such the results were just on the edge of the system's resolution and it is possible that noise or resolution limitations obscure some of the details (See Appendix).

Under less optimal conditions than those used to measure the data for Fig 5.7, dV/dI vs. MW power was measured for this sample at 2.9 GHz and 8 GHz to produce 2d Color maps. Figures 5.8 and 5.9 show this. For 2.9 GHz only integer resonances were visible, but at 8.07 GHz $\frac{1}{3}$ resonances are clearly present, however they do not show well in the colormap (See Fig 5.3 above for a single curve from this data set). Both frequencies show a region of higher dV/dI for low bias current and high MW power. We attribute this partly to the suppression of low integer Ss for high MW power and to some smearing of these resonances dues to noise, thermal fluctuations, or AC excitation current. A $V(I)$ curve with many small, noisy Ss, will appear to have a higher average slope than a $V(I)$ curve with many large clear Ss.



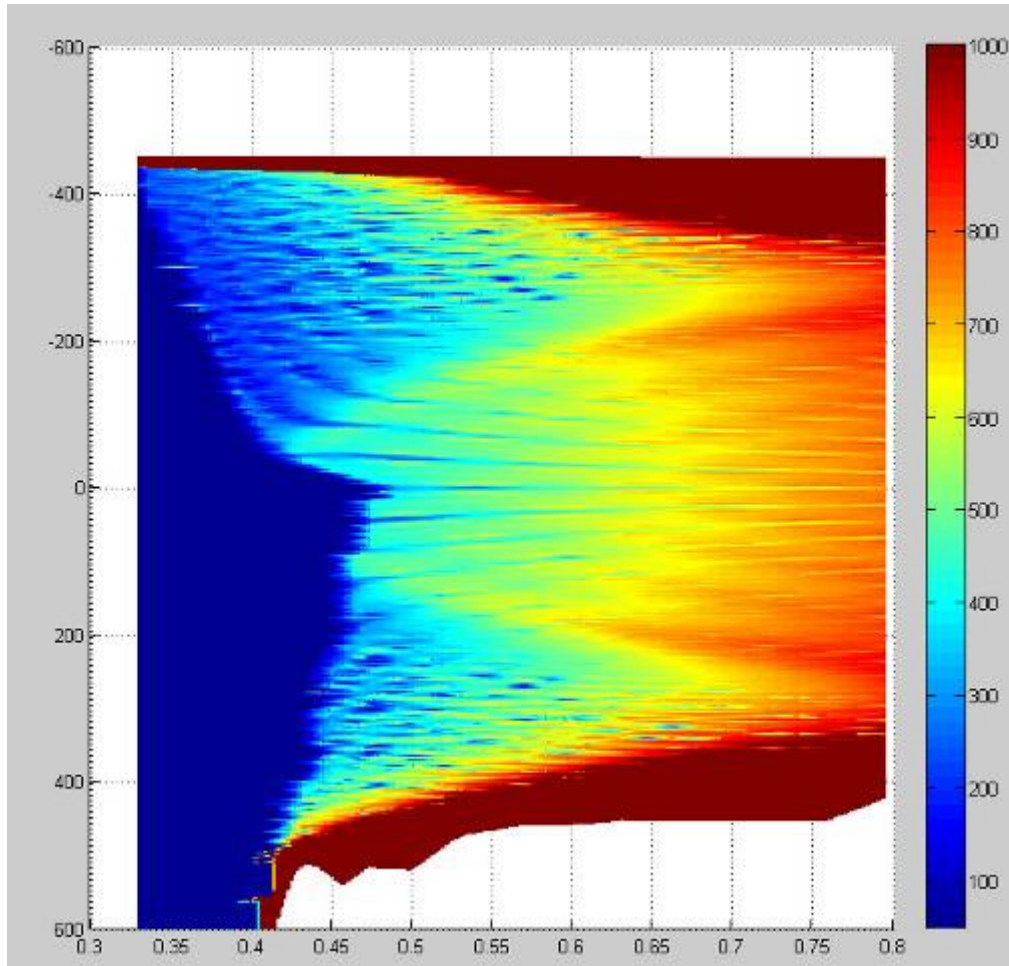


Figure 5.9 Colormap for sample 120207C at 8.07 GHz. The color scale shown on the right is for dV/dI in Ohms, the vertical axis is current in nA and the horizontal axis is I_{RF} in arbitrary units. It is just possible to observe the $1/3$ resonances. Most of the features at low RF power are artifacts from the data and plot method. See Fig 5.3 for a graph of on RF power for this data set.

5.2 Modeling Our Results

5.2.1 McCumber-Stewart model for resistively shunted superconducting junctions

The system is modeled using the resistively shunted JJ, (RSJ) model, which is the limiting case for the RCSJ model discussed in chapter 1 with $C=0$ [5] for the case of an overdamped junction.

$$d\phi / d\tau + I_S(\phi) = i_{dc} + i_{ac} \sin(\Omega\tau) + \eta(T, \tau) \quad (5.1)$$

Here ϕ is the phase difference across the length of the wire, $\tau [=2\pi f_c t]$ is the dimensionless time, t is the time, $\Omega = f/f_c$, and i_{dc} and i_{ac} are, respectively, the DC bias current and the AC bias current induced by an external microwave normalized by I_C , the critical depairing current, and $I_S(\phi)$ is the current-phase relationship (CPR). The characteristic frequency, given by $f_c = 2eI_C R / h$ accounts for the resistance of the normal current channel, R , and the critical current of the wire and $\eta(T, \tau)$ represents thermal fluctuations and is incorporated into simulations by adding the term $2e / \hbar \sigma \sqrt{2k_B T t R}$ to the phase computation where T is the temperature and t is the time-step and σ is a Gaussian random variable with $\langle \sigma^2 \rangle = 1$ [6]. The analysis presented here is based on the simplifying assumption that our wires are overdamped. The analysis presented below could be readily extended to the underdamped case as well.

The CPR for a traditional JJ is purely sinusoidal, i.e. $I_S(\phi) = I_C \sin(\phi)$. As discussed in Chapter 1, a sinusoidal CPR can lock-in with an external AC signal to produce current steps (or, in other words, constant voltage plateaus) in the $V(I)$ characteristics for these systems at voltages given by $V_n = n * hf / 2e$ with V_n the voltage at the n th current step, n an integer, e the charge of the electron, h the Planck constant, and f the frequency of the external AC signal. Other types of superconducting junctions,

such a π -junctions [7] may have a CPR with higher order terms such as a term, $I_2 \sin(2\phi)$. In general a CPR for a superconducting junction could be given by $I_s(\phi) = \sum_m I_m \sin(m\phi)$ where m can range from 1 to any positive integer, the highest of which we denote m_{\max} . Such a CPR would produce Ss that go as $V_{n,m} = n / m * hf / 2e$ with n and m integers. Such a CPR would produce fractional Shapiro steps up to the order m_{\max} . A CPR of this fashion is not sufficient to model our results because we see higher order fractional steps at higher frequencies. This CPR would, in the absence of thermal fluctuations, and other sources of noise, lead to fractional steps up to order m_{\max} .

Our nanowires are quasi one dimensional so they are not expected to have a sinusoidal CPR. One such model CPR can be derived from the Ginzburg-Landau equations in the limit of a one dimensional weak link [8]. For wires of intermediate to long length the phase difference across the length of the wire could be significantly greater than 2π and still be fully superconducting just so long as quantum phase slips are not frequent [9,10]. This CPR is given by following equation derived by Likharev [11,12]:

$$I_s(\phi) = \frac{I_C 3\sqrt{3}}{2} \frac{\phi}{(L/\xi(T))} \left[1 - \left(\frac{\phi}{(L/\xi(T))} \right)^2 \right] \quad (5.2)$$

with ϕ the phase difference across the entire wire, L the length of the wire, $\xi(T)$ the temperature dependant coherence length, and I_C is the critical depairing current. This function is valid in the limit $L \gg \xi$ and gives the stable branch of a multi-valued CPR that takes into account the existence of PSCs in superconducting nanowires (see Fig. 5.10). This function alone does not meet all of the physical requirements of a CPR [12]. These requirements are as follows. The CPR must be 2π periodic, must be equal to zero at $\phi = \pi$, and must be an odd function. These requirements are satisfied by allowing the CPR to be multi-valued. For a multi-valued CPR the phase can increase past π without a sign change in the CPR. Once the phase increases to its critical value corresponding to $I_S = I_C$, the CPR turns back on itself, to cross the axis at π . This new branch of the CPR has the opposite curvature from that of the other branch near the critical current and is

unstable. As such the system never attains these values, but instead ends up on another stable branch that is shifted by 2π from the previous branch by undergoing a phase slip. The inset of Fig. 5.10 shows this process diagrammatically. The maximum phase for this relationship is given by

$$\phi_{max} = \frac{L}{\sqrt{3}\xi(T)} \quad (5.3)$$

and $\phi_{min} = -\phi_{max}$. When the ratio $L/\xi(T)$ is greater than 5.4 ϕ_{max} exceeds π and the CPR as used in our model is in the multi-valued regime. The numerical simulation is only used for values of $L/\xi(T)$ in this regime. The CPR for 1-D weak links as derived by Likharev attains some multi-valued nature for $L/\xi(T) = 4$, however this regime was not considered for this model because our wires have $L/\xi(T) \sim 10$ or greater.

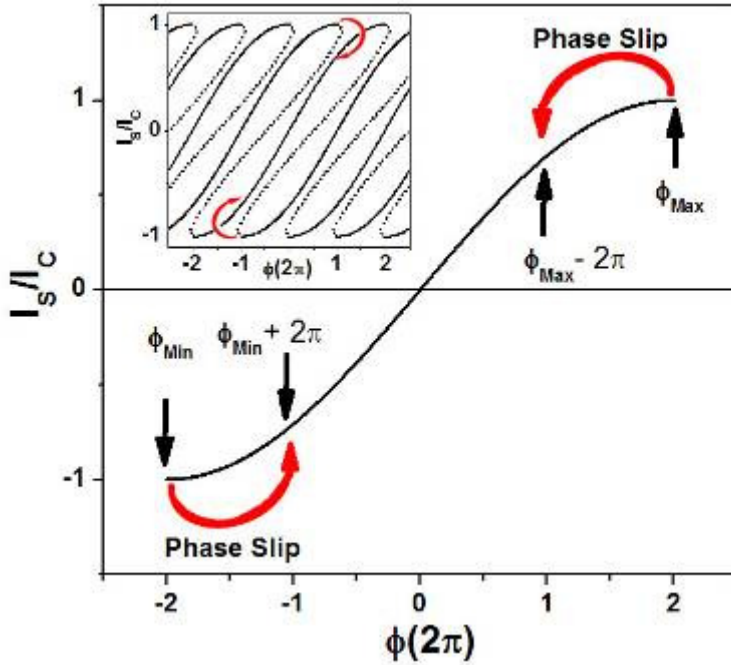


Figure 5.10 Schematic of the Current-Phase relationship (CPR) used in numerical simulations. When the supercurrent in the wire hits I_c a phase slip occurs and the phase changes by $\pm 2\pi$ depending on the sign of the supercurrent. After the phase slip process occurs the amount of supercurrent in the wire is given by the CPR evaluated at $\phi_{max} - 2\pi$ or $\phi_{min} + 2\pi$ as indicated by the red (curved) arrows. Inset: Full multi-valued CPR. The solid curves are the stable branch described by equation given in the text. The dotted

line shows the unstable branch which is not used in our model. Here the Arrows show how a phase slip is equivalent to moving to the adjacent stable branch instead of traversing the unstable region

Another possible CPR for nanowires was derived by Khlebnikov [10,13]:

$$I_s = I_c \left(\frac{\phi}{\pi} - \left(\frac{\alpha}{I_c} \right)^2 \frac{1}{2\pi^3} \frac{\phi}{(1 - (\phi/\pi)^2)} \right) \quad (5.4)$$

This CPR was derived for the case when there are frequent quantum phase slips (QPS). The function as written is not a valid CPR because it has a singularity at $\phi = \pi$. To use this function in as a model we allow the phase to evolve according to eq. 5.1 and when I_s reaches I_c it goes rapidly through zero along a straight line connecting the points $(I_s, \phi) = (I_c, \phi_{max})$ to $(-I_c, -\phi_{max})$ for the next branch. This is shown in Fig 5.11 for $\alpha = .1 I_c$. This CPR is quite nearly a sawtooth function. The phase slip is modeled as a continuous, though abrupt process because the function does not quite reach π . This Khlebnikov quantum CPR is in fact single-valued. This CPR is also only valid in for wires with frequent quantum phase slips (QPS). Our wires don't show QPS in R vs. T measurements [14], however recent work has found evidence for their existence at high bias currents [15, 16], so this idea was tested.

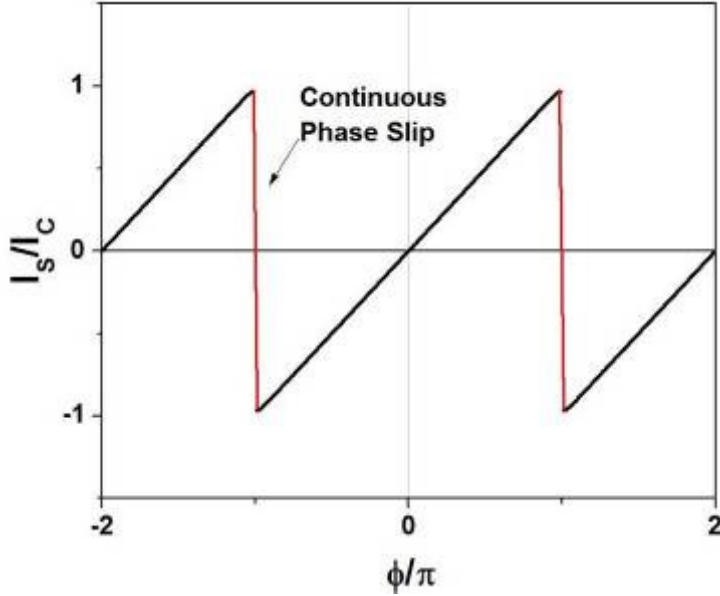


Figure 5.11 Schematic of the Khlebnikov CPR. The central black curve is a plot of equation 5.4 between its two extrema using $\alpha = 0.1 \cdot I_C$. The other black curves are this function shifted by 2π . The red lines are a linear connection to model the phase slip process.

In addition to the Likharev and Khlebnikov CPRs, two other test CPRs were used. These two model CPRs are given by the equations below:

$$I_S = I_C * \phi / \phi_{\max} \quad (5.5)$$

$$I_S = I_C * \sin(\pi / 2 * \phi / \phi_{\max}) \quad (5.6)$$

The first one is just the multi-valued analog to the sawtooth function for $\phi_{\max} > \pi$ and the second one was just a modification of the first to have some curvature. Equation 5.6 is very similar in shape to the Likharev CPR. Figure 5.12 shows how these functions are used in the model.

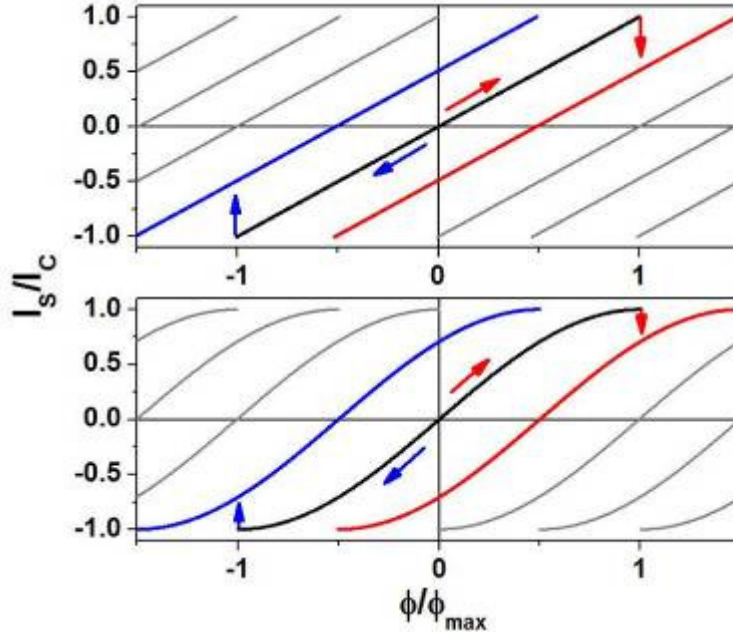


Figure 5.12 Other CPRs used in RSJ model for a nanowire. When the phase reaches it's maximum value the phase is changed abruptly by 2π . The arrows show this schematically as a transition to an adjacent branch of the CPR which is just the same function shifted by 2π on the phase axis. Top the CRP given by equation 5.5. Bottom the CPR given by equation 5.6.

5.2.2 Numerical Simulations

Numerical simulations were performed using MATLAB. The time evolution of the phase was computed by numerically integrating equation 5.1. The algorithm used goes as follows:

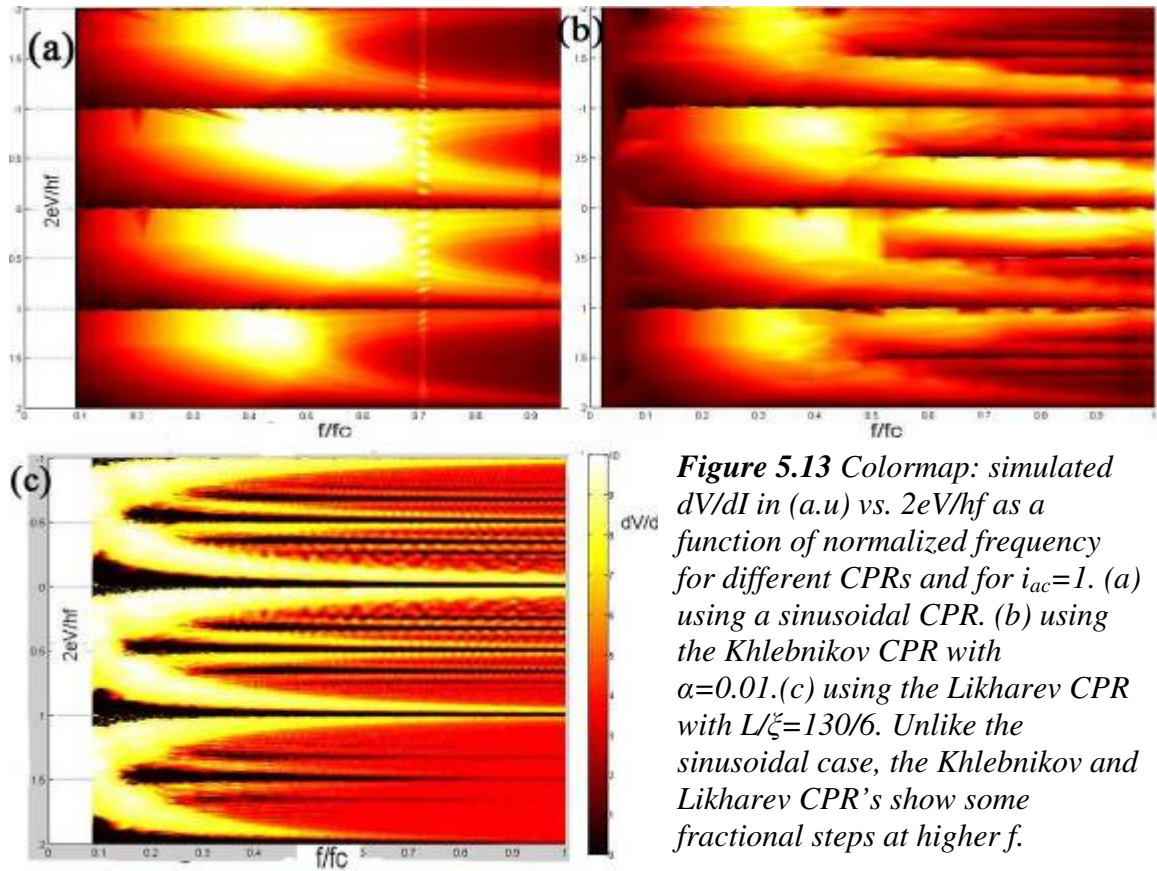
$$\dot{\phi}(t) = i_{dc} + i_{ac} \sin(\Omega t \Delta t) - I_S(\phi(t-1)) \quad (5.7)$$

$$\phi(t) = \phi(t-1) + \dot{\phi}(t-1)\Delta t + \sigma 2e / \hbar \sqrt{2k_B T R \Delta t} \quad (5.8)$$

Here t is the number of timesteps, Δt , and σ is a Gaussian random variable with mean zero and variance 1. The phase and its time derivative are computed for several periods of the MW signal and of the characteristic oscillation, $2\pi/f_c$ and then the average value of $\dot{\phi}$ is used to compute the voltage as $V=(h/2e)\langle d\phi/dt \rangle$. The result of this computation is an array of computed voltage values for each chosen value of DC bias current. This is used to also compute dV/dI values using a 3 point differentiation algorithm. To help decrease the noise in the computation and to try to mimic our method for collecting experimental data we use MATLAB's built in smoothing functions to perform adjacent averaging if desired.

5.2.3 Discussion

The CPRs outlined in the previous sections were all used with the algorithm described in section 5.2.2. Partial results are displayed in Fig 5.13. All multi-valued CPRs used in these simulations are implemented in a similar manner to that outlined in Fig 5.10 for the Likharev one (eq. 5.2). The phase is allowed to evolve by equations 5.7 and 5.8 until it reaches ϕ_{max} or ϕ_{min} and then the phase is changed by -2π or $+2\pi$ depending on which extremum it hits. The phase is then allowed to evolve by equations 5.7 and 5.8 again. Note that a pure sinusoidal CPR does not produce any fractional steps whereas the CPRs derived by Khlebnikov [10] and Likharev [11] and the ones described by equations 5.5 and 5.6 do.



The model shows higher order fractional steps as the frequency is increased for all CPRs that have some abrupt change. Figure 5.13 shows a 2D colormap of dV/dI plotted vs. normalized voltage ($2eV/hf$) and normalized frequency, Ω for 3 CPRs. The Khlebnikov model shows the fractional steps for normalized frequencies greater than 0.5. The Likharev one shows them for normalized frequencies near 0.15 for $L/\xi=130/6$. The normalized frequency, Ω is given by f/f_C with $f_C = 2eRI_C/h$. Taking 6 GHz to be the onset of the 1/3 step in sample 120207C and a critical current of 500 nA, the Likharev results predict a resistance of the resistive branch to be ~ 125 Ohms whereas the Khlebnikov one predicts R to be ~ 40 Ohms. The resistance at this frequency can be approximated from Fig. 4.3 and is approximately 120 Ohms. As stated early the Khlebnikov CPR is valid when QPS are frequent which might not be the case for this sample. It is interesting to note that by studying the microwave response of these wires one could, in principle determine whether or not QPS are present.

Figure 5.14 shows a comparison between actual data and a simulated set of data using the Likharev CPR with similar parameters. The overall shape of the simulated $V(I)$ curves as the power is increased is very similar to that observed in experiment and much different than those for the sinusoidal CPR[4]. Both experiment and simulation show some suppression of the low integer steps, however the simulation shows more oscillation in these steps than does the experiment. The reason for this is not understood and this behavior seems to be present in all of the model CPRs. One possible reason is that real samples are shunted with frequency-dependent impedance and they may be slightly underdamped at relevant frequencies.

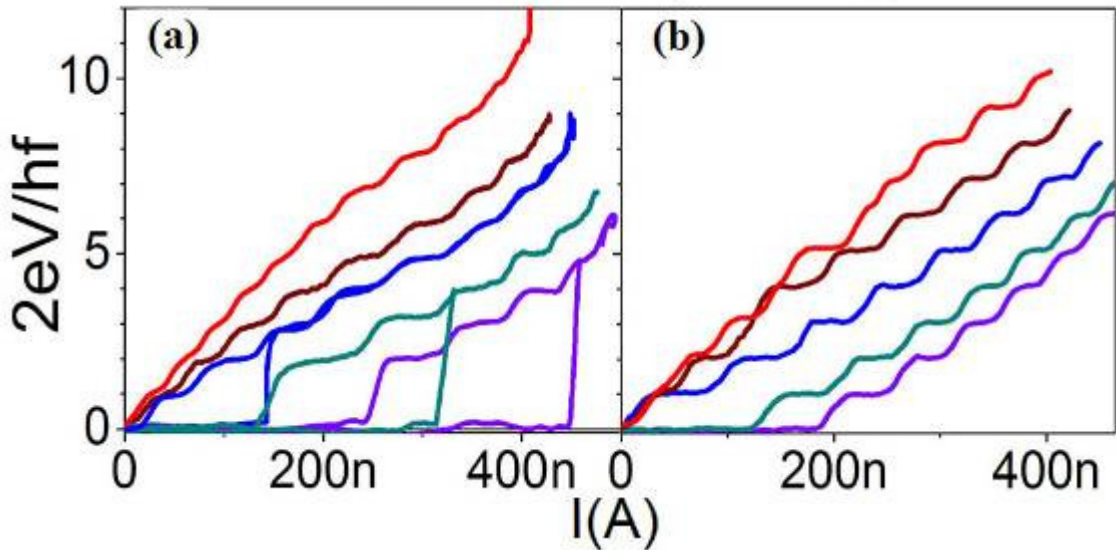
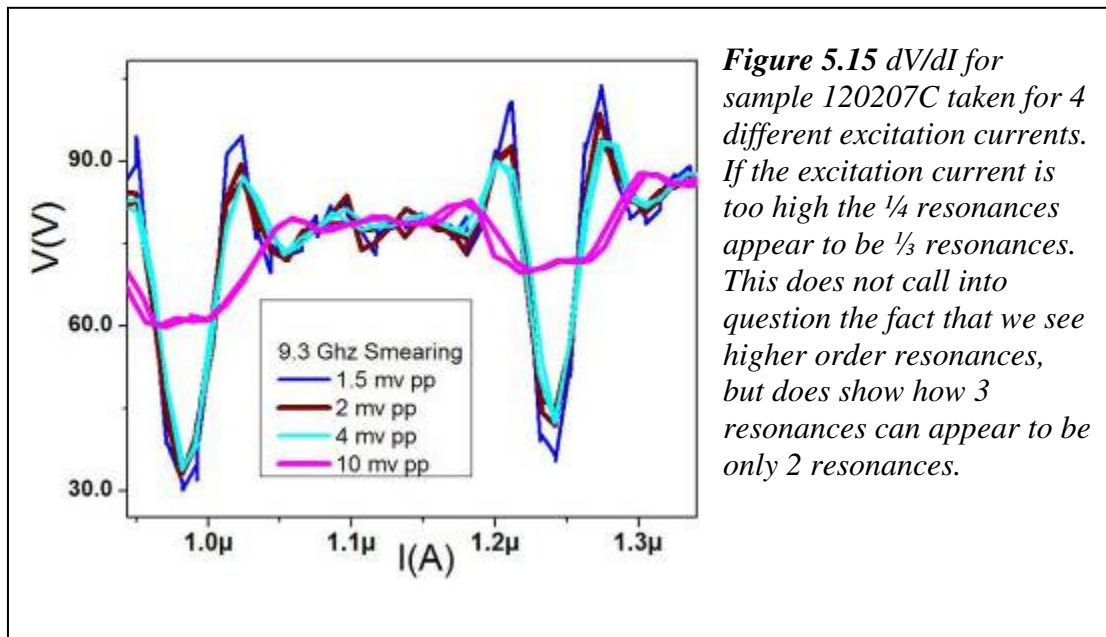


Figure 5.14 (a) Normalized voltage vs. bias current for sample A for MW powers in dBm decreasing from top to bottom curves as follows; -21.8, -22.4, -22.9, -24, -24.6. These curves end where the wire switches to JNS and low power MW show hysteresis and do not have the $n=1$ step. (b) Numerical simulations using the CPR given in the text for $L=140\text{nm}$, $\zeta=10\text{nm}$, $I_C=500\text{nA}$, $\Omega=0.1$ for i_{ac} decreasing from top curve to bottom curve as follows: 2.4, 2.0, 1.6, 0.8, 0.6. The simulated curves are extremely sensitive to the values of ζ and Ω .

5.3 A Brief Discussion of Noise

Fractional Shapiro steps are very difficult to observe in our system due to the inherent voltage noise $\sim 2 \mu\text{V}$ which makes it very unlikely that we could observe them in $V(I)$ curves. We need to apply an AC current to measure dV/dI so our ability to resolve them are limited to the size of the signal we need to apply in order to measure any appreciable signal. Figure A5.1 shows how the excitation current can smear 3 resonances into what appears to be 2. I.e. it takes $\frac{1}{4}$ resonances and makes them appear as though they are $\frac{1}{3}$ resonances. This could explain why we don't see the $\frac{1}{2}$ resonances at all frequencies as predicted by our model. Due to the abrupt appearance of the steps, and the qualitative reproduction of this behavior with our model, it is unlikely that all these resonances are always there, but simply obscured by noise and smearing. Figure 5.16 shows more data than Fig 5.7 to illustrate how quickly the new resonances appear.



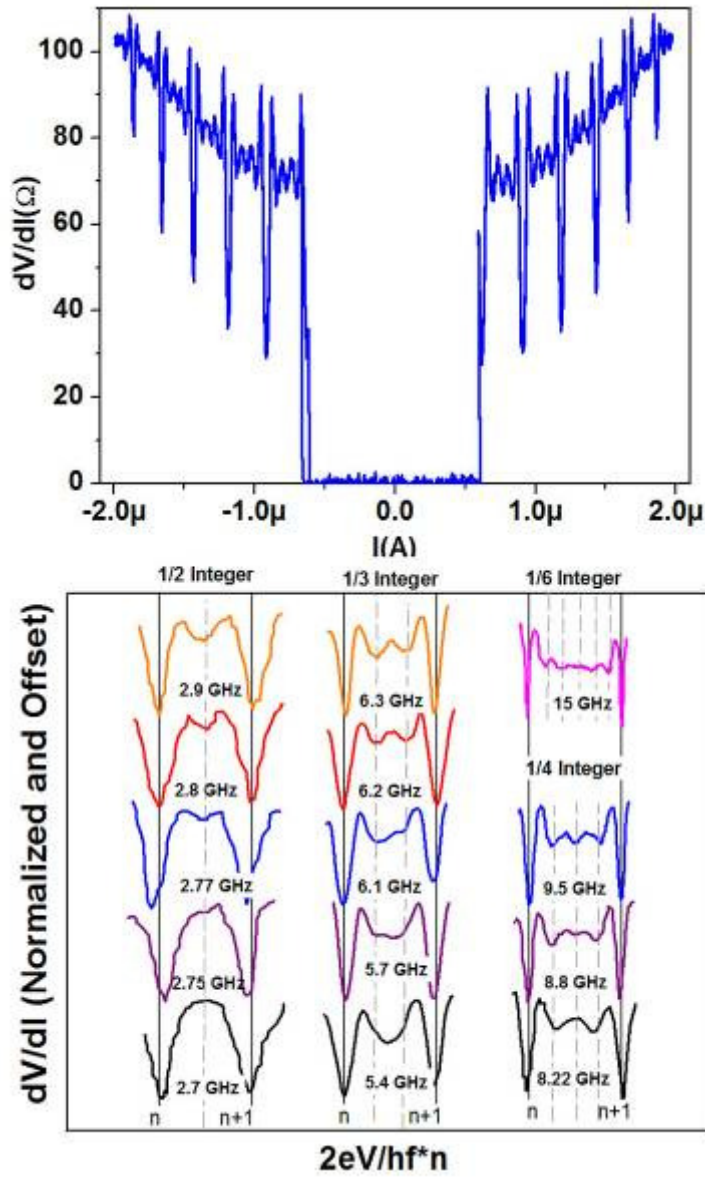


Figure 5.16 Same data as Fig 5.7 only expanded and plotted vertically.

5.4 References

- [1] R.C.Dinsmore III, Myung-Ho Bae, A. Bezryadin. *Appl. Phys. Lett.* **93**, 192505 (2008).
- [2] Myung-Ho Bae, R.C.Dinsmore III, A. Bezryadin. Submitted (2009) .
- [3] P. W. Anderson and A.H. Dayem, *Phys. Rev. Lett.* **13**, 195 (1964).
- [4] P. Russer, *J. Appl. Phys.* **43**, 2008 (1972).
- [5] D. E. McCumber, *J. Appl. Phys.* 39, 3113 (1968); W. C. Stewart, *Appl. Phys. Lett.* 12 277 (1968).
- [6] N. Gronbech-Jensen, et al, *Phys. Rev. Lett.* **93**. 107002 (2004).
- [7] H. Sellier, C. Baraduc, F. Lefloch & R. Calemczuk, *Phys. Rev. Lett.* **92**, 257005 (2004).
- [8] K. K. Likharev and L. A. Yakobson, *Zh. Tekhn. Fiz* **45**, 1503-1507 (1975); *Sov. Phys. Tech. Phys.* **20**, 950-954 (1975).
- [9] D. Pekker, A. Bezryadin, D. S. Hopkins, and P. M. Goldbart, *Phys. Rev. B* **72**, 104517 (2005).
- [10] S. Khlebnikov, *Phys. Rev. B.* **78**, 014512 (2008).
- [11] K. K. Likharev, *Rev. Mod. Phys.* **51**, 101-159 (1979).
- [12] A. Golubov, A. Kupriyanov, M. Yu. & Il'ichev, *Rev. Mod. Physics.* **76**, 411-469 (2004).
- [13] Private correspondence with S. Klebnikov (2008).
- [14] A. Bezryadin, *J. of Phys. Condens. Matter* **76**, 043202 (1-11) (2008) and references therein.
- [15] M. Sahu, et al. arXiv:0804.2251v2 (2008).
- [16] N. Shah, D. Pekker, and P. M. Goldbart, *Phys. Rev. Lett.* **101**, 207001 (2008).

Author's Biography

Robert Chesley Dinsmore III was born on May 3rd 1976 in Lowell, Massachusetts. He graduated from the University of Massachusetts in May of 1999 with a B.S. majoring in both Chemistry and Physics. Robert graduated with *magna cum laud* honors and was awarded the Outstanding Chemistry Student Award in 1998. Robert's research interests as an undergraduate were in the field of theoretical chemistry. In the fall of 2001 Robert enrolled as a Physics Graduate student at Northeastern University in Boston Massachusetts. While at Northeastern, Robert was awarded a GANN fellowship to study advanced scientific computation. Robert received an M.S. in Physics in June 2003.

In the fall of 2003 Robert enrolled at the University of Illinois at Urbana Champaign to begin his doctoral studies. He joined the group of his advisor, Alexey Bezryadin in January of 2005. As a member of the Bezryadin group, Robert learned to fabricate nanowires using carbon nanotubes as templates. Robert used these wires to study the effects of microwave radiation on quasi-one-dimensional wires and published some of this work in *Appl. Phys. Lett.* Most recently, Robert studied the enhancement of quantum phase slips in the presence of microwave radiation. Following the completion of his Ph.D., Robert will begin his work for Intel Corporation as a Process Development Engineer.